eXPRESS Polymer Letters Vol.10, No.10 (2016) 788
Available online at www.expresspolymlett.com
DOI: 10.3144/expresspolymlett.2016.73

Editorial corner – a personal view
3D-printed polymers for biomedical applications

J. Seppälä[*]

Aalto University, Department of Biotechnology and Chemical Technology, Kemistintie 1 Espoo, P.O. Box 16100, FI-00076 Aalto, Finland

Great opportunities in science appear when significant technology leaps take place simultaneously in several complementary areas. This is the case in polymeric biomaterials' technology.

Amazing advances have been made in the additive manufacturing technologies, i.e. 3D-printing. It is a family of different layer by layer manufacturing methods like fused deposition modeling, powder laser sintering, ink-jet printing, stereo lithography, two or multi photon polymerization and hydrogel 3D-printing. All of them applicable for processing of polymeric materials. Essential developments have taken place also in biomedical imaging and 3D-design to create the necessary digital models needed for the 3D-printing. At the same time great progress has been achieved in biopolymers' development. They can be tailored to be biostable or bioresorbable in a controlled way, or in some cases even bioactive. Bioactivity has been achieved through addition of bioactive compounds like bioactive glass or through functionalization of the polymeric structure (www.kunststoffe-international.com/1332070, DOI: 10.1016/j.actbio.2011.06.039, DOI: 10.1016/j.compscitech.2012.10.014, DOI: 10.1002/jbm.b.32863, DOI: 10.1002/pola.27400, DOI: 10.1039/C5TB01468A).

The parallel advance which has taken place in the biomedical sciences has significantly improved the options in regenerative medicine and may even enable tissue engineering. For polymer research this important and fast developing area offers great opportunities of high societal impact. However, the demands for polymer properties are strict for the novel biomaterials. They should meet the various physical criteria set by the needs of the application, but in addition the demand of non-toxicity is a self-evident must in biomedical applications. Successful 3D-additive manufacturing sets requirements to master the viscosities and liquid to solid transitions in the printing process. In stereo lithography the oligomeric low viscosity prepolymers need to be fast photo curing; with photo curing chemistry that is non-toxic in the biological environment and can get approved by the authorities. Especially for resorbable polymers there is a need to find alternative curing chemistries in addition to acrylate or methacrylate based systems. (www.kunststoffe-international.com/1325854) Complementary research interplay is essential in this field of science. An excellent example of such an effort has been the ArtiVasc 3D-project funded by the 7th Framework Program of the European Union to prepare polymeric scaffolds for vascularized, cell tissue cultivated skin like tissue. Outcome of the project is presented in the video: ArtiVasc 3D on the Way to Bio-Artificial Tissue. Novel technologies, breakthroughs in biomedical sciences together with innovative novel polymers enable jointly significant enhancements for life!

Prof. Dr. Jukka Seppälä
Member of the International Advisory Board

[*]Corresponding author, e-mail: jukka.seppala@aalto.fi

eXPRESS Polymer Letters Vol.10, No.10 (2016) 789–798
Available online at www.expresspolymlett.com
DOI: 10.3144/expresspolymlett.2016.74

Synthesis and characterization of flexible and high-temperature resistant polyimide aerogel with ultra-low dielectric constant

X. M. Zhang[1*], *J. G. Liu*[2], *S. Y. Yang*[2]

[1]School of Electrical Engineering, Beijing Jiaotong University, 100044 Beijing, China
[2]Laboratory of Advanced Polymer Materials, Institute of Chemistry, Chinese Academy of Sciences, 100190 Beijing, China

Received 10 March 2016; accepted in revised form 2 May 2016

Abstract. A polyimide (PI) aerogel with excellent combined thermal and dielectric properties was successfully prepared by the polycondensation of 3,3′,4,4′-biphenyltetracarboxylic dianhydride (BPDA), 5-amino-2-(4-aminophenyl)benzoxazole (APBO) and octa(amino-phenyl)silsesquioxane (OAPS) crosslinker, followed by a supercritical carbon dioxide ($scCO_2$) drying treatment. The developed PI aerogel exhibited an ultra-low dielectric constant (k) of 1.15 at a frequency of 2.75 GHz, a volume resistivity of $5.45 \cdot 10^{14}$ Ω·cm, and a dielectric strength of 132 kV/cm. The flexible PI aerogel exhibited an open-pore microstructure consisting of three-dimensional network with tangled nanofibers morphology with a porosity of 85.6% (volume ratio), an average pore diameter of 19.2 nm, and a Brunauer-Emmet-Teller (BET) surface area of 428.6 m^2/g. In addition, the PI aerogel showed excellent thermal stability with a glass transition temperature (T_g) of 358.3 °C, a 5% weight loss temperature over 500 °C, and a residual weight ratio of 66.7% at 750 °C in nitrogen.

Keywords: *thermal properties, polyimide aerogel, supercritical drying, dielectric properties*

1. Introduction

In the past decades, polymer dielectrics with low dielectric constant (low-k) and low dissipation factor features have been paid increasing attention in ultra-large scale integrated circuit (ULSI) fabrication due to their abilities to lower the line-to-line noise in interconnects and alleviate power dissipation issues by reducing the capacitance between the interconnect conductor lines so as to achieve faster signal transmission speed [1–3]. Among various polymer dielectrics, polyimides (PIs) have been investigated more extensively as high performance interlayer dielectrics (ILDs) than most other polymers due to their desirable high-temperature stability, excellent mechanical and dielectric properties for ULSI fabrications [4–6]. However, conventional PI dielectrics usually have k values around 3.0, which cannot meet the rapid development of ULSI assembly. For example, according to the prediction of International Technology Roadmap for Semiconductors (ITRS), by 2016, a k value below 2.0 at 1 GHz and a dielectric loss below 0.003 have to be met for the ILDs [7]. It has been proven that the common methodologies reducing the k values for conventional PIs ($k \approx 3.0$), including introduction of substituents with low molar polarizability (fluorinated groups, alicyclic groups, etc.) or with large molar volumes (phenyl, fluorene, etc.) could only achieve a lowest k value around 2.5 [8].

In recent years, it was found that incorporation of air voids ($k = 1.0$) into the polymers is efficient to achieving a k value less than 2.0. Thus, various macroporous,

*Corresponding author, e-mail: xmzhang@bjtu.edu.cn

mesoporous or nanoporous low-*k* polymer films have recently been very attractive for ILD applications to reduce *k* to a minimum value [9]. By this methodology, various ultra low-*k* PIs have been reported [10–14]. However, the attempts further reducing the *k* values of PIs below 1.5 seem to be more challenging because the conventional methods could only achieve a very limited air loading (<60%, volume ratio).

Very recently, aerogel dielectrics have been becoming one of the most important research topics for high performance ILDs using in ULSI due to their extremely high porosity, low density, low thermal conductivity, and ultra-low dielectric constants [15]. The porosity of an aerogel material can usually reach over 80% (volume ratio). The trapped air efficiently decreases the *k* values of the aerogels to a low level extremely close to 1.0 for air. Among various aerogels, organic polymeric aerogels are more suitable to be used as ILDs for ULSI due to their intrinsically flexible and tough nature compared with their fragile inorganic counterparts, such as silica, alumina aerogels, etc. [16]. Various polymer aerogels, such as polyurethane, polyurea, polystyrene, and polydicyclopentadiene aerogels have been widely investigated in the literature and have been finding a variety of applications in high-tech fields [17]. However, common organic aerogels usually suffer from their low thermal and dimensional stability at elevated temperatures; thus cannot meet the severe demands of interlayer electrical insulation process for ULSI fabrications. Thus, as a representative high-temperature resistant organic aerogels, PI aerogels have been developed rapidly in recent years [18–22]. The dielectric constants and dissipation factors for PI aerogels have also been investigated in detail. For instance, Meador and coworkers studied the dielectric properties of PI aerogels and investigated their potential applications as substrates for lightweight patch antennas for aerospace applications [23, 24]. Relative *k* values as low as 1.16 at a frequency of X-band (~11–12 GHz) were obtained for PI aerogels made from 3,3′,4,4′-biphenyl tetracarboxylic dianhydride (BPDA), 2,2′-dimethylbenzidine (DMBZ), and 1,3,5-tris(4-aminophenoxy)benzene (TAB) crosslinker. Shen and coworkers have reported intrinsically highly-hydrophobic semi-alicyclic fluorinated PI aerogel with ultra-low k values of 1.17–1.19 in the frequency range of 2–12 GHz [25].

The dielectric constants and dissipation factor of PI aerogels have been investigated in the literature; however, other dielectric behaviors for PI aerogels have been rarely addressed in the literature although they are also very important for their applications in ULSI. For example, in addition to low dielectric constants, the next generation of ILDs for submicron and nano-level electronics must also satisfy a variety of other requirements, including high dielectric strength and resistivity, high thermal and dimensional stability, low moisture adsorption, and good adhesion to semiconductor and metal substrates in order to achieve high reliability [26]. As we know, for porous low-*k* polymers, while increasing porosity can reduce the *k* values; however, the dielectric strength is often adversely affected. To the best of our knowledge, the dielectric breakdown behavior for PI aerogels or even organic aerogels has been rarely involved in the literature. In the current paper, a PI aerogel was first prepared from BPDA, APBO and OAPS via a $scCO_2$ drying procedure, and then the thermal and dielectric properties for the aerogel were investigated in detail. Especially the dielectric breakdown behavior for the aerogel was studied.

2. Experimental

2.1. Materials

3,3′,4,4′-Biphenyltetracarboxylic dianhydride (BPDA) and 5-amino-2-(4-aminophenyl)-benzoxazole (APBO) were purchased from Tokyo Chemical Industry Co., Ltd. (TCI), Japan. BPDA was dried *in vacuo* at 180 °C overnight prior to use and APBO was used as received. Octa(aminophenyl) silsesquioxane (OAPS) was purchased from Meilian Composite Co. Ltd., Liaoning, China and used as received. *N*-methyl-2-pyrrolidinone (NMP) was purified by vacuum distillation over CaH_2 and stored over 0.4 nm molecular sieves prior to use. The other commercially available reagents were used without further purification.

2.2. Characterization

Fourier transform infrared (FT-IR) spectrum was obtained on a Bruker Tensor-27 FT-IR spectrometer. Field emission scanning electron microscopy (FE-SEM) was obtained on a Hitachi S-4800 microscope. PI aerogel surface area (σ) and pore size distribution were measured by nitrogen adsorption and desorption at 77 K using a Micromeritics ASAP 2000 surface

areas and porosity analyzer. Before testing, the PI aerogel sample was outgassed at 80 °C for 10 h *in vacuo*. The surface area was calculated by Brunauer-Emmet-Teller (BET) method and pore size distribution was calculated by Barret-Joyner-Halenda (BJH) method. The bulk density (ρ_b) and skeletal density (ρ_s) were measured by mercury intrusion porosimetry using a Micromeritics Auto Pore IV9520 porosimeter. The percent porosity was calculated as: porosity (%) = $(1–\rho_b/\rho_s)\cdot 100$. The thermogravimetric analyses (TGA) were recorded on a TA-Q50 thermal analysis system at a heating rate of 20 °C/min in nitrogen. Thermal mechanical analyses (TMA) were performed on a TA-Q400 analyzer over 50–400 °C at a heating rate of 5 °C/min in nitrogen. The compression properties of the PI aerogels were measured on an Instron 5567 according to the ASTM Standard D 695-10. The Young's modulus was determined as the initial linear portion of the slope of the stress-strain curve. The electrical insulation properties were measured on a PC68 digital high-voltage and high-resistance Megger instrument. The surface resistivity (ρ_s) and volume resistivity (ρ_v) of PI aerogel were measured according to ASTM D-257-91. The samples were dried at 120 °C for 1 h prior to measurement. Dielectric strength of PI aerogel film (d = 2.5 mm) were measured according to ASTM D-149-81, which were subjected to 60 cycles AC voltage at 100 V/s rate of rise to the breakdown voltage. The broadband dielectric constant (k) and dissipation factor (δ) is measured by an Agilent vector network analyzer (Model 8510) at room temperature. The frequency was in the range of 2–12 GHz and the sample size was 50 mm ×30 mm×2.5 mm.

2.3. Synthesis of PI aerogel

To a three-necked 250 mL flask equipped with a mechanical stirrer, a nitrogen inlet and a cold water bath was charged with APBO (1.3885 g, 6.1644 mmol) and NMP (25 g) at 10–15 °C under a nitrogen flow of 10 mL/min. After stirring for 20 min, a clear solution was obtained. Then, BPDA (1.8722 g, 6.3632 mmol) was added in one batch and an additional volume of NMP (26 g) was added to wash the residual dianhydride and adjust the solid content of the reaction solution to be 6 wt%. The cold water bath was removed after 2 h. The mixture was stirred at room temperature for 12 h to yield a viscous poly(amic acid) (PAA) solution. To the solution, OAPS (0.0575 g, 0.0497 mmol) was added and the reaction mixture was stirred at room temperature for another 12 h to afford a pale-brown viscous solution. Acetic anhydride (3.1 mL, 31.6 mmol) and pyridine (2.6 mL, 31.6 mmol) were then added to the PAA solution. After stirring at room temperature for 30 min, the solution was poured into pre-prepared molds. The molds were pre-made into various required shapes according to the demands of different measurement standards. For example, disk-shape molds were made for dielectric properties measurements; cylinder-shape for compression measurements; and rectangular shape for TMA measurements, etc.

The PAA solution gelled within 2 h and further aged for 24 h in the molds. Then, the gels were continuously immersed into a solution of 75% NMP in ethanol for 24 h, then a 25% NMP in ethanol for 24 h, and finally a 100% ethanol for 24 h. The obtained wet gels were then dried in a 160 L supercritical CO_2 ($scCO_2$) autoclave (maximum temperature: 80 °C; maximum pressure: 32 MPa; and maximum flow: 400 L/h) at the condition of 45 °C under 15 MPa for three cycles, 2 h each time. Then, the PI aerogel (BPDA/APBO/OAPS) was dried in vacuo at 80 °C for 24 h to afford the target aerogels as yellow monolithic solids with various shapes.

3. Results and discussion

3.1. PI aerogel preparation

A PI aerogel was designed and synthesized from rigid BPDA dianhydride, benzoxazole-containing APBO diamine, and POSS-containing OAPS crosslinking agent, as shown in Figure 1. Basically rigid molecular skeleton structures would guarantee the high thermal and dimensional stability for the PI aerogel. Introduction of benzoxazole moiety into the molecular structure of the PI aerogel via diamine monomer is to endow the polymer with good dielectric properties. As we know, polybenzoxazole (PBO) has an advantage over other polar high-temperature polymers (PI, polyamide, polybenzimidazole, etc.) due to the absence of polar groups in its repeating unit. The absence of polar groups in the polymer prevents the formation of hydrogen bond between the polymer and water, therefore resulting in less water absorption in the polymer and low dielectric constant (<2.9 at 1 MHz) and dielectric loss factor [27]. Ad-

ditionally, PBO is also known for its excellent thermal and thermo-oxidative resistance, high electrical resistivity, and high dielectric strength over a long temperature period. Thus, the benzoxazole moiety in the current PI aerogel might provide various desirable properties for the target aerogel. At last, OAPS was chosen to be an end-capper to crosslink the PI system affording the three-dimensional network microstructure. The nanoporous cage structure for OAPS is undoubtedly beneficial to decreasing the *k* values

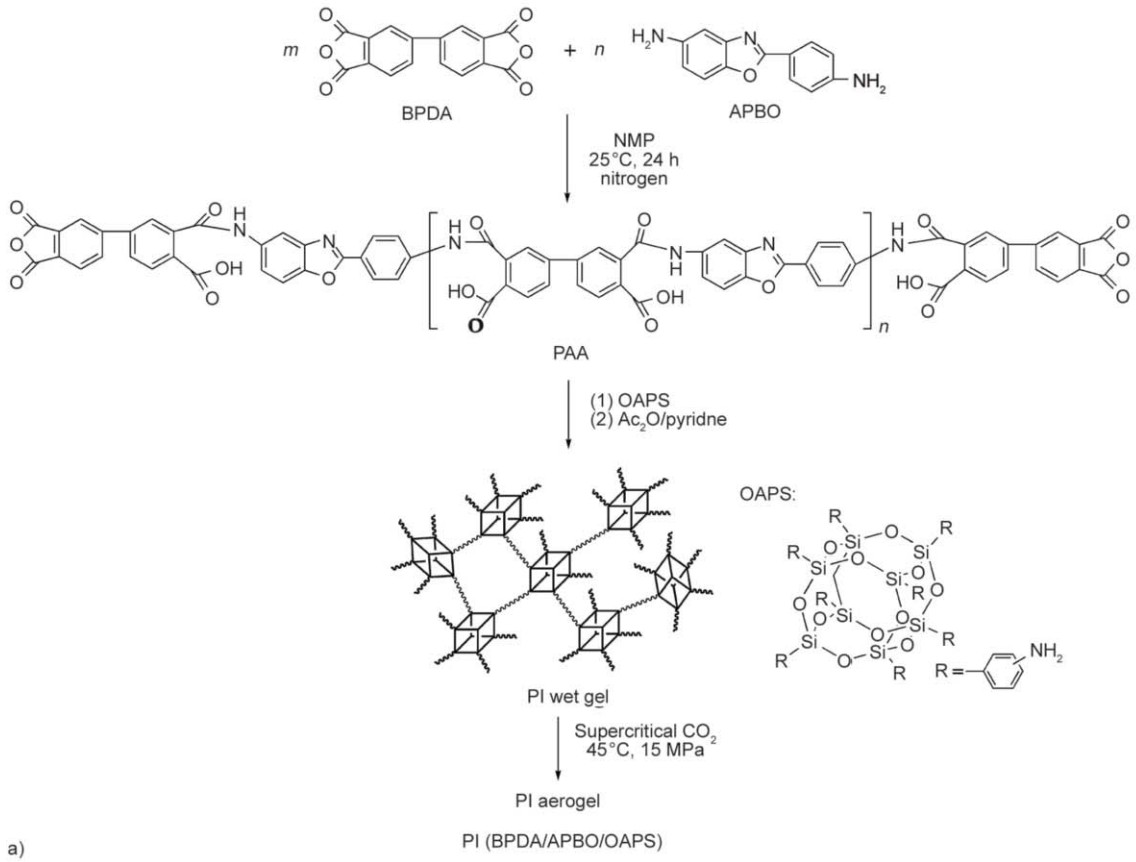

a)

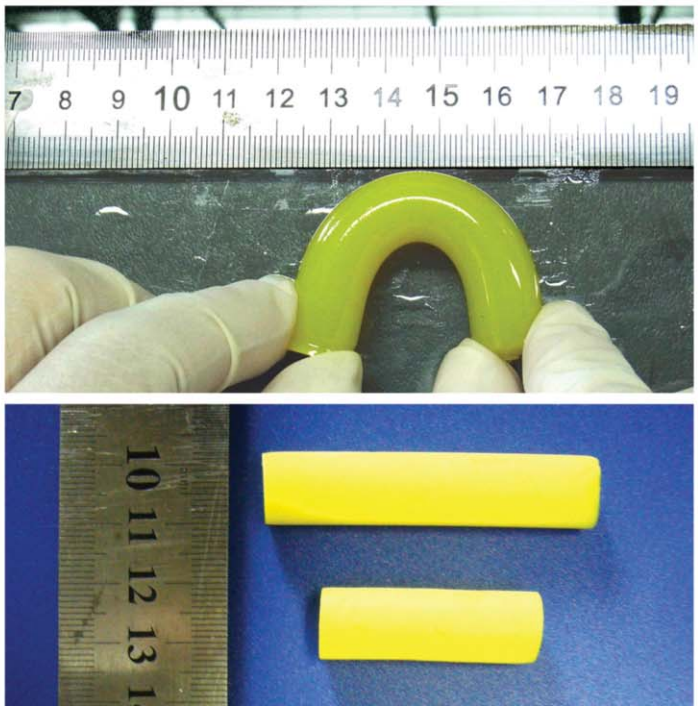

b)

Figure 1. (a) Synthesis of PI (BPDA/APBO/OAPS) aerogel, (b) appearance of PI wet gel (above) and PI aerogel (below)

for the PI aerogel. Actually, OAPS has been widely used as components to develop low-*k* PI films. PI composite films with k values around 1.9 have been prepared by OAPS functionalized graphene oxide and PI matrix [28].

In the preparation, excessive BPDA was first reacted with APBO to give a anhydride-capped PI precursor, poly(amic acid) (PAA) solution. Then, OAPS was added into the PAA solution inducing a crosslinking reaction of the PAA. Dehydrating agent (acetic anhydride/pyridine system) was then added into the solution affording a PI wet gel. The PI wet gel exhibited excellent flexibility and toughness, which could be bent with a large radius of curvature (picture inserted in Figure 1). Then, the PI wet gel was immersed into ethanol to extract the NMP solvent. At last, the residual NMP and ethanol trapped in the gel was dried with $scCO_2$ at 45 °C with a pressure of 15 MPa to give the final PI aerogel (Figure 1). This drying condition is more efficient and gentle than that of other supercritical fluids, such as supercritical ethanol (critical point: 243 °C, 6.38 MPa). The prepared PI aerogel exhibited good mechanical properties. The stress-strain correlation in the compression tests indicated linear elastic regions below 10% strain and yielded in a relatively low slope for the aerogel. The compression stress of the PI aerogel at 10% strain is 0.92 MPa and the Young's modulus is 18.2 MPa. These values are comparable to those mechanically strong PI aerogels reported in ref, [21]. The good mechanical properties for the PI aerogel are mainly attributed to the flexible and tough nature for the PI resin containing rigid biphenyl and benzoxazole moieties. In our experiments, PI aerogels with various shapes and sizes, including rods, films, sheets, and bulks were prepared for further measurements.

The chemical structures of the PI aerogel were identified by FT-IR measurements, illustrated in Figure 2. The characteristic absorption bands due to the vibration of the carbonyl groups (C=O) in the imide segments are clearly observed at 1766 and 1722 cm^{-1}, which are assigned to the asymmetric and symmetric stretching vibrations, respectively. In addition, the stretching vibration of C–N bond located at 1371 cm^{-1} and the imide ring deformation at 740 cm^{-1} further confirm the formation of PI. Meanwhile, the absence of absorbing band around 1855 cm^{-1} ($\upsilon_{C=O}$ in BPDA) indicated the complete reaction of the dianhydride.

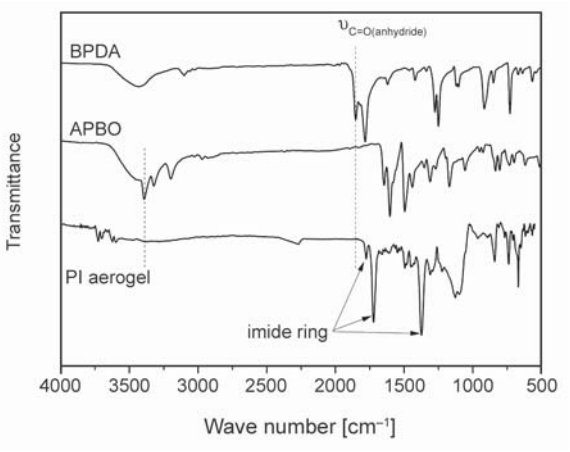

Figure 2. FT-IR spectra of PI aerogel and its crude materials

Similarly, absorbing bands around 3392 cm^{-1} (υ_{N-H} in APBO) and 1640 cm^{-1} ($\upsilon_{amide,\ C=O}$ in PAA) are also absent, indicating the completion reaction of the APBO and the successful conversion from the PAA precursors to PIs by chemical imidization.

3.2. PI aerogel morphology

The microtopography and physical parameters of the PI aerogel, including density, porosity, surface area, and volume shrinkage were investigated in detail. First, the FE-SEM measurement was performed to investigate the morphology of the PI aerogel, as shown in Figure 3. For the polymer, the open-pore structure consisting of three-dimensional networks with tangled nanofibers morphology having diameters at the nanometer scale were observed. This morphology determined the properties of the PI aerogel. The open-pore structure might endow the aerogel with low density and low dielectric constants, while the three-dimensional networks tangled with nanofibers might provide good mechanical properties for the aerogel. The morphology-property correlations will be subsequently discussed in detail.

This three-dimensional network microstructures for the PI aerogel are mainly caused by the highly crosslinked structure of the molecular chains in the aerogel. The solvents in the networks were continuously extracted by the solvent exchange process and following supercritical drying procedures, leaving nano pores in the final aerogels. The volume of the PI aerogel shrinks 14.5% of its original value during the supercritical drying process. This value is comparable to the PI aerogels reported in the literature [29]. The low shrinkage and microtopography for the current

aerogel prove that supercritical drying is an efficient procedure producing polymer aerogels. It has been established that supercritical fluids obtained above the critical point in temperature-pressure diagram enable drying the wet polymer gels without capillary stress due to absence of liquid-vapor interfaces in the phase [30]. In addition, $scCO_2$ is a clean and versatile solvent, which has been widely used for the processing of a range of porous polymers due to the chemical, environmental, and economic advantages [31]. Using this technique, porosity higher than 85–90% and dielectric constants below 1.5 can usually be obtained. Adversely, for other porous gels, such as Xerogels prepared by common drying techniques, the gels are easily collapsed by capillary stress induced at the liquid-vapor interfaces during drying process, resulting in apparent shrinkage for the nanoporous gels (>30%). The porosity is usually lower than 60–80% and the k values are always higher than 1.50 [32, 33].

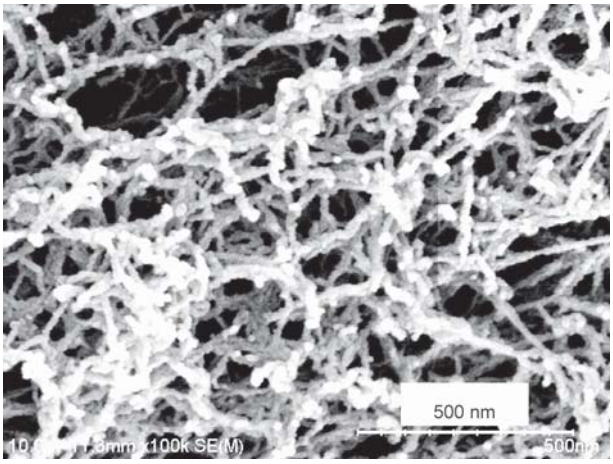

Figure 3. SEM image of PI aerogel

The structural parameters for PI aerogel are tabulated in Table 1. The ρ_b and ρ_s values of PI aerogel were measured by mercury intrusion porosimetry method. The nanoporous structure for the aerogel endows them with low bulk density (ρ_b) of 0.21 g/cm^3. Air occupies the free empty space in the aerogel with a porosity of 85.6% as calculated from the ρ_b and skeletal density (ρ_s) of the aerogel. The surface areas (σ) and pore size distribution of the PI aerogel were measured by N_2 adsorption and desorption isotherms, using the Brunauer-Emmet-Teller (BET) method. As deduced from the N_2 adsorption-desorption isotherm shown in Figure 4, the PI aerogel shows BET surface area of 428.6 m^2/g. The pore size distribution of PI aerogel calculated by Barret-Joyner-Halenda (BJH) method (Figure 4b) indicates that the average pore diameter in PI aerogel is 19.2 nm. In addition, it can be seen from Figure 4 that PI aerogel showed rapid increases in adsorbed volumes at relative pressure above 0.9 and the desorption plots exhibited narrow loops. All this information indicates that both mesoporous and macroporous structures exist in the PI aerogel.

Table 1. Structural parameters and thermal properties of the PI aerogel

Sample	ρ_b[a] [g/cm^3]	ρ_s[b] [g/cm^3]	Porosity[c] [%]	σ[d] [m^2/g]	d[e] [nm]	$T_{5\%}$[f] [°C]	R_{w750}[g] [%]	T_g[h] [°C]
PI aerogel	0.21	1.46	85.6	428.6	19.2	502	66.7	358.3

[a]Bulk density. [b]Skeletal density. [c]Calculated by $1–(\rho_b/\rho_s)$. [d]Brunauer-Emmett-Teller (BET) surface area. [e]Average pore diameter from the BJH desorption plot. [f]Temperature at 5% weight loss. [g]Residual weight ratio at 750 °C in nitrogen. [h]Glass transition temperature.

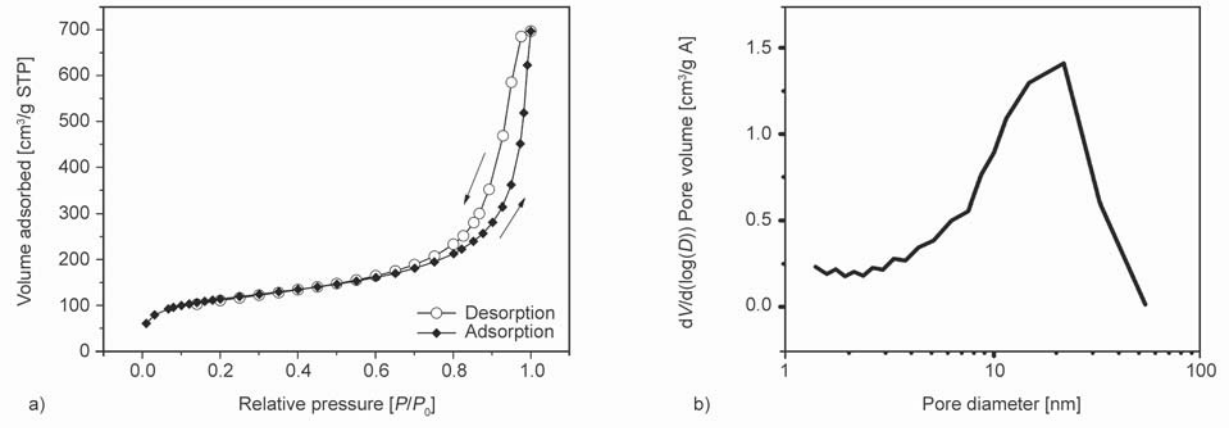

Figure 4. (a) N_2 adsorption-desorption isotherm data for PI aerogel. (b) pore size distribution plot (BJH plot)

3.3. Thermal properties

Thermal properties of the PI aerogel were evaluated by thermogravimetric analyses (TGA) and thermal mechanical analyses (TMA) measurements and the data were tabulated in Table 1. The TGA measurements of the PI aerogels were performed in nitrogen from 50 to 750 °C and the results are shown in Figure 5. From the plot, it can be observed that the aerogel showed good thermal stability up to 450 °C. The smooth plots around 300 °C indicated the complete remove of residual NMP solvent by the supercritical drying procedure and the complete imidization in the system. The 5% weight loss temperatures ($T_{5\%}$) are 505 °C and the residual weight ratio (char yield) of the aerogel at 750 °C is 66.7% in nitrogen, indicating good thermal stability of the aerogel.

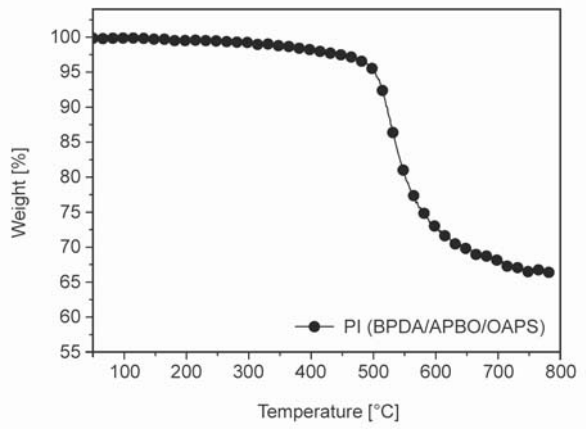

Figure 5. TGA plot of PI aerogel

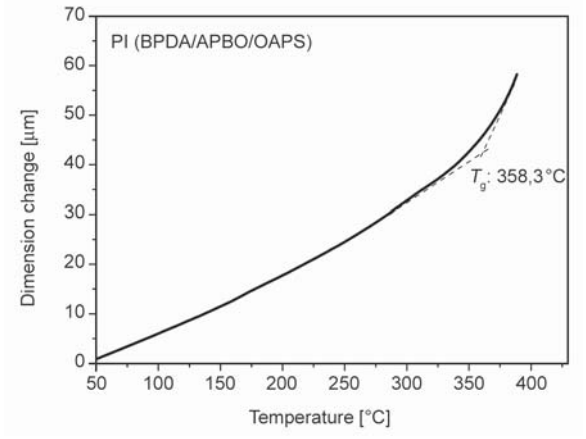

Figure 6. TMA plot of PI aerogel

The dimensional changes of aerogel at elevated temperatures were investigated by TMA measurements, as depicted in Figure 6. The aerogel showed expansion behavior after the occurrence of glass transition around 350 °C. A T_g value was recorded at 358.3 °C for the aerogel. This value is much higher than those of common polymer aerogels, which can guarantee the good reliability of the aerogel in ULSI fabrication.

3.4. Dielectric properties

The dielectric properties of the PI aerogel, including surface (ρ_s) and volume (ρ_v) resistivity, dielectric strength, dielectric constant and dissipation factor were investigated. These dielectric parameters are critical for their applications in ULSI applications. As shown in Table 2, the ρ_v and ρ_s values for the aerogel are $5.45 \cdot 10^{14}$ Ω·cm and $8.74 \cdot 10^{13}$ Ω, respectively, indicating excellent electrical insulation properties.

The dielectric breakdown strength of the aerogel is 132 kV/cm at a thickness of 2.5 mm in our measurement. This value is a bit higher than that expected for porous materials. Similar phenomenon has also been observed by Hrubesh and Pekala [34] in their research on inorganic silica aerogels. In their investigation, the dielectric strength of 128 kV/cm was recorded for silica aerogels and this value was higher than those of common ceramics, such as alumina (110 kV/cm) although lower than those of pure polymers (160–500 kV/cm). The authors ascribed this unexpected high dielectric strength for aerogels to the small pore sizes in the air-filled aerogels. The pore sizes are of the same order as the mean free path for electron collisions. Thus, electrons in aerogel pores tend to collide with the solid before gaining sufficient kinetic energy to ionize upon impact. In the current work, the dielectric strength of 132 kV/cm at a thickness of 2.5 mm was recorded, which is comparable to that of inorganic silica aerogels.

We further investigated the dielectric breakdown behavior for the PI aerogel. Figure 7 compares the surface macro- and micro-topographies of PI aerogel before and after dielectric breakdown under high

Table 2. Dielectric properties of the PI aerogel

	ρ_v[a] [Ω·cm]	ρ_s[a] [Ω]	d[b] [mm]	D_S[c] [kV/cm]	k[d]	δ[e]
PI aerogel	$5.45 \cdot 10^{14}$	$8.74 \cdot 10^{13}$	2.5	132	1.15	0.0023

[a]ρ_V and ρ_s: volume and surface resistivity at 23 °C and 50% relative humidity, respectively; [b]PI aerogel thickness for k measurements; [c]dielectric breakdown strength; [d]dielectric constant at 2.75 GHz; [e]dielectric loss factor at 2.75 GHz.

voltage. From the illustration, we can obviously observe that high level electrical voltage induces not only the dielectric breakdown, but apparent surface ablation phenomena in the tested area. Many pinholes were observed at the tested area, indicating dielectric breakdown of the PI solid. Basically, the dielectric properties of aerogels are dominated by the large volume fraction of trapped gas in the pores. However, during our measurement for dielectric breakdown, bright spark was observed at the moment of electrical breakdown, indicating a gaseous discharge. Meanwhile, high voltage breakdown occurred in the dense PI solid. Thus, the dielectric breakdown for PI aerogel might be ascribed to the simultaneous actions of high voltage to the trapped air and the dense PI solid. High temperature induced by the air discharge caused the surface ablation of the aerogel. At the same time, the instantaneous high temperature caused the expansion of the trapped air in the aerogel, resulting in the swelling at the surface of the aerogel (Figure 7b). Nevertheless, the high dielectric breakdown strength makes the current PI aerogel to be effective and lightweight dielectric insulators for high-voltage insulating applications.

The broadband dielectric constant (k) and dissipation factor (δ) of PI aerogel in the frequency range of 2–12 GHz were measured at room temperature and the curve is illustrated in Figure 8. The monolithic PI

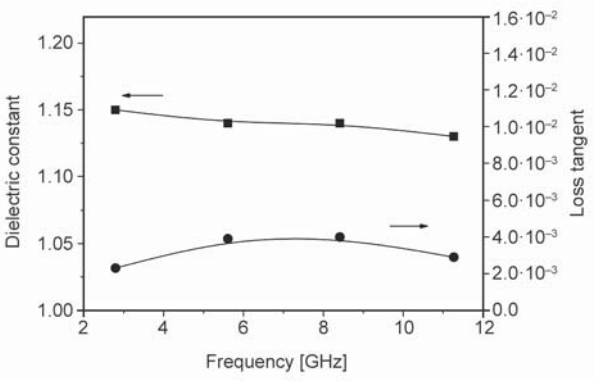

Figure 8. Dielectric constant (k) and loss tangent for PIA as a function of frequency

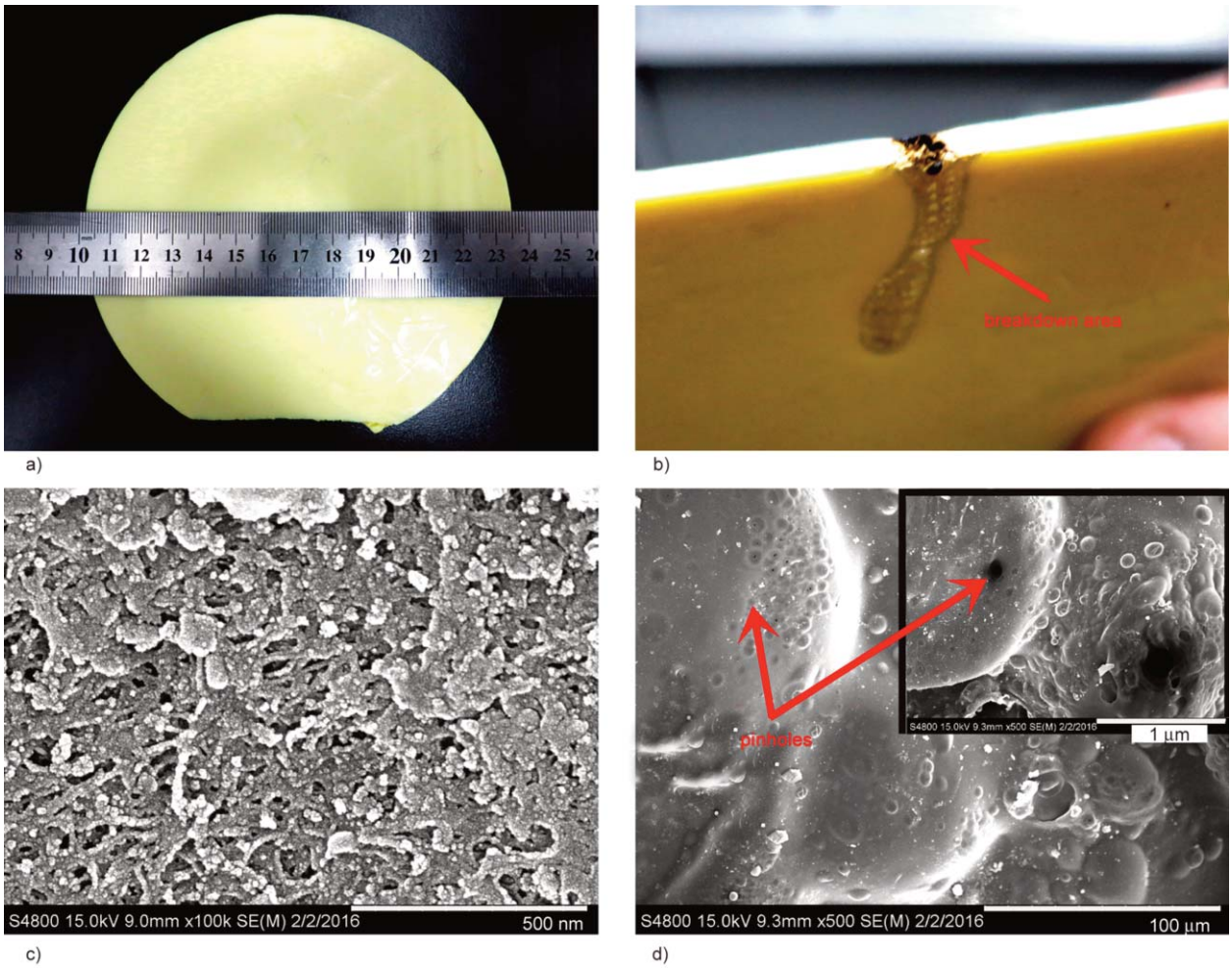

Figure 7. Surface macro- and micro-topographies of PI aerogel before (a) and after (b) dielectric breakdown, (c) SEM image before dielectric breakdown, (d) SEM image after dielectric breakdown

aerogel sample (50 mm×30 mm×2.5 mm) exhibited nearly a constant k value (1.15–1.13) over the entire frequency range. Thus, introduction of air within the PI reduced the k value significantly. The loss tangent (δ) value of PI aerogel also changed in a narrow range of $2.3\cdot10^{-3}$–$4.0\cdot10^{-3}$. The frequency-independent feature of k and δ values for PI aerogel is mainly attributed to the high air loading (porosity: 85.6%) in its structure. The phenomena indicate that the dielectric constant of the PI aerogel is dominated by the trapped air rather than by the solid PI matrix.

4. Conclusions

New PI aerogel was synthesized from BPDA, APBO and OAPS via two-step chemical imidization procedure, followed by $ScCO_2$ drying procedure. The original purpose of molecular design aiming at developing functional PIs with potential applications as ILDs for ULSI was successfully achieved by the derived PI aerogel. Experimental results revealed that the current PI aerogel possessed various advantages compared with the other organic aerogels reported before. First, the polymer exhibited excellent thermal stability and T_g over 350 °C, which is among the most thermally stable polymers reported in the literature. Secondly, the current PI aerogel shows excellent dielectric characteristics, including ultra-low k value and dissipation factor over a broad frequency range of 2–12 GHz, high surface and volume resistivity, and high dielectric strength. The k value around 1.15 at a frequency of 2.75 GHz is one the lowest values for PI materials reported in the literature. Thus, good combined properties make the PI aerogel a good candidate as interlayer dielectric for advanced semiconductor chip interconnection.

Acknowledgements

Financial support from the Fundamental Research Funds of Beijing Jiaotong University (E14JB00130), National Basic Research Program (973 Program) of China (2014CB643605), and National Natural Science Foundation of China (51173188) are gratefully acknowledged.

References

[1] Volksen W., Miller R-D., Dubois G.: Low dielectric constant materials. Chemical Reviews, **110**, 56–110 (2010). DOI: 10.1021/cr9002819

[2] Drobny J-G.: Polymers for electricity and electronics. Materials, properties, and applications. Wiley, New Jersey (2012).

[3] Maier G.: Low dielectric constant polymers for microelectronics. Progress in Polymer Science, **26**, 3–65 (2001). DOI: 10.1016/S0079-6700(00)00043-5

[4] Liaw D-J., Wang K-L., Huang Y-C., Lee K-R., Lai J-Y., Ha S-K.: Advanced polyimide materials: Syntheses, physical properties and applications. Progress in Polymer Science, **37**, 907–974 (2012). DOI: 10.1016/j.progpolymsci.2012.02.005

[5] Liu Y., Qian C., Qu L., Wu Y., Zhang Y., Wu X., Zou B., Chen W., Chen Z., Chi Z., Liu S., Chen X., Xu J.: A bulk dielectric polymer film with intrinsic ultralow dielectric constant and outstanding comprehensive properties. Chemistry of Materials, **27**, 6543–6549 (2015). DOI: 10.1021/acs.chemmater.5b01798

[6] Simpson J-O., St. Clair A-K.: Fundamental insight on developing low dielectric constant polyimides. Thin Solid Films, **308–309**, 480–485 (1997). DOI: 10.1016/S0040-6090(97)00481-1

[7] Kohl P-A.: Low–dielectric constant insulators for future integrated circuits and packages. Chemical and Biomolecular Engineering, **2**, 379–401 (2011). DOI: 10.1146/annurev-chembioeng-061010-114137

[8] Dhara M-G., Banerjee S.: Fluorinated high-performance polymers: Poly(arylene ether)s and aromatic polyimides containing trifluoromethyl groups. Progress in Polymer Science, **35**, 1022–1077 (2010). DOI: 10.1016/j.progpolymsci.2010.04.003

[9] Taki K., Hosokawa K., Takagi S., Mabuchi H., Ohshima M.: Rapid production of ultralow dielectric constant porous polyimide films *via* CO_2-*tert*-amine Zwitterion-induced phase separation and subsequent photopolymerization. Macromolecules, **46**, 2275–2281 (2013). DOI: 10.1021/ma302406m

[10] Carter K. R., DiPietro R-A., Sanchez M-I., Swanson S-A.: Nanoporous polyimides derived from highly fluorinated polyimide/poly(propylene oxide) copolymers. Chemistry of Materials, **13**, 213–221 (2001). DOI: 10.1021/cm990707o

[11] Fu G. D., Zong B. Y., Kang E. T., Neoh K. G., Lin C. C., Liaw D. J.: Nanoporous low-dielectric constant polyimide films *via* poly(amic acid)s with RAFT-graft copolymerized methyl methacrylate side chains. Industrial Engineering Chemistry Research, **43**, 6723–6730 (2004). DOI: 10.1021/ie0498807

[12] Zha J-W., Jia H-J., Wang H-Y., Dang Z-M.: Tailored ultralow dielectric permittivity in high-performance fluorinated polyimide films by adjusting nanoporous characterisitics. The Journal of Physical Chemistry C, **116**, 23676–23681 (2012). DOI: 10.1021/jp305286r

[13] Zhao G., Ishizaka T., Kasai H., Hasegawa M., Furukawa T., Nakanishi H., Oikawa H.: Ultralow-dielectric-constant films prepared from hollow polyimide nanoparticles possessing controllable core sizes. Chemistry of Materials, **21**, 419–424 (2009). DOI: 10.1021/cm802989u

[14] Leu C-M., Chang Y-T., Wei K-H.: Polyimide-side-chain tethered polyhedral oligomeric silsesquioxane nanocomposites for low-dielectric film applications. Chemistry of Materials, **15**, 3721–3727 (2004).
DOI: 10.1021/cm030393b

[15] Nitta S. V., Pisupatti V., Jain A., Wayner Jr P. C., Gill W. N., Plawsky J. L.: Surface modified spin-on xerogel films as interlayer dielectrics. Journal of Vacuum Science and Technology, B, **17**, 205–212 (1999).
DOI: 10.1116/1.590541

[16] Yan P., Zhou B., Du A.: Synthesis of polyimide cross-linked silica aerogels with good acoustic performance. RSC Advances, **4**, 58252–58259 (2014).
DOI: 10.1039/c4ra08846h

[17] Leventis N., Sotiriou-Leventis C., Chandrasekaran N., Mulik S., Larimore Z-J., Lu H-B., Churu G., Mang J-T.: Multifunctional polyurea aerogels from isocyanates and water. A structure–property case study. Chemistry of Materials, **22**, 6692–6710 (2010).
DOI: 10.1021/cm102891d

[18] Bang A., Buback C., Sotiriou-Leventis C., Leventis N.: Flexible aerogels from hyperbranched polyurethanes: Probing the role of molecular rigidity with poly(urethane acrylates) versus poly(urethane norbornenes). Chemistry of Materials, **26**, 6979–6993 (2014).
DOI: 10.1021/cm5031443

[19] Meador M. A. B., Malow E. J., Silva R., Wright S., Quade D., Vivod S. L., Guo H., Guo J., Cakmak M.: Mechanically strong, flexible polyimide aerogels cross-linked with aromatic triamine. ACS Applied Material Interfaces, **4**, 536–544 (2012).
DOI: 10.1021/am2014635

[20] Guo H. Q., Meador M. A. B., McCorkle L., Quade D. J., Guo J., Hamilton B., Cakmak M., Sprowl G.: Polyimide aerogels cross-linked through amine functionalized polyoligomeric silsesquioxane. ACS Applied Material Interfaces, **3**, 546–552 (2011).
DOI: 10.1021/am101123h

[21] Meador M. A. B., Alemán C. R., Hanson K., Ramirez N., Vivod S. L., Wilmoth N., McCorkle L.: Polyimide aerogels with amide cross-Links: A low cost alternative for mechanically strong polymer aerogels. ACS Applied Material Interfaces, **7**, 1240–1249 (2015).
DOI: 10.1021/am507268c

[22] Liu P., Tran T-Q., Fan Z., Duong H. M.: Formation mechanisms and morphological effects on multi-properties of carbon nanotube fibers and their polyimide aerogel-coated composites. Composites Science and Technology, **117**, 114–120 (2015).
DOI: 10.1016/j.compscitech.2015.06.009

[23] Meador M. A. B., Wright S., Sandberg A., Nguyen B. N., van Keuls F. W., Mueller C. H., Rodriguez-Solís R., Miranda F. A.: Low dielectric polyimide aerogels as substrates for lightweight patch antennas. ACS Applied Material Interfaces, **4**, 6346–6353 (2012).
DOI: 10.1021/am301985s

[24] Meador M. A. B., McMillon E., Sandberg A., Barrios E., Wilmoth N. G., Mueller C. H., Miranda F. A.: Dielectric and other properties of polyimide aerogels containing fluorinated blocks. ACS Applied Materials and Interfaces, **6**, 6062–6068 (2014).
DOI: 10.1021/am405106h

[25] Shen D., Liu J., Yang H., Yang S.: Intrinsically highly hydrophobic semi-alicyclic fluorinated polyimide aerogel with ultralow dielectric constants. Chemistry Letters, **42**, 1230–1232 (2013).
DOI: 10.1246/cl.130623

[26] Ko H-H., Chong J. Y-T., Lam D. C. C.: Low-stress ultra-low dielectric porous polymer for high density applications: A review. in 'Proceeding of the 13th IEEE International Conference on Nanotechnology, Beijing, China' 34–38 (2013).
DOI: 10.1109/NANO.2013.6721031

[27] Fukukawa K-I., Shibasaki Y., Ueda M.: A photosensitive semi-alicyclic poly(benzoxazole) with high transparency and low dielectric constant. Macromolecules, **37**, 8256–8261 (2004).
DOI: 10.1021/ma049063i

[28] Liao W-H., Yang S-Y., Hsiao S-T., Wang Y-S., Li S-M., Ma C-C. M., Tien H-W., Zeng S-J.: Effect of octa (aminophenyl) polyhedral oligomeric silsesquioxane functionalized graphene oxide on the mechanical and dielectric properties of polyimide composites. ACS Applied Materials and Interfaces, **6**, 15802–15812 (2014).
DOI: 10.1021/am504342j

[29] Shen D., Liu J., Yang H., Yang S.: Highly thermally resistant and flexible polyimide aerogels containing rigid-rod biphenyl, benzimidazole, and triphenylpyridine moieties: Synthesis and characterization. Chemistry Letters, **42**, 1545–1547 (2013).
DOI: 10.1246/cl.130758

[30] Aegerter M. A., Leventis N., Koebel M. M.: Aerogel handbook. Springer, New York (2011).

[31] Cooper A. I.: Polymer synthesis and processing using supercritical carbon dioxide. Journal of Materials Chemistry, **10**, 207–234 (2000).
DOI: 10.1039/A906486I

[32] Li L., Yalcin B., Nguyen B. N., Meador M. A. B., Cakmak M.: Flexible nanofiber-reinforced aerogel (xerogel) synthesis, manufacture, and characterization. Applied Materials and Interfaces, **1**, 2491–2501 (2009).
DOI: 10.1021/am900451x

[33] Pierre A. C., Pajonk G. M.: Chemistry of aerogels and their applications. Chemical Reviews, **102**, 4243–4265 (2002).
DOI: 10.1021/cr0101306

[34] Hrubesh L. W., Pekala R. W.: Dielectric properties and electronic applications of aerogels. in 'Sol-gel processing and applications' (ed.: Attia Y. A.) Plenum Press, New York, 363–367 (1994).
DOI: 10.1007/978-1-4615-2570-7_31

eXPRESS Polymer Letters Vol.10, No.10 (2016) 799–809
Available online at www.expresspolymlett.com
DOI: 10.3144/expresspolymlett.2016.75

Moisture curable toughened poly(lactide) utilizing vinyltrimethoxysilane based crosslinks

*J. Schneider, K. Bourque, R. Narayan**

Michigan State University, Department of Chemical Engineering and Materials Science, MI 48823 East Lansing, USA

Received 17 February 2016; accepted in revised form 9 May 2016

Abstract. Vinyltrimethoxysilane (VTMOS) was grafted on to the backbone of poly(lactide) (PLA) through a free radical grafting reaction using reactive extrusion (REX) processing. The methoxy groups of the silane provide the modified PLA sites for crosslinking through a moisture induced pathway. VTMOS grafting efficiencies of up to 90% were obtained. The newly created methoxy functionality of the modified PLA readily undergoes hydrolysis and condensation forming siloxane crosslinks in the material. Crosslinking with VTMOS exhibited improved modulus, strength, and impact toughness while showing a decrease in ductility. Incorporating silanol-terminated poly(dimethylsiloxane) (OH-PDMS) resulted in the formation of longer siloxane crosslinks. These samples showed an increase in modulus and impact toughness due to the crosslinking, while the longer siloxane linkages resulted in improved ductility and tensile toughness. This is unusual for polymers toughened through crosslinking reactions. Scanning Electron Microscopy (SEM) of the fractured surfaces showed the presence of these elongated siloxane crosslinks. This enhanced ability for the modified PLA to deform and absorb energy results in the increase in both impact and tensile toughness.

Keywords: *biodegradable polymers, reactive extrusion, free radical grafting, moisture induced crosslinking, PLA*

1. Introduction

Poly(lactide) (PLA) is receiving much attention in the polymer materials space because it is produced from renewable resources and is biodegradable/compostable. Thanks to the commercialization processing improvements of PLA producing companies like NatureWorks, LLC, its cost is around $1/lb, making it an intriguing cost-competitive alternative to traditional petroleum based plastics [1]. However, PLA possesses certain inherent polymer properties such as low impact toughness [2], poor heat [3] and hydrolytic stability [4], and weak melt strength [5] that have prevented it from more wide scale commercial use.

Compared to poly(styrene), PLA has very similar mechanical properties such as tensile strength and modulus, as well as similar brittleness and low impact strength [6]. These limitations of poly(styrene) led to the development of modified high-impact polymers and copolymers (ex. ABS, HIPS) to further its commercial viability. Now in recent years, the toughening of PLA has undergone the same level of interest in effort to develop a toughened PLA. The typical methods of this include plasticization, copolymerization, and melt blending.

Some research has been done utilizing vinyl functionality to graft reactive groups onto PLA's backbone, making it more susceptible to modification. The introduction of new functional groups onto PLA allows for the creation of new materials, with potentially increased properties due to the incorporation of new reactive chemistries. While many different functionalities have been grafted onto PLA, including acrylic acid [7] and acrylamides [8], the most popular method of PLA melt grafting is with maleic an-

*Corresponding author, e-mail: Narayan@egr.msu.edu

hydride. This grafting is typically done using reactive extrusion (REX) processing making it cost-competitive and commercially scalable. Maleic anhydride grafted PLA polymers (MA-*g*-PLA) have been used as compatibilizers for native [9] and thermoplastic starches [10] where they have promoted strong interfacial adhesion and better dispersion for these biocomposites. Other researchers have used MA-*g*-PLA as an reactive intermediary to graft more flexible compounds such as poly(ethylene glycol) [11] and citrate [12] onto PLA to increase its toughness.

PLA can also be toughened by introducing an appropriate level of crosslinking into the material. The two common procedures to crosslink thermoplastic polymers are copolymerization with a multifunctional monomer and introducing reactive compounds onto the polymer backbone. Such reactive compounds include the vinyl functionalities previously described, followed by additional crosslinking steps. Crosslinking through the grafting of a reactive compound route has been commonly done with triallyl isocyanurate (TAIC). This has been performed both in the melt via free radical initiation [13] and crosslinking prefabricated samples via radiation curing [14]. TAIC is a highly reactive material making it difficult to control the extent of grafting. And while crosslinking is an effective method of increasing impact toughness, it typically results in a loss in ductility and therefore a decrease in tensile toughness.

Vinylalkoxysilane grafting appears to be an excellent combination of the two methods. The vinyl functionality can be easily incorporated onto the PLA backbone via free radical grafting in the melt phase, while the alkoxysilane functionality is capable of forming crosslinks through moisture curing. This procedure was first introduced by Dow Corning for the crosslinking of polyolefins and termed the SioPlas method [15]. This two-step method of free radical grafting followed by moisture cured crosslinking increases the chemical and thermal resistance of the polyolefins, while also increasing the crack propagation and impact resistance [16]. The advantages of this crosslinking method compared to other common techniques such as initiation by high energy radiation and peroxides are energy saving, higher productivity, and the crosslinked products contain stable siloxane (Si–O–Si) bonds [17]. However, this method still does result in a loss in ductility. Han *et al.* [18] reported a study adopting this SioPlas method to PLA in which an improvement in thermal stability, hydrolysis resistance, and strength/stiffness properties occurred. The crosslinked PLA showed an increase in tensile strength and modulus along with a decrease in ductility/elongation, similar to SioPlas. In addition, they only achieved very low grafting efficiency (max of 37%). This study used a hot water crosslinking step, which Rahmat *et al.* [19] recently showed leads to excessive hydrolytic degradation of PLA. At long crosslinking times, hydrolytic degradation becomes the dominant mechanism leading to network defects, causing loose gel structures.

In this paper, improvements to the REX processing are discussed in detail and their effects on the grafting efficiency of VTMOS onto PLA are reported. The improvements result in drastically better grafting efficiency and therefore less VTMOS is needed. After process optimization, a silanol-terminated poly (dimethylsiloxane) (OH-PDMS) was added into the system to aid in the crosslinking. This resulted in longer and more flexible crosslinks being formed which had a large positive impact on mechanical properties. Crosslinking was done without the previously used hot water bath to prevent excessive hydrolytic degradation. Tensile and impact properties where determined and the siloxane crosslinking effect was examined.

2. Experimental

2.1. Materials

PLA resin pellets (3051D) with a weight average molecular weight of 150 000 g/mol (PDI = 1.7) and 8% meso-lactide content (T_m = ~155 °C) were purchased from NatureWorks LLC (NE, USA). Vinyltrimethoxysilane (VTMOS, *bp* = 123 °C) and 2,5-Bis(tert-butylperoxy)-2,5-dimethylhexane (Luperox 101) were obtained from Sigma-Aldrich (WI, USA). The silanol terminated polydimethylsiloxane (OH-PDMS) was from Gelest and possessed a molecular weight of ~550 g/mol.

2.2. Compounding and sample preparation

The PLA resin pellets were dried for 24 hours in a 70 °C oven to remove moisture. This is crucial for PLA in extrusion processes because it has a tendency to hydrolytically degrade as a result of back-biting and intermolecular transesterification reactions [20]. The

VTMOS grafting process was carried out using a ZSK 30 mm co-rotating twin screw extruder (Werner Pfleiderer, NJ, USA) with an *L*/*D* ratio of 30. The dried PLA pellets were premixed with the required amounts of VTMOS, OH-PMDS, and Luperox before being fed into the hopper using a gravimetric feeder. All samples were compounded at a throughput of 6 kg/hr, cooled in a water bath, and then pelletized. The pellets were tumbled in a bin with absorbent towels to remove the surface moisture. Some moisture was retained in the sample to promote hydrolysis of the methoxy groups and promote the crosslinking chemistry during downstream processing. The screw speed and temperature profile for all compounding were 125 rpm and 120, 140, 160, 170, 170, 165 °C, respectively. It is necessary for the first temperature zone to be 120 °C or lower to prevent flash evaporation of the VTMOS in the hopper. Previously, Han *et al.* [18] used an initial feed zone temperature of 170 °C and noted very low grafting, even though large percentages were used. This could be because a large amount of it did not even enter the extruder due to flash evaporation as soon as it entered the hopper. This same study used a screw speed of 60 rpm which is rather slow and results in poor mixing. Poor mixing leads to slower reactions, which is another potential reason for the low grafting percentages.

Tensile and impact test specimens were compression molded using a Carver Laboratory Press (IN, USA), immediately after tumble-drying of the pellets. Immediate processing was done to ensure that the crosslinking reaction had not started prior to sample fabrication. The platen were heated to 180 °C and the filled mold was pressed at a minimum of 10 ton for 3 minutes. Cooling water was then turned on to cool the platen. The mold was removed when the temperature reached below 40 °C, or approximately 10 minutes. After removal from the mold, the specimens were placed into a 50 °C oven for 3 days to pull off any residual water and subsequently drive the condensation reaction forward to form the siloxane crosslinks. In the past, this crosslinking step was done by placing the samples in hot water for up to 20 hours, which led to significant degradation of the PLA [19]. Test specimens were stored in a zip-top bag with as much air removed as possible and were allowed to rest for 2 weeks prior to mechanical testing.

2.3. Percent grafting determination

The grafting percent of VTMOS onto PLA was measured immediately after compounding and then again prior to mechanical testing using two different techniques, TGA and proton NMR. In the TGA method, the amount of free or ungrafted VTMOS can be determined by isothermally holding the sample above the boiling point of VTMOS (123 °C), for 20 minutes. At this temperature, the free VTMOS evaporates and the weight loss represents the un-grafted VTMOS. Also at this temperature, PLA begins to slightly decompose as seen by a gradual negative slope in the weight percent versus time graph. To correct for this, the slope of the line in the 18–20 minute range is extrapolated back to time zero and is used for determining the percent grafting. The slope is calculated at the end of the isotherm since all free VTMOS has been removed and a steady slope is reached. The extrapolated time zero weight % is the grafted VTMOS and PLA percentage in the sample. Therefore the weight % difference from the extrapolated and starting values, is due to the loss of the ungrafted VTMOS.

Proton NMR was also used to establish percent grafting. The ratio of the vinyl to methoxy proton integrations from neat VTMOS was compared to that of the reacted material. Neat VTMOS shows an integration ratio of 1:3 for vinyl to methoxy protons. So as the VTMOS grafts onto PLA through the reaction of the vinyl group, the signal corresponding to this vinyl group decreases. This results in a decrease in the vinyl to methoxy proton integration ratio. Therefore percent grafting can be calculated with NMR by Equation (1):

$$Grafting\,[\%] = \frac{[v{:}m]_{neat} - [v{:}m]_{exp}}{[v{:}m]_{neat}} \cdot 100 \qquad (1)$$

where $[v{:}m]_{neat}$ and $[v{:}m]_{exp}$ are the integration ratios corresponding to the vinyl and methoxy groups of VTMOS for the pure/neat material and the experimentally reacted materials, respectively. For the pure material, this in theory should be 1:3, however in practice it is typically slightly higher due to the hydrolysis of some methoxy groups.

NMR was primarily used to verify the grafting percentage determinations obtained by TGA. The grafting percentages calculated by TGA and NMR showed less than 5% statistical variation. Therefore it was con-

cluded that TGA can accurately determine VTMOS grafting efficiency, and was then used as the primary method to determine grafting. This TGA/NMR method for experimentally determining VTMOS grafting efficiency has been used to monitor/determine VTMOS grafting onto soybean oil [21].

2.4. Mechanical testing

The tensile properties of the siloxane crosslinked samples were tested using a United Testing Systems (CA, USA) SFM-20 load frame with a 1000 lb (4448 N) load cell. The dog-bone shaped specimens had a 2 inch gage length and cross-sectional dimensions of 0.5×0.125 inches (12.7×3.175 mm). The testing rate used was 0.2 inch/min (5.08 mm/min), which resulted in most failures occurring between 30–120 seconds. A minimum of 5 replicates were tested for each compound.

The notched IZOD impact properties were determined using a TMI pendulum impact tester (Testing Machines, Inc., DE, USA), following ASTM D256 utilizing a 1 ft-lb (0.113 Nm) pendulum. The specimens had cross-sectional dimensions of 0.5×0.125 (12.7×3.175 mm) inches, and the notch was 0.1 (0.254 mm) inch deep. After notching, the specimens were allowed to rest at least 24 hours prior to impact testing. A minimum of 5 replicates were impact tested for each sample set.

2.5. Morphology (SEM)

The morphologies of the siloxane crosslinked samples were studied using a JEOL 6610V (Japan Electron Optics Laboratories, Japan) Scanning Electron Microscope (SEM). The fractured surfaces following tensile and impact testing were analyzed after coating with osmium.

3. Results and discussion

3.1. Determination of VTMOS grafting

The previous study by Han *et al.* [18] showed that VTMOS can be grafted onto the backbone of PLA using a free radical initiator through reactive extrusion (REX) processing. However, with the processing conditions used, very low grafting percentages resulted. Due to this low grafting efficiency, these researchers used high concentrations of VTMOS, up to 8 wt%. This VTMOS concentration results in a molar ratio of ~70 VTMOS per PLA chain (based on a number average molecular weight of 120 000 g/mol), which is excessive and could lead to an extremely high crosslink density as well as a dramatic increase in the cost of the final material. Therefore, the initial portion of this study was to optimize the process to give enhanced grafting efficiency for our materials while using lower concentrations of VTMOS, and thereby reducing costs.

In attempt to increase the grafting efficiency, a lower VTMOS concentration (0.5 and 1.0 wt%), a lower feed zone temperature (starting at 120 °C – so no VTMOS loss due to evaporation), and higher screw speed (125 rpm) were used. Initially a higher free radical initiator (Luperox) concentration was also used (0.5 wt%), however this resulted in a rigid and highly brittle thermoset material (incapable of dissolving in solvent). This was caused by an unwanted additional reaction of Si–O–C linkages formed through the methoxy groups and PLA during extrusion. This two sided reaction resulted in the formation of the thermoset. Reducing the Luperox concentration to 0.25 and 0.1 wt% yielded products with slightly lower grafting efficiencies of 87.49 and 82.91%, respectively. However, this reaction was without the unwanted Si–O–C linkages responsible for the formation rigid thermoset. Both samples were fully dissolvable in solvent, indicating that no crosslinking occurred through REX, but rather the grafting was done solely via the vinyl attachment onto PLA.

The mechanism for the vinyl attachment of VTMOS onto the PLA backbone is shown in Figure 1. This mechanism for melt free radical grafting utilizing vinyl functionality is well accepted and has been used to incorporate many different chemical species onto PLA. The first step is the thermal decomposition of a free radical initiator (Luperox) resulting in the production of radicals. The generated radical abstracts hydrogen from the α-carbon, creating radicals on the PLA chain. This hydrogen abstraction of PLA was first shown by Avella *et al.* [22] in the reaction with butyl acrylate. The PLA radicals are then capable of coupling with radicals on the vinyl group of VTMOS, as shown below. A potential side reaction involves the PLA radicals coupling with another material, the initiator radical, hydrogen, or another polymer radical, potentially leading to an unwanted result such as β-scission, which is noted by a molecular weight

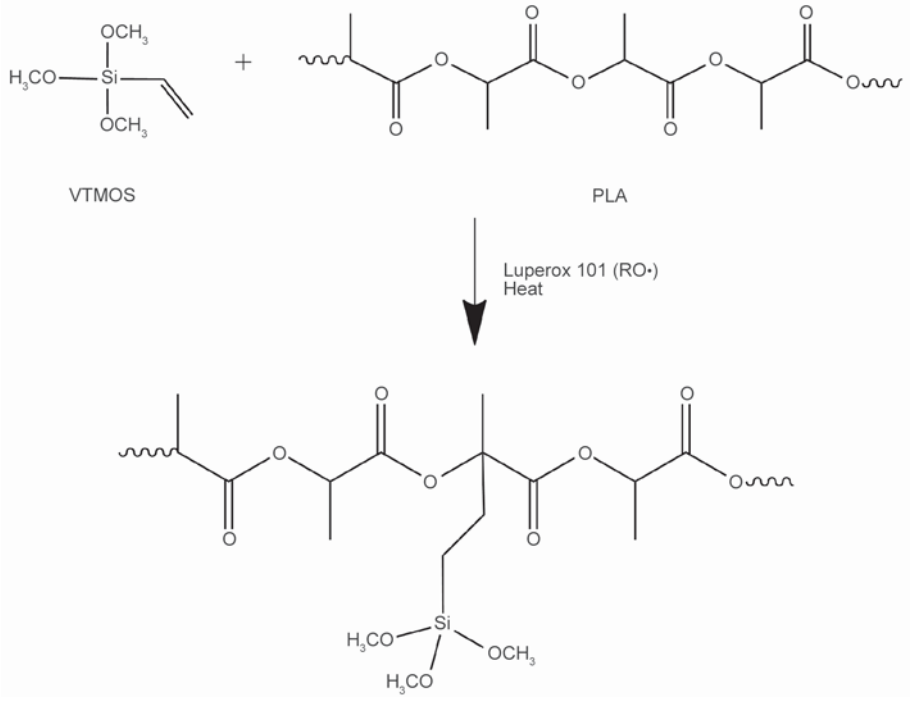

Figure 1. A schematic mechanism for the free radical initiated grafting of VTMOS on PLA

decrease in processing. The vinyl grafting efficiency was determined by NMR using the decrease in the vinyl to methoxy proton integration ratio as well as a slight change in the ratio of the PLA peaks corresponding to the methyl hydrogens and the hydrogen on the C-backbone. These two components prove that VTMOS is grafted onto the PLA backbone as described in Figure 1.

Following VTMOS grafting, a moisture induced crosslinking of the grafted polymers can occur. First the methoxy groups of VTMOS readily hydrolyze in the presence of water, forming silanol functionality (Si–OH). The silanols condense to form siloxane linkages leading to the formation of crosslinked compounds. These short siloxane linkages from the coupling of two VTMOS molecules is not flexible enough to impart any toughening benefit. In fact, just crosslinking PLA with VTMOS yields a material with less ductility. Therefore, in effort to lengthen the siloxane linkages and create a true toughening effect, a silanol functionalized PDMS (OH-PDMS) was incorporated to take part in the condensation portion of the crosslinking reaction. This hydrolysis and condensation crosslinking reaction is shown in Figure 2.

After fabrication of test specimens and the following moisture cure, samples were again analyzed to determine grafting efficiency and for the formation of gels. Over this crosslinking period, the compounds experienced very little change in grafting of VTMOS and some samples showed a slight increase. This increase in grafting can be explained by some of the free, or unreacted VTMOS being incorporated in the crosslinking reaction thereby becoming part of the crosslinked material. A few of the samples showed a decrease in grafting which can be attributed to the weight loss of methanol during testing, which is created through the hydrolysis step. VTMOS can also migrate to the surface and evaporate instead of crosslinking. The grafting percentages for the compounds after REX and after the crosslinking period are shown in Table 1. For the VTMOS only samples, the higher Luperox concentration results in slightly higher grafting. With the addition of OH-PDMS, the opposite trend occurs where 0.1% Luperox results in higher grafting. The other trend to notice is that there was lower grafting efficiency for the 0.5 wt% VTMOS samples compared to the 1 wt% VTMOS samples. This is probably due to small losses of VTMOS in processing due to evaporation, where when using less material, the small losses result in larger percentages.

After the moisture curing step, the compounds were again placed in dichloromethane to dissolve. All of the samples experienced gel-swell rather than dissolving. This indicates that the siloxane crosslinking had in fact occurred through the hydrolysis and con-

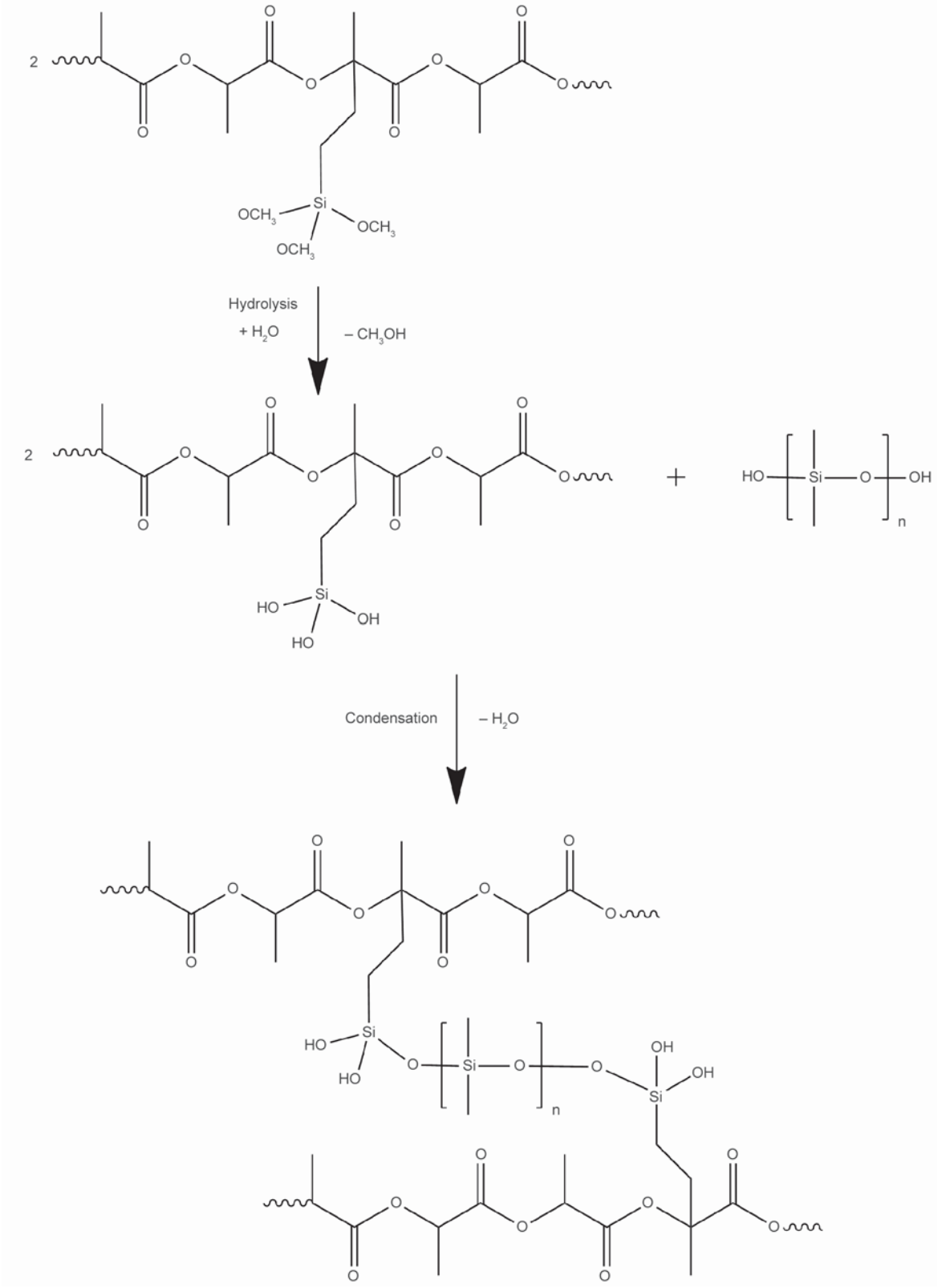

Figure 2. A mechanism showing the hydrolysis of the methoxy groups and the condensation resulting in siloxane crosslinked PLA

densation steps shown. The REX procedure used was shown to be effective in its ability to enhance VTMOS grafting efficiency onto PLA compared to previous reports.

3.2. Mechanical properties

The tensile properties of neat and REX modified PLA samples are shown in Table 2. The yield stress (σ_y) was taken as the maximum stress value achieved

Table 1. Determination of percent VTMOS grafting post REX processing and post two week crosslinking period

% VTMOS	% OH-PDMS	% Luperox	% Graft.$_{intial}$	% Graft.$_{2\ weeks}$
0.5	1	0.10	78.2	70.5
0.5	1	0.25	66.1	75.1
0.5	3	0.10	63.5	50.3
0.5	3	0.25	63.7	73.1
1.0	1	0.10	89.5	83.6
1.0	1	0.25	86.4	86.5
1.0	3	0.10	79.3	77.8
1.0	3	0.25	76.4	79.8
1.0	0	0.10	82.9	79.9
1.0	0	0.25	87.4	86.8

for the specimens and the elongation at fracture (ε_f) is the strain at break. The modulus (E) of the specimens was determined by measuring the slope of the stress-strain curve in the linear elastic region, within the first 0.5% strain. It should first be mentioned that the mechanical properties experimentally determined for neat PLA are comparable to the properties reported by NatureWorks in their technical data sheet. As mentioned earlier, crosslinking PLA with only VTMOS results in a decrease in ductility. This was observed in our results as the test specimens showed an increased modulus coupled with a loss in elongation. This is due to the formation of a crosslinked network where the crosslinks are short, and rather stiff in nature. As OH-PDMS is added and incorporates in the crosslinking, the siloxane crosslinks become longer and much more flexible due to the physical characteristics of this bond. The short siloxane linkages formed by the coupling of VTMOS does not impart flexibility like the longer OH-PDMS chains. With an increase in OH-PDMS content, an increase in elongation is experienced along with a slight reduction in yield stress. In fact, the VTMOS only specimens did not show a true yield stress but rather an increase in stress until fracture, and the neat PLA fractured immediately following yielding. When OH-PDMS is incorporated, a true yielding is experienced and examples of such samples are shown in Figure 3. However, it is possible that some of the increase in elongation observed for the samples with OH-PDMS is due to a lubricating effect from un-reacted OH-PDMS.

From Figure 3 it is clear to see that by incorporating OH-PDMS, much higher elongations to failure are experienced. However, the very unique result from this modification is that the elongation was increased

Table 2. Tensile properties of the siloxane crosslinked PLA samples

% VTMOS	% OH-PDMS	% Luperox	E [GPa]	σ_y [MPa]	ε_f [%]
0.5	1	0.10	3.40	54.68	53.07
0.5	1	0.25	3.25	55.02	5.94
0.5	3	0.10	3.67	44.95	9.97
0.5	3	0.25	3.07	45.51	4.45
1.0	1	0.10	3.43	55.36	3.59
1.0	1	0.25	3.33	53.16	4.05
1.0	3	0.10	3.71	45.44	3.24
1.0	3	0.25	3.48	45.30	4.49
1.0	0	0.10	3.73	58.67	2.40
1.0	0	0.25	3.46	55.92	1.92
0	0	0	2.62	58.67	2.93

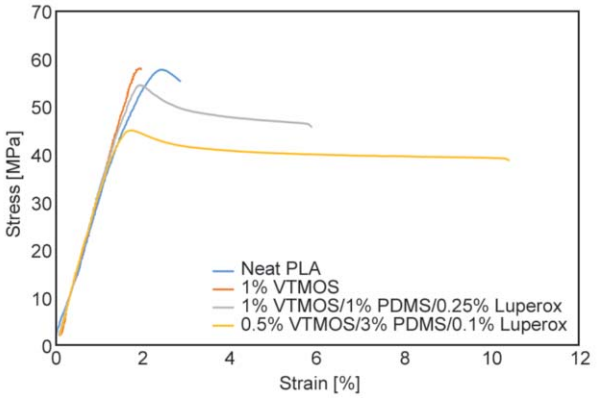

Figure 3. Representative stress-strain curves of neat PLA, VTMOS crosslinked PLA, and crosslinked samples incorporating 1 and 3% OH-PDMS

without reduction in moduli of the specimens. In fact, the crosslinked samples with OH-PDMS showed a significantly higher modulus than neat PLA. This is caused by crosslinking a stiff material with a very ductile polymer. The crosslinked structure initially provides rigidity, raising the modulus. Yet these ductile crosslinks are capable of stretching under the applied load until they reach their limit, where the PLA then fails. This explains why even with increased

elongation, a brittle failure was still observed. All tensile specimens showed a flat and smooth fracture surface, indicating a brittle fracture. The OH-PDMS crosslinked samples are both stiffer and more ductile in comparison to neat PLA, resulting a significant increase in the tensile toughness, as seen by the area under the curves. The addition of OH-PDMS does result in a slight reduction in ultimate stress, but with the increases in elongation and modulus, an increase in toughness is still experienced.

Another thing of note is how the crosslink density affects the tensile properties. Assuming 80% grafting efficiency, 0.5 and 1 wt% of VTMOS results in ~4 and ~8 VTMOS groups grafting onto each PLA chain, respectively. Therefore these samples experience different crosslink densities. The lower crosslink density samples (0.5 wt% VTMOS) show higher elongations to failure, while the high crosslink density samples have a higher modulus. This fits with theory and is what would be expected when dealing with crosslinked samples. The higher amount of crosslinks in a specific area result in the material not being able to stretch and deform as much, coincidentally resulting in a higher modulus. However, regardless of the VTMOS content in the samples, a significant increase in tensile toughness was observed with the presence of OH-PDMS due to increases in both elongation to failure and modulus compared to neat PLA.

IZOD Impact testing also showed a significant increase in toughness (~25%) for the modified samples. However there was no discernible trend based on VTMOS, OH-PDMS, or Luperox concentrations, as seen in Table 3. It appears that with such a dynamic and fast fracture, the extent of crosslinking (VTMOS concentration) and the crosslink length (OH-PDMS concentration) has no direct effect. But rather, a siloxane crosslinked sample of any nature shows approximately a 25% increase in impact toughness over neat PLA. The quick fracture likely doesn't allow for the longer siloxane linkages to stretch and absorb more energy, yielding a higher toughness as is seen with higher OH-PDMS concentrations in tensile testing. But rather the presence of these siloxane crosslinks is enough to increase the impact toughness compared to neat PLA.

3.3. Morphology

The tested samples were analyzed using SEM to determine if the siloxane crosslinks affected the morphology of the fractured surfaces. Figure 4 shows the fractured surfaces of select samples following tensile testing. The neat PLA sample in Figure 4a shows an extremely rough surface in comparison to the others which are just VTMOS crosslinked (Figure 4b) and containing both VTMOS and OH-PDMS crosslinking (Figure 4c). This extremely rough surface corresponds to the brittle fracture experienced by the neat PLA samples during testing. Not only do the siloxane crosslinked samples exhibit a smoother fracture surface but they show siloxane pullout. In these samples, small holes (black circles) of where the siloxane was pulled out are visible along with the analogous opposite, the stretched siloxane (white circles). The sample containing OH-PDMS shows the presence of long white strands which are most likely the long siloxane linkages from the PDMS polymers.

The morphologies of the impact test samples are shown in Figure 5. All of the fractured surfaces exhibited a rippled pattern morphology, seen by the

Table 3. Notched IZOD impact toughness of siloxane crosslinked samples compared to neat PLA

% VTMOS	% OH-PDMS	% Luperox	Impact energy [J/m]	Standard deviation	% Increase vs neat PLA
0.5	1	0.10	26.71	0.35	22.6
0.5	1	0.25	28.36	0.29	30.2
0.5	3	0.10	27.14	0.66	24.6
0.5	3	0.25	27.30	0.44	25.3
1.0	1	0.10	27.51	1.05	26.3
1.0	1	0.25	27.51	0.61	26.3
1.0	3	0.10	27.45	0.08	26.0
1.0	3	0.25	25.39	0.50	16.5
1.0	0	0.10	26.71	0.25	22.6
1.0	0	0.25	27.83	0.36	27.7
0	0	0	21.78	2.86	0

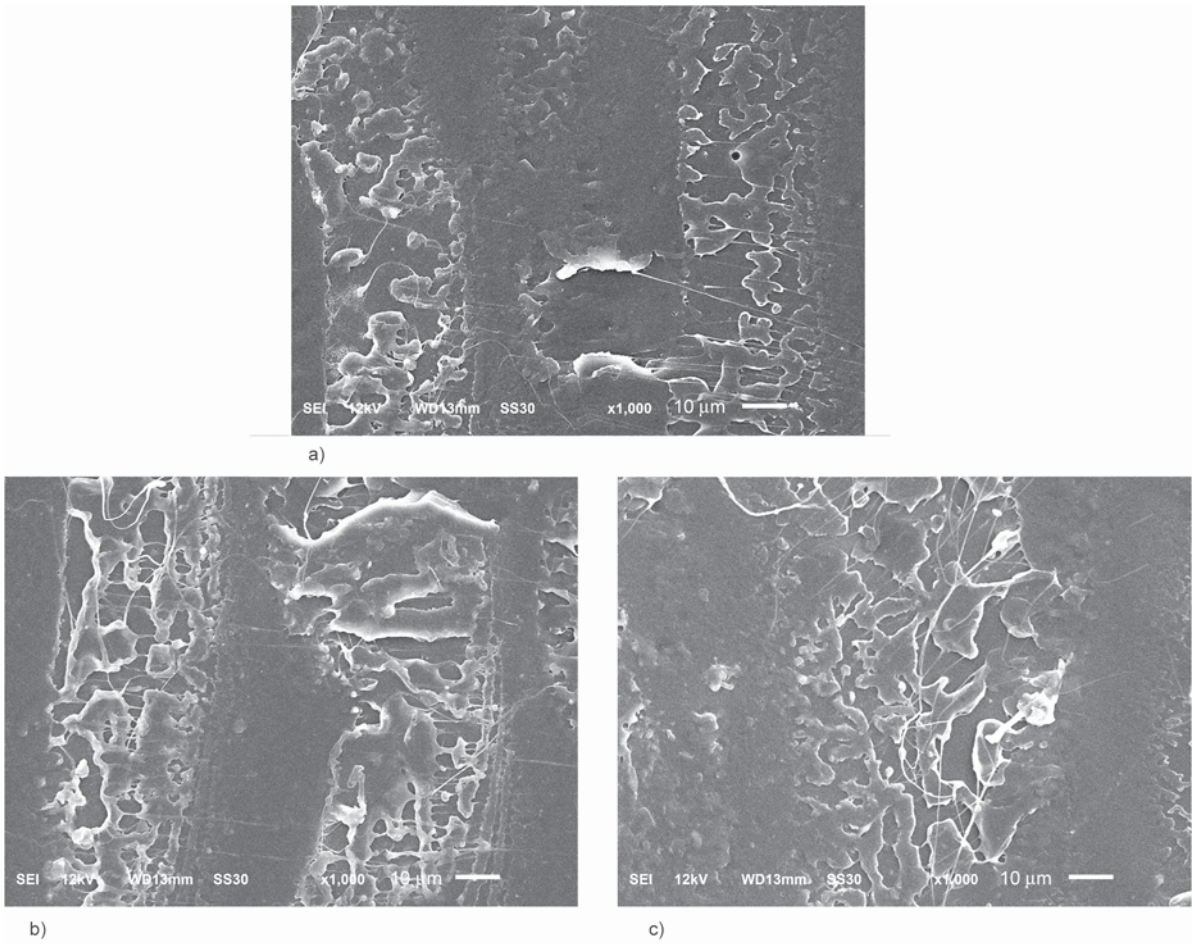

Figure 4. SEM micrographs of the tensile fractured surfaces of a) neat PLA, b) 1% VTMOS – 0.25% Luperox, and c) 0.5% VTMOS – 3% OH-PDMS – 0.1% Luperox samples

vertical columns in the figure. The crosslinked samples show more visual connectivity of the raised sections of the surface, which are from the crosslinking. For the sample with OH-PDMS, the same long linkages are visible as seen in the tensile samples, due to the longer siloxane crosslinks. This added connectivity and ability to deform prior to fracture is the cause of the increase in impact energy.

4. Conclusions

VTMOS was grafted onto PLA using REX processing and moisture cured to form a siloxane crosslinked PLA material. Process improvements compared to a previous study resulted in greater than a two fold increase in grafting efficiency of VTMOS onto the PLA backbone. This resulted in less VTMOS used, lowering the cost of the final product. OH-PDMS was added to lengthen the siloxane crosslinks, resulting in improved tensile toughness. The samples crosslinked with only VTMOS showed improvements in modulus, strength, and impact properties with a decrease in ductility, as previously reported. However, by incorporating OH-PDMS into the crosslinking reaction, not only did an increase in modulus and impact toughness occur compared to neat PLA, but increased elongation to failure was observed resulting in the improvement in tensile toughness. SEM of the fractured surfaces showed the presence of the stretched siloxane crosslinks for the impact samples and siloxane pullout for the tensile samples. This enhanced ability for the material to deform and absorb energy gives reason for the increase in toughness.

References

[1] Auras R., Harte B., Selke S.: An overview of polylactides as packaging materials. Macromolecular Bioscience, **4**, 835–864 (2004).
DOI: 10.1002/mabi.200400043

[2] Jacobsen S., Fritz H. G.: Plasticizing polylactide – The effect of different plasticizers on the mechanical properties. Polymer Engineering and Science, **39**, 1303–1310 (1999).
DOI: 10.1002/pen.11517

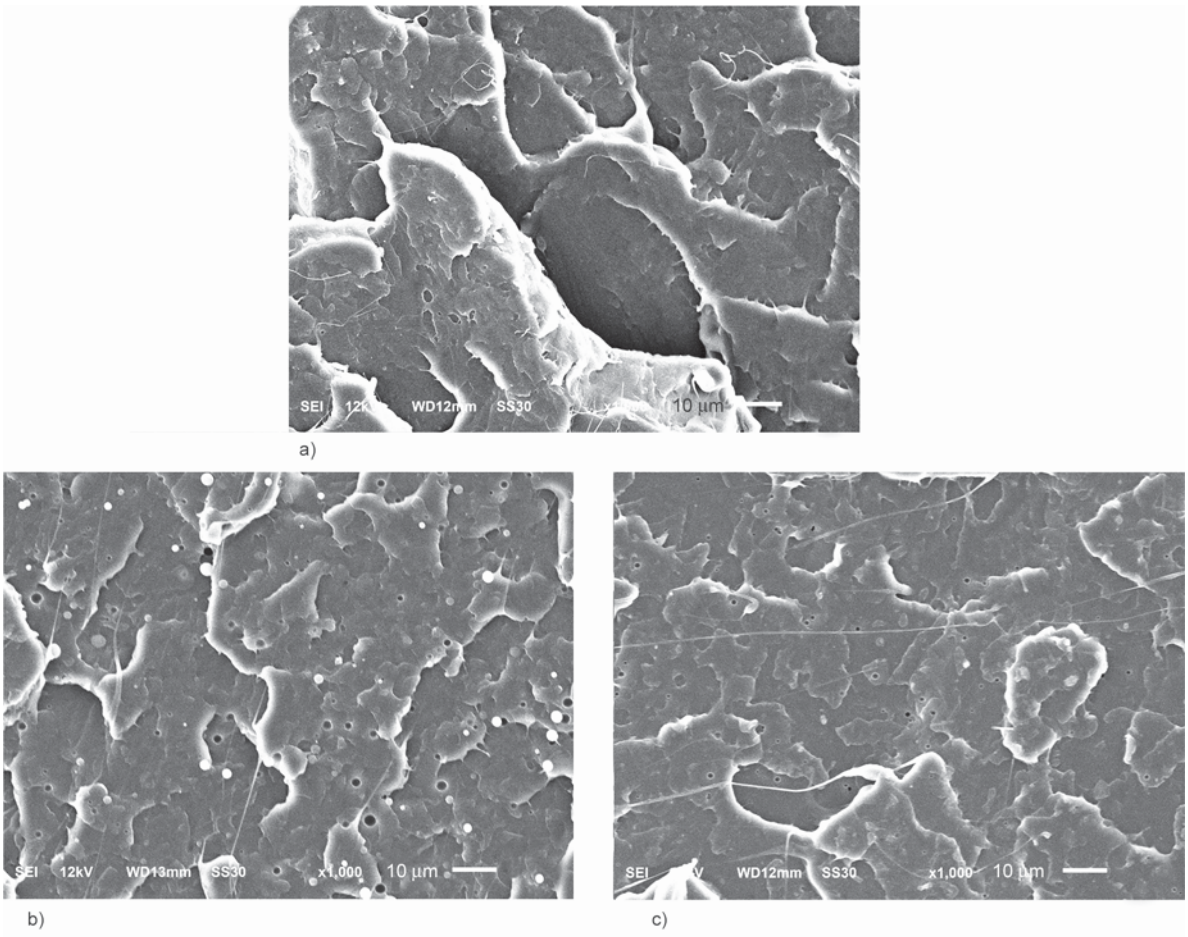

Figure 5. SEM micrographs of the impact test fracture surfaces of a) neat PLA, b) 1% VTMOS – 0.25% Luperox, and c) 1% VTMOS – 1% OH-PDMS – 0.1% Luperox samples

[3] Jamshidi K., Hyon S-H., Ikada Y.: Thermal characterization of polylactides. Polymer, **29**, 2229–2234 (1988). DOI: 10.1016/0032-3861(88)90116-4

[4] De Paula E. L., Mano V., Pereira F. V.: Influence of cellulose nanowhiskers on the hydrolytic degradation behavior of poly(D,L-lactide). Polymer Degradation and Stability, **96**, 1631–1638 (2011). DOI: 10.1016/j.polymdegradstab.2011.06.006

[5] Dorgan J. R., Janzen J., Clayton M. P., Hait S. B., Knauss D. M.: Melt rheology of variable L-content poly (lactic acid). Journal of Rheology, **49**, 607–619 (2005). DOI: 10.1122/1.1896957

[6] Raquez J-M., Habibi Y., Murariu M., Dubois P.: Polylactide (PLA)-based nanocomposites. Progress in Polymer Science, **38**, 1504–1542 (2013). DOI: 10.1016/j.progpolymsci.2013.05.014

[7] Wu C-S.: Improving polylactide/starch biocomposites by grafting polylactide with acrylic acid – Characterization and biodegradability assessment. Macromolecular Bioscience, **5**, 352–361 (2005). DOI: 10.1002/mabi.200400159

[8] Zare A., Morshed M., Bagheri R., Karimi K.: Effect of various parameters on the chemical grafting of amide monomers to poly(lactic acid). Fibers and Polymers, **14**, 1783–1793 (2013). DOI: 10.1007/s12221-013-1783-y

[9] Carlson D., Nie L., Narayan R., Dubois P.: Maleation of polylactide (PLA) by reactive extrusion. Journal of Applied Polymer Science, **72**, 477–485 (1999). DOI: 10.1002/(SICI)1097-4628(19990425)72:4<477::AID-APP3>3.0.CO;2-Q

[10] Huneault M. A., Li H.: Morphology and properties of compatibilized polylactide/thermoplastic starch blends. Polymer, **48**, 270–280 (2007). DOI: 10.1016/j.polymer.2006.11.023

[11] Hassouna F., Raquez J-M., Addiego F., Dubois P., Toniazzo V., Ruch D.: New approach on the development of plasticized polylactide (PLA): Grafting of poly(ethylene glycol) (PEG) via reactive extrusion. European Polymer Journal, **47**, 2134–2144 (2011). DOI: 10.1016/j.eurpolymj.2011.08.001

[12] Hassouna F., Raquez J-M., Addiego F., Toniazzo V., Dubois P., Ruch D.: New development on plasticized poly(lactide): Chemical grafting of citrate on PLA by reactive extrusion. European Polymer Journal, **48**, 404–415 (2012). DOI: 10.1016/j.eurpolymj.2011.12.001

[13] Yang S-L., Wu Z-H., Yang W., Yang M-B.: Thermal and mechanical properties of chemical crosslinked polylactide (PLA). Polymer Testing, **27**, 957–963 (2008). DOI: 10.1016/j.polymertesting.2008.08.009

[14] Quynh T. M., Mitomo H., Nagasawa N., Wada Y., Yoshii F., Tamada M.: Properties of crosslinked polylactides (PLLA & PDLA) by radiation and its biodegradability. European Polymer Journal, **43**, 1779–1785 (2007). DOI: 10.1016/j.eurpolymj.2007.03.007

[15] Scott H. G.: Cross-linking of a polyolefin with a silane. U.S. Patent 3646155 A, USA (1972).

[16] Morshedian J., Hoseinpour P. M.: Polyethylene crosslinking by two-step silane method: A review. Iranian Polymer Journal, **18**, 103–128 (2009).

[17] Chen T., Wang J., Shi P., Li Q., Wu C.: Effect of hot water and water-carrying agent on the properties of silane-water crosslinked linear low density polyethylene. International Polymer Processing, **28**, 180–187 (2013). DOI: 10.3139/217.2672

[18] Han C., Bian J., Liu H., Han L., Wang S., Dong L., Chen S.: An investigation of the effect of silane water-crosslinking on the properties of poly(L-lactide). Polymer International, **59**, 695–703 (2010). DOI: 10.1002/pi.2760

[19] Rahmat M., Ghasemi I., Karrabi M., Azizi H., Zandi M., Riahinezhad M.: Silane crosslinking of poly(lactic acid): The effect of simultaneous hydrolytic degradation. Express Polymer Letters, **9,** 1133–1141 (2015). DOI: 10.3144/expresspolymlett.2015.101

[20] Raquez J-M., Narayan R., Dubois P.: Recent advances in reactive extrusion processing of biodegradable polymer-based compositions. Macromolecular Materials and Engineering, **293**, 447–470 (2008). DOI: 10.1002/mame.200700395

[21] Tambe C., Dewesthale S., Shi X., Graiver D., Narayan R.: Silylation of non-terminal double bonds of natural oils. Silicon, **8**, 87–98 (2016). DOI: 10.1007/s12633-015-9299-2

[22] Avella M., Errico M. E., Immirzi B., Malinconico M., Martuscelli E., Paolillo L., Falcigno L.: Radical polymerization of poly(butyl acrylate) in the presence of poly(L-lactic acid), 1. Synthesis, characterization and properties of blends. Die Angewandte Makromolekulare Chemie, **246**, 49–63 (1997). DOI: 10.1002/apmc.1997.052460104

eXPRESS Polymer Letters Vol.10, No.10 (2016) 810–821
Available online at www.expresspolymlett.com
DOI: 10.3144/expresspolymlett.2016.76

Synthesis of cationic star polymers by simplified electrochemically mediated ATRP

*P. Chmielarz**

Department of Physical Chemistry, Faculty of Chemistry, Rzeszów University of Technology, Al. Powstańców Warszawy 6, 35-959 Rzeszów, Poland

Received 23 March 2016; accepted in revised form 16 May 2016

Abstract. Cyclodextrin-based cationic star polymers were synthesized using β-cyclodextrin (β-CD) core, and 2-(dimethylamino)ethyl methacrylate (DMAEMA) as hydrophilic arms. Star-shaped polymers were prepared *via* a simplified electrochemically mediated ATRP (*se*ATRP) under potentiostatic and galvanostatic conditions. The polymerization results showed molecular weight (MW) evolution close to theoretical values, and maintained narrow molecular weight distribution (MWD) of obtained stars. The rate of the polymerizations was controlled by applying more positive potential values thereby suppressing star-star coupling reactions. Successful chain extension of the ω-functional arms with a hydrophobic *n*-butyl acrylate (BA) formed star block copolymers and confirmed the living nature of the β-CD-PDMAEMA star polymers prepared by *se*ATRP. Novelty of this work is that the β-CD-PDMAEMA-*b*-PBA cationic star block copolymers were synthesized for the first time *via se*ATRP procedure, utilizing only 40 ppm of catalyst complex. The results from ^{1}H NMR spectral studies support the formation of cationic star (co)polymers.

Keywords: *polymer synthesis, seATRP, amphiphilic star copolymers*

1. Introduction

Atom transfer radical polymerization (ATRP) is proven to be one of the most versatile reversible deactivation radical polymerization (RDRP) methods that enables the preparation of polymers with controlled molecular weights (MWs), narrow molecular weight distributions (M_w/M_n, MWDs), and targeted degrees of polymerization (DP) [1–13]. The advent of low amount catalyst ATRP system, such as simplified electrochemically mediated ATRP (*se*ATRP) [14] offers more environmentally friendly reaction conditions for the synthesis of polymers [15]. In *se*ATRP a desired amount of the catalyst complex ($X–Cu^{II}/L$) can be electrochemically reduced to (Cu^{I}/L) activators to start a controlled polymerization [16]. The reduced activator then spreads out into reaction mixture by vigorous stirring, and reacts with initiators (P–X) to form radical species ($P^{\bullet}$) and is oxidized back to ($X–Cu^{II}/L$). Consequently, the radical species propagate to form polymeric chains by reacting with monomers (M), or are deactivated back to the dormant species ($P_n–X$) (Figure 1) [14, 15, 17, 18].

This method has been applied to hydrophobic (meth) acrylates [14, 15, 19–26], and hydrophilic (meth)acrylates and (meth)acrylamides [14, 16–18, 25, 27–31] for the synthesis of well-defined polymeric architec-

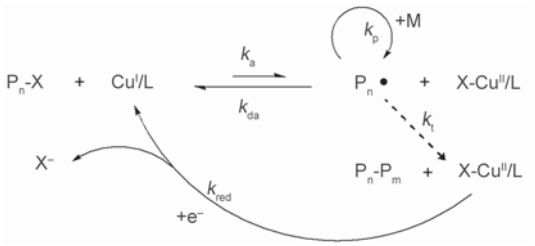

Figure 1. Mechanism of *se*ATRP [19]

*Corresponding author, e-mail: : p_chmiel@prz.edu.pl

tures. Star-shaped cationic polymers, consisting of multiple arms linked to a central β-cyclodextrin (β-CD) core, have recently attracted much attention, because of their dense branched architecture with moderate flexibility, tunable properties like solubility, chemically crosslinked structure, temperature or pH sensitivity, which could be manipulated by the parameters such as the block composition, MW, and arm number [32–44].

Amphiphilic star copolymers composed of poly(2-dimethylaminoethyl methacrylate)-*block*-poly(*n*-butyl acrylate) (PDMAEMA-*b*-PBA) arms covalently linked to a β-CD core are especially interesting, because they can be used in biomedical applications, including drug delivery and tissue engineering. PDMAEMA is the most extensively studied pH-responsive polymer [45–50], because it is able to function as the pH-responsive component as it has a nitrogen moiety, which can be protonated by lowering the pH of the solution [48, 49], and shows pH-dependent lower critical solution temperature behavior [45] and upper critical solution temperature behavior at low temperatures in the presence of multivalent counter ions [47]. Furthermore PBA is an industrially important polymer because of its low glass-transition temperature, durability, and potential use as a soft segment in thermoplastic elastomers [51, 52].

The main objective of this article is to report the first example of the preparation of well-defined star-shaped cationic polymers, consisting of the β-CD core and the respective PDMAEMA and PDMAEMA-*b*-PBA arms by *se*ATRP, under both potentiostatic and galvanostatic conditions. In this case, the arm of the star polymer is composed of a cationic PDMAEMA block and a hydrophobic PBA block. It was presented that polymerization conditions were optimized (including the effect of applied potential on the polymerization behavior) to provide fast reactions while employing low catalyst concentrations and preparation of star copolymers with narrow MWDs. Therefore, well-defined cationic block star copolymers, with a β-CD core were successfully produced through appropriate selection of experimental conditions.

2. Experimental section

2.1. Materials

β-Cyclodextrin (β-CD, M_n = 1,135), 2-bromoisobutyryl bromide (BriBBr, 98%), *N*-methyl-2-pyrrolidone (NMP, >99%), dichloromethane (DCM, >99.5%), *n*-hexane (95%), sodium bicarbonate (>99.7%), tetrabutylammonium perchlorate (TBAP, >98%), copper(II) bromide ($Cu^{II}Br_2$, 99.999%), and methylated cellulose (Tylose, MH = 300) were purchased from Aldrich, USA. *N*,*N*-Dimethylformamide (DMF, 99.9%) was purchased from Acros, Belgium. These reagents were used without further purification. Tris(2-pyridylmethyl)amine (TPMA) was prepared according to a published procedure [53]. Stock solutions of $Cu^{II}Br_2$ and TPMA were prepared according to a previously described in reference [18]. The β-CD-Br_{21} ATRP initiator was prepared by reacting β-CD with BriBBr in NMP according to procedure described in reference [54] and characterized according to our previous work [15]. 2-(Dimethylamino)ethyl methacrylate (DMAEMA; 98%; Sigma-Aldrich, USA) and *n*-butyl acrylate (BA; >99%; Sigma-Aldrich, USA) were passed through a column filled with basic alumina prior to use to remove any inhibitor. Platinum (Pt) wire, Pt gauge mesh and Pt disk (3 mm diameter, Gamry) were purchased from Alfa Aesar, USA. All cyclic voltammetry (CVs) and preparative electrolysis were conducted in electrochemical cell kit (Gamry, USA).

2.2. Analysis

^{1}H NMR spectra in $CDCl_3$ were measured using Bruker Avance 500 MHz spectrometer. Monomer conversion and theoretical number-average molecular weight ($M_{n,th}$) were determined by NMR based on the previous research [17]. MWs and MWDs were determined by GPC (Polymer Standards Services (PSS) columns (guard, 10^5, 10^3, and 10^2 Å), with THF eluent, flow rate 1.00 mL/min, and with a differential refractive index (RI) detector (Viscotek, T60A)). The apparent molecular weights (MWs) and dispersity (M_w/M_n) were determined with a calibration based on PS standards using TRISEC software. CVs and preparative electrolysis were recorded on a Metrohm Autolab potentiostat (AUT84337) using GPES software from EcoChemie B. V. Corporation. The electrolysis were carried out under Ar atmosphere using a Pt disk for CV, (A = 0.071 cm^2) and Pt mesh for preparative electrolysis, (A = ~6 cm^2) working electrodes (WE). The counter electrode (CE, sacrificial anode) was Al wire (l = 10 cm, d = 1 mm). Values for potentials applied for preparative electrolysis were

established from CV measurements at a 100 mV/s scan rate using saturated calomel electrode (SCE; Gamry) reference electrode (RE) according to the previous research [15].

2.3. Synthesis of β-CD-(PDMAEMA)$_{21}$ star polymers by *se*ATRP

The synthesis of β-CD-(PDMAEMA)$_{21}$ star polymers was conducted under potentiostatic and galvanostatic conditions (Figure 2).

TBAP (1.64 g, 5 mmol) was placed in an electrolysis cell maintained at 50 °C under an Ar purge. Then, 12 mL of Ar purged DMAEMA (71 mmol), DMF (8.9 mL) and 57 μL of $Cu^{II}Br_2$/2TPMA stock solution (0.05 M in DMF) were added to the reaction cell. The CV was recorded using a Pt disk WE, a SCE RE, and an Al wire CE for determining the appropriate applied potential ($E_{app} = E_{pc}$, $E_{app} = E_{pc}$–30 mV, $E_{app} = E_{pc}$–60 mV, and $E_{app} = E_{pc}$–100 mV). A solution of 451 mg of β-CD-Br$_{21}$ (0.11 mmol) in 3 mL of DMF was injected to the reaction solution and the CV was measured to confirm an increased cathodic response. Then the Pt mesh WE, Al wire CE, and SCE RE were prepared and immersed in the polymerization solution and the selected potential was applied using the preparative electrolysis method.

After the initial *se*ATRP polymerization under potentiostatic conditions the proper applied current values were calculated based on $I = Q$/s for each step. An identical reaction mixture was prepared and the polymerization was carried out under multiple applied currents ($I_{app,1}$ = (–) 0.52 mA (0.33 h), $I_{app,2}$ = (–) 0.30 mA (0.33 h), $I_{app,3}$ = (–) 0.19 mA (0.56 h), $I_{app,4}$ = (–) 0.09 mA (0.56 h), $I_{app,5}$ = (–) 0.04 mA (1.22 h)). In both cases samples were withdrawn periodically to follow the monomer conversion, using ^{1}H NMR. The M_n and M_w/M_n were determined by GPC measurements (with PS standard curve). The product was purified by dialysis against water (Spectra/Por dialysis membrane, MWCO 1000, Spectrum Laboratories Inc.), dried by air, dissolved in acetone, passed through a neutral alumina column in order to remove catalyst, and dried under vacuum for 5 days. The polymer was then isolated and characterized using ^{1}H NMR.

2.4. Chain extension of a β-CD-(PDMAEMA)$_{21}$ star macroinitiator with BA

The synthesis of β-CD-(PDMAEMA-*b*-PBA)$_{21}$ star block copolymers was conducted under potentiostatic and galvanostatic conditions (Figure 3).

The *se*ATRP method was also used for the chain extension of the β-CD-(PDMAEMA-Br)$_{21}$ macroinitiator with BA. Polymerization conditions: $[BA]_0/[\beta\text{-CD-(PDMAEMA-Br)}_{21}]_0/[Cu^{II}Br_2/2TPMA]_0$ = 32/1/0.0013, $[BA]_0$ = 2.1 M in DMF, $[Cu^{II}Br_2/2TPMA]_0$ = 0.08 mM, $[TBAP]_0$ = 0.2 M, $E_{app} = E_{pc}$–60 mV (vs. SCE), T = 50 °C, WE = Pt mesh, CE = Al wire, and RE = SCE. An identical reaction mixture was prepared and *se*ATRP was carried out under multiple applied currents ($I_{app,1}$ = (–) 0.38 mA (0.67 h), $I_{app,2}$ = (–) 0.15 mA (0.67 h), $I_{app,3}$ = (–) 0.04 mA (0.67 h), $I_{app,4}$ = (–) 0.01 mA (1.0 h)). In both cases samples were withdrawn periodically to follow the monomer conversion, using ^{1}H NMR. The M_n and M_w/M_n were determined by GPC measurements (with PS standard curve). The product was purified by dialysis against water and methanol (MWCO 1000), and

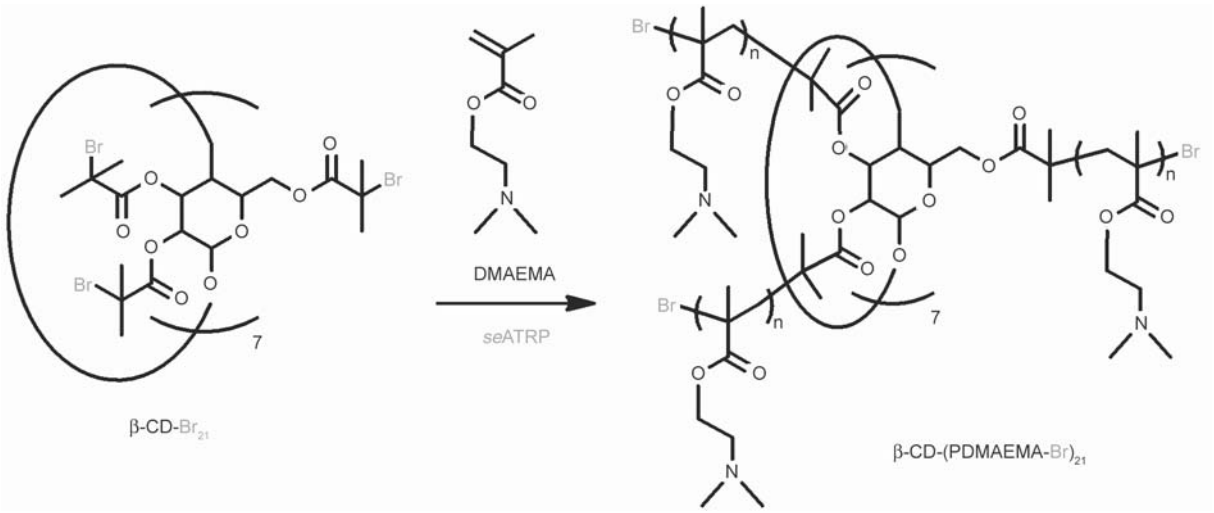

Figure 2. Synthesis of β-CD-(PDMAEMA)$_{21}$ star polymers *via se*ATRP

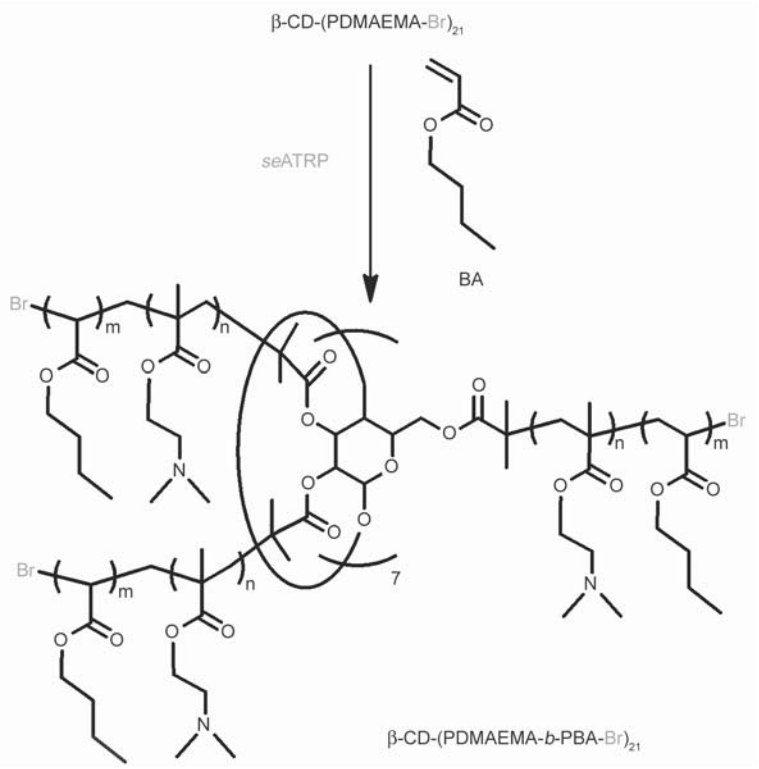

Figure 3. Synthesis of β-CD-(PDMAEMA-*b*-PBA)$_{21}$ star block copolymers *via se*ATRP

dried under vacuum for 5 days. The polymer was then isolated and characterized using ^{1}H NMR.

3. Results and discussion

Well-controlled ATRP synthesis of star polymers is challenging when chain extension occurs from a macroinitiator of lower activity to a more active monomer [24]. The rate of activation of a bromo-terminated PDMAEMA chain end is faster than the activation of a 2-bromoisobutyrate β-CD chain ends (ω-functional arms) [55, 56]. Typically, halogen exchange procedures [55–58] are employed to solve this problem, but it can't be used for systems with low concentrations of catalyst, because of poor initiation efficiency.

Here we have demonstrated new proposition of solving the problem with poor initiation efficiency by *se*ATRP procedure. In this paper synthesis of cation-

Table 1. Summary of cationic star polymers synthesis by *se*ATRP

Entry	$[M]_0/[I]_0/[Cu^{II}Br_2/2TPMA]_0$	E_{app}[(a)]	k_p^{app}[(b)] [h^{-1}]	Conv[(b)] [%]	DP_{app}[(b)] (per arm)	$M_{n,theo}$[(c)] ($\cdot 10^{-3}$)	M_n^{app}[(d)] ($\cdot 10^{-3}$)	M_w/M_n[(d)]
1	32/1/0.0013	E_{pc}	0.202	45	14	51.5	45.0	1.08
2	32/1/0.0013	E_{pc}–30 mV	0.417	70	23	78.7	67.7	1.09
3	32/1/0.0013	E_{pc}–60 mV	0.772	90	29	99.3	80.7	1.09
4	32/1/0.0013	E_{pc}–100 mV	0.947	94	30	103.9	135.0	1.63
5	32/1/0.0013	*Galvanostatic conditions*[(e)]	0.709	88	28	97.1	78.5	1.08
6	32/1/0.0013	E_{pc}–60 mV	0.577	82	26	167.7	135.6	1.15
7	32/1/0.0013	*Galvanostatic conditions*[(f)]	0.523	79	25	165.1	132.0	1.14

General reaction conditions: T = 50 °C; V_{tot} = 24 mL (except entry 6 and 7: V_{tot} = 16 mL); t = 3 h; $[M]_0$: $[DMAEMA]_0$ = 3.0 M (except entry 6 and 7: $[BA]_0$ = 2.1 M); $[I]_0$: $[\beta\text{-CD-Br}_{21}]_0$ = 4.4 mM calculated per 21 Br (except entry 6 and 7: $[\beta\text{-CD-(PDMAEMA-Br)}_{21}]_0$ = 3.1 mM calculated per 21 Br); $[Cu^{II}Br_2/2TPMA]_0$ = 0.12 mM except entry 6 and 7: = 0.08 mM); $[TBAP]_0$ = 0.2 M. *se*ATRP under potentiostatic conditions (WE = Pt mesh, CE = Al wire (l = 10 cm, d = 1 mm), RE = SCE): entries 1–4 and 6; *se*ATRP under galvanostatic conditions (WE and CE without RE): entry 5 and 7.

[a]E_{app} were selected based on CV analysis (v = 100 mV/s); [b]Monomer conversion, apparent propagation constants (k_p^{app}), and apparent practical degree of polymerization of monomer unit per arm (DP_{app}) were determined by NMR; [c]$M_{n,theo} = ([M]_0/[MI]_0) \times$ conversion $\times M_{monomer} + M_{initiator}$; [d]apparent M_n and MWD were determined by THF GPC with PS standard; [e]I_{app} = –0.52, –0.30, –0.19, –0.09, and –0.04 mA for each steps; [f]I_{app} = –0.51, –0.22, –0.11, –0.05, and –0.03 mA for each steps.

ic star copolymers by *se*ATRP are reported for the first time using only 40 ppm of Cu^{II}/L in solution. Table 1 summarizes the results of the star polymers synthesis using the β-CD based macroinitiator (M_n = 4260, M_w/M_n = 1.06) under both potentiostatic and galvanostatic conditions.

The structure of the ligand, monomer, dormant species as well as reaction conditions (solvent, temperature and pressure) can strongly influence the values of the rate constants (k_a, k_{da} and K_{ATRP} (= k_a/k_{da})) [5, 19]. In most cases electrochemically mediated ATRP reactions were carried out in DMF [14, 15, 19, 23, 24] and acetonitrile (MeCN) [20] as solvents. The polymerization in DMF was faster in comparison to the reactions conducted in MeCN, this is because more polar system could enhance ATRP equilibrium constants ($K_{ATRP} = k_a/k_{da}$) [59]. For example, K_{ATRP} value in aqueous condition is *ca*. 10^3 times higher than MeCN condition. In contrast, less polar solvent condition such as anisole mixture would require higher concentration of the supporting electrolyte to achieve better conductivity [60]. Moreover it is well known that temperature plays a vital role in controlled polymerization systems, because the activation rate constants increased with increasing temperature [61, 62]. Thus, the objective of this study was to investigate and optimize polymerization conditions for *se*ATRP of DMAEMA (in terms of R_p, controlled MWs and narrow MWDs).

3.1. Influence of different applied potential

The effect of applied potential ($E_{app} = E_{pc}$, $E_{app} = E_{pc}$–30 mV, $E_{app} = E_{pc}$–60 mV, and $E_{app} = E_{pc}$–100 mV) on the polymerization behavior was investigated as reported in Table 1, entries 1–4, and Figure 4. In essence, the fastest k_p^{app} (thereby R_p) and

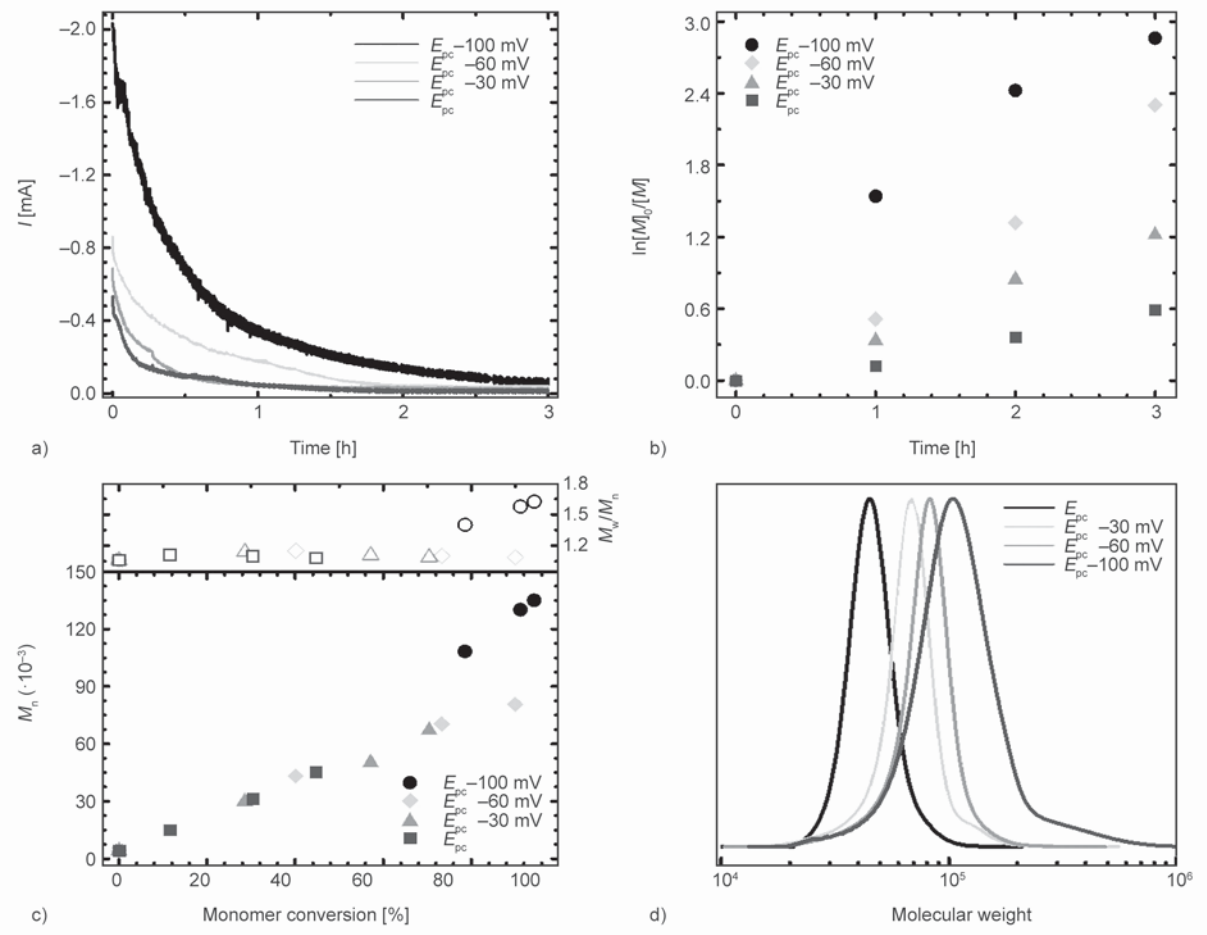

Figure 4. Synthesis of β-CD-PDMAEMA star-shaped polymers as a function of applied potential; (a) current profile versus time, (b) first-order kinetic plots, (c) M_n and M_w/M_n versus monomer conversion, and (d) GPC results of DMAEMA polymerization for different E_{app} values (final GPC traces for each reactions). Reaction conditions: $[DMAEMA]_0/[\beta\text{-CD-Br}_{21}\text{ (per –Br)}]_0/[Cu^{II}Br_2/2TPMA]_0$ = 32/1/0.0013, $[DMAEMA]_0$ = 3.0 M, $[Cu^{II}Br_2/2TPMA]_0$ = 0.12 mM, T = 50 °C, $[TBAP]_0$ = 0.2 M, V_{tot} = 24 mL, $E_{app} = E_{pc}$, $E_{app} = E_{pc}$–30 mV, $E_{app} = E_{pc}$–60 mV, $E_{app} = E_{pc}$–100 mV (vs. SCE).

larger cathodic currents (faster rate of reduction) were observed when more negative potential was applied (compare k_p^{app}; Table 1, entries 4 vs. 1–3). In this case, faster rates of reduction provide a higher [Cu^I/L] and [P•] leads to a higher R_p [19].

The polymerization results for more positive applied potentials (E_{pc}, E_{pc}–30 mV and E_{pc}–60 mV) showed a linear increase of M_n with conversion (Figure 4c), and low M_w/M_n values of obtained stars (Figure 4c–4d). On the other hand GPC trace of β-CD-PDMAEMA received at the most negative E_{app} (E_{pc}–100 mV, Figure 4d) showed the presence of a significant high molecular weight shoulder attributed to a higher occurrence of star-star intermolecular X-linking reaction *via* a coupling process as well as intramolecular coupling, which lead to less uniform growth of arms [63].

3.2. Synthesis of 21-arm star block copolymers

The preparation of CD star homopolymers with 21-arms of PDMAEMA under potentiostatic and galvanostatic conditions were carried out and the results are reported in Table 1, entries 3 and 5, Figure 5 and 6. Nearly identical first-order kinetic plots were observed (Figure 5b), with linear MW evolution (Figure 5c), and GPC analysis indicated narrow MWD (Figure 5a, 6a and 6b).

Chain end functionality was evaluated by chain extension from β-CD-$(PDMAEMA_{28})_{21}$ macroinitiator (M_n = 97 100, M_w/M_n = 1.08; Table 1, entry 5) with BA as the second monomer to form a star block copolymers under both copolymers under potentiostatic and galvanostatic conditions (Table 1, entries 6–7, Figure 7 and 8).

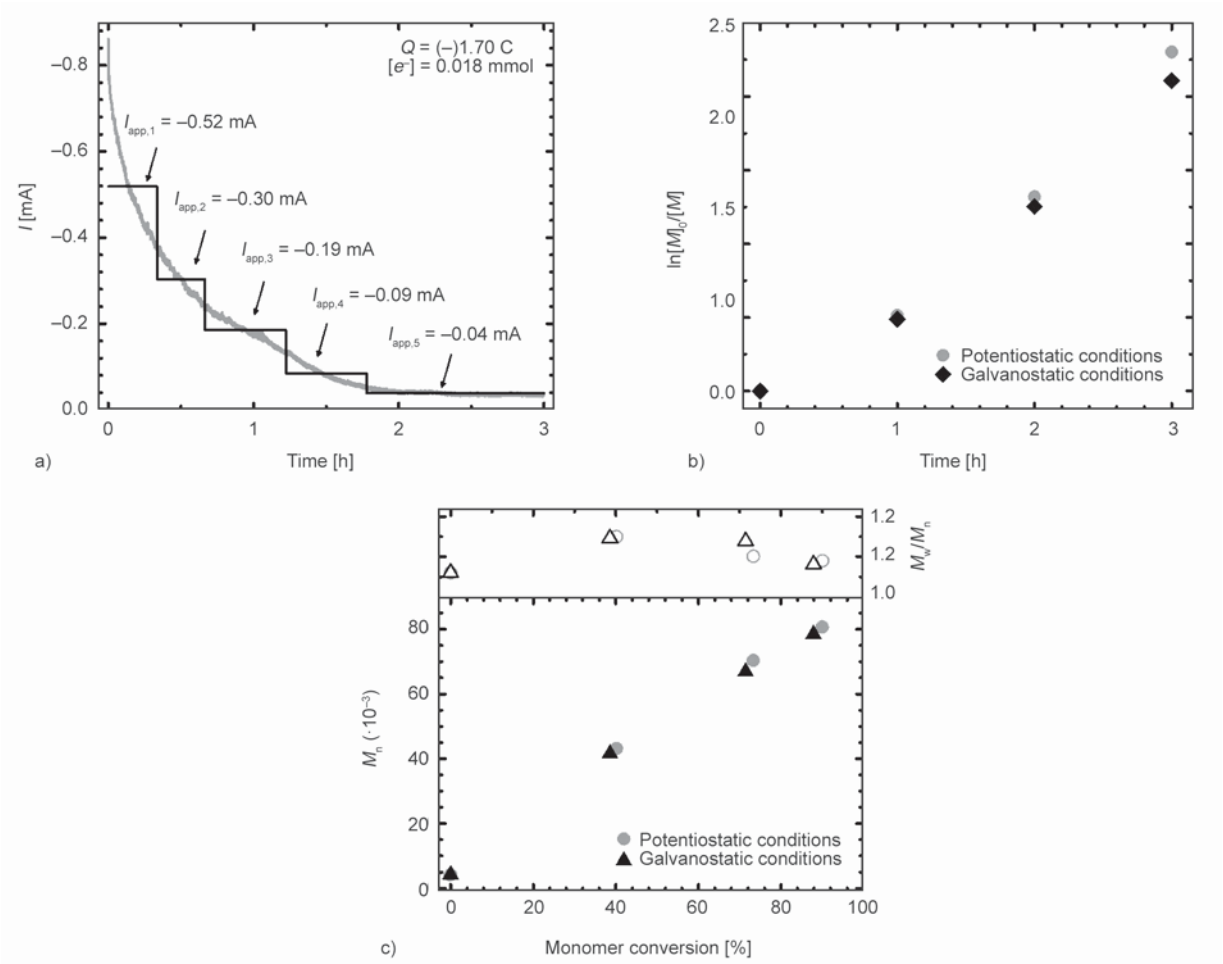

Figure 5. Multi-step preparative electrolysis for *se*ATRP; (a) preparative electrolysis results from applied potential conditions (grey line) and applied current (black line), (b) first-order kinetic plot of monomer conversion versus time, and (c) M_n and M_w/M_n versus monomer conversion by potentiostatic and galvanostatic conditions. Reaction conditions: $[DMAEMA]_0/[\beta\text{-CD-}Br_{21}$ (per –Br)$]_0/[Cu^{II}Br_2/2TPMA]_0$ = 32/1/0.0013, $[DMAEMA]_0$ = 3.0 M, $[Cu^{II}Br_2/2TPMA]_0$ = 0.12 mM, T = 50 °C, $[TBAP]_0$ = 0.2 M, V_{tot} = 24 mL.

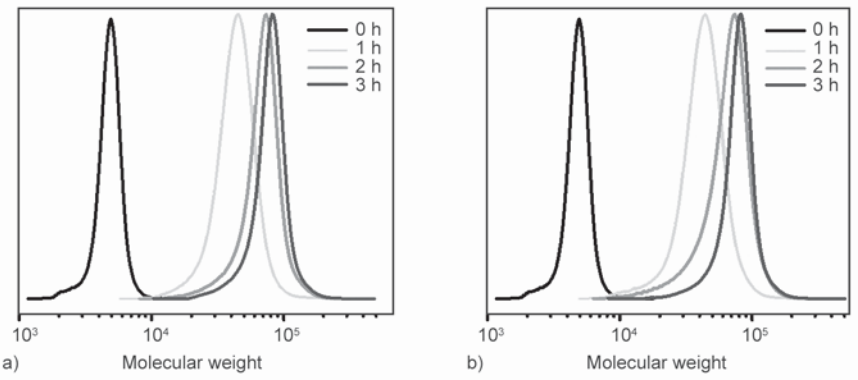

Figure 6. GPC traces of DMAEMA polymerization in the presence of β-CD-Br_{21} under potentiostatic *se*ATRP (a) and galvanostatic *se*ATRP (b)

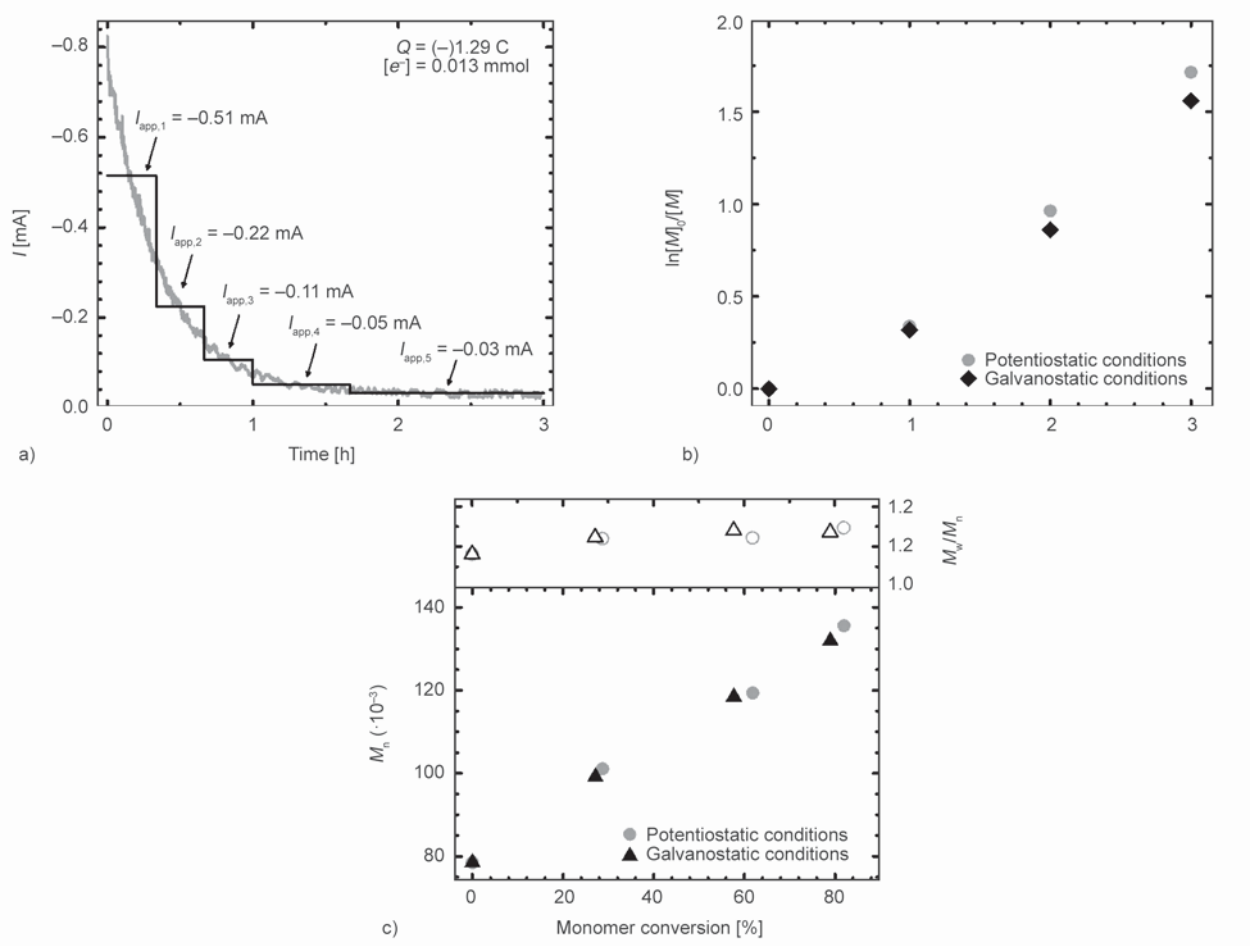

Figure 7. Multi-step preparative electrolysis for *se*ATRP; (a) preparative electrolysis results from applied potential conditions (grey line) and applied current (black line), (b) first-order kinetic plot of monomer conversion versus time, and (c) M_n and M_w/M_n versus monomer conversion by potentiostatic and galvanostatic conditions. Reaction conditions: $[BA]_0/[\beta\text{-CD-(PDMAEMA-Br)}_{21}\text{ (per –Br)}]_0/[Cu^{II}Br_2/2TPMA]_0 = 32/1/0.0013$, $[BA]_0 = 2.1$ M, $[Cu^{II}Br_2/2TPMA]_0 = 0.08$ mM, $T = 50$ °C, $[TBAP]_0 = 0.2$ M, $V_{tot} = 16$ mL.

Close to identical first-order kinetic plots were observed (Figure 7b), and DP of resulting copolymers increased linearly with monomer conversion (Figure 7c) indicating high initiation efficiency. The differences between theoretical and measured MW originate the differences in hydrodynamic radius of star and linear polymer standards for GPC. Moreover, GPC analysis indicated narrow MWD (Figure 7c and 8a–b) confirming that the halogen end groups were preserved during the *se*ATRP of BA. In this case the % of chains terminated by radical means are below 1%, what indicating that *se*ATRP was conducted

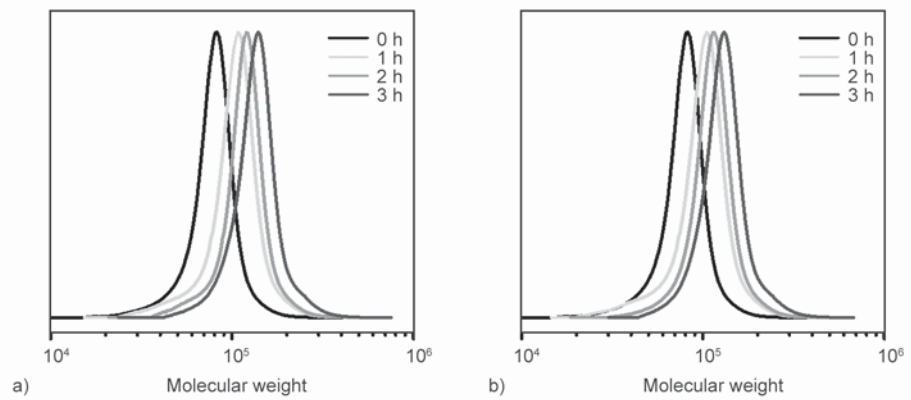

Figure 8. GPC traces of BA polymerization in the presence of β-CD-(PDMAEMA-Br)$_{21}$ under different conditions: potentiostatic *se*ATRP (a) and galvanostatic *se*ATRP (b)

with preserved chain end functionality, therefore the bimodality cannot be detected by GPC, even if termination will be 100% of coupling. Probability of the intramolecular termination of acrylates can be enhanced due to a close proximity of radicals but also can be diminished due to radical segregation [15, 64].

3.3. Chemical structure of the 21-arm star polymers

The chemical structure of the synthesized β-CD-(PDMAEMA$_{28}$)$_{21}$ star polymer (Table 1, entry 5) and β-CD-(PDMAEMA$_{28}$-PBA$_{25}$)$_{21}$ star block copolymer (Table 1, entry 7) were confirmed by ^{1}H NMR spectroscopy (Figure 9 and 10).

The ^{1}H NMR spectrum shown in Figure 9 confirms the structure of β-CD-(PDMAEMA$_{28}$)$_{21}$ star cationic polymer obtained through *se*ATRP under galvanostatic conditions (Table 1, entry 5). The chemical shifts, 0.75–1.17, 1.72–2.09, 2.20–2.50, 2.51–2.86, and 3.78–4.34 ppm, are mainly attributable to the –CH_3 (α), –CH_2– (β), –CH_3 (g), –CH_2– (f), and –OCH_2– (e) groups of the PDMAEMA units in the arms, respectively, indicating the presence of PDMAEMA chains [65]. While, in the ^{1}H NMR spectrum of the star block copolymer (Figure 10), the chemical shifts, 0.75–1.18m, 1.31–2.02, 2.18–2.55, 2.57–2.86, and 3.78–4.34 ppm, are mainly attributed by the –CH_3 (d), –CH_2– (β′+b+c), –CH– (α′), and –OCH_2– (a) groups of the PBA units in the

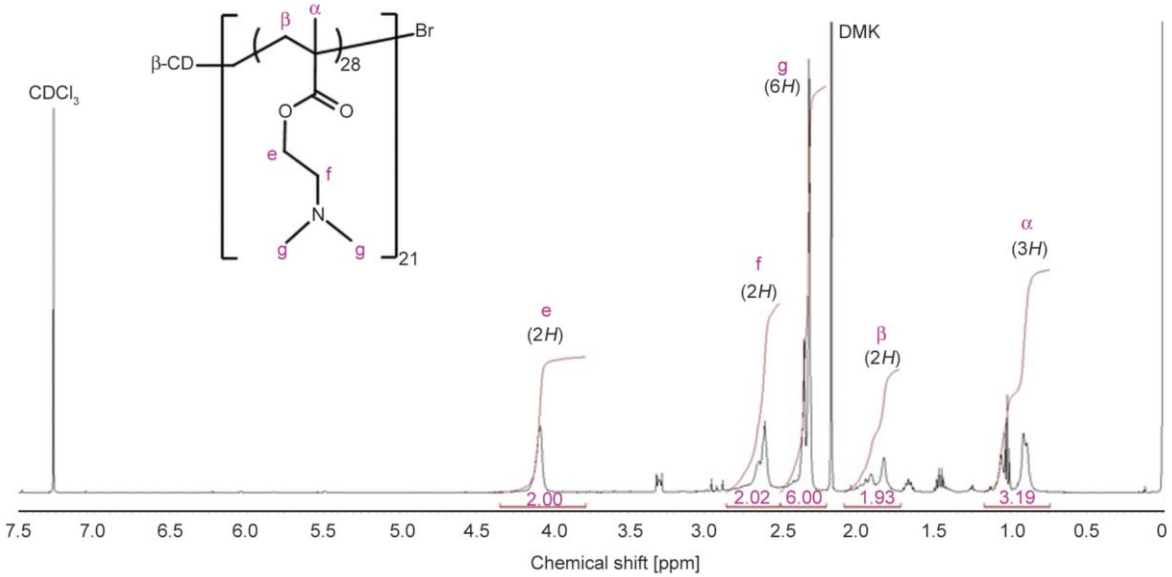

Figure 9. ^{1}H NMR spectrum of CD star homopolymers with PDMAEMA arms (β-CD-(PDMAEMA$_{28}$)$_{21}$; Table 1, entry 5; M_n = 97 100, $Đ$ = 1.08) after purification (in $CDCl_3$)

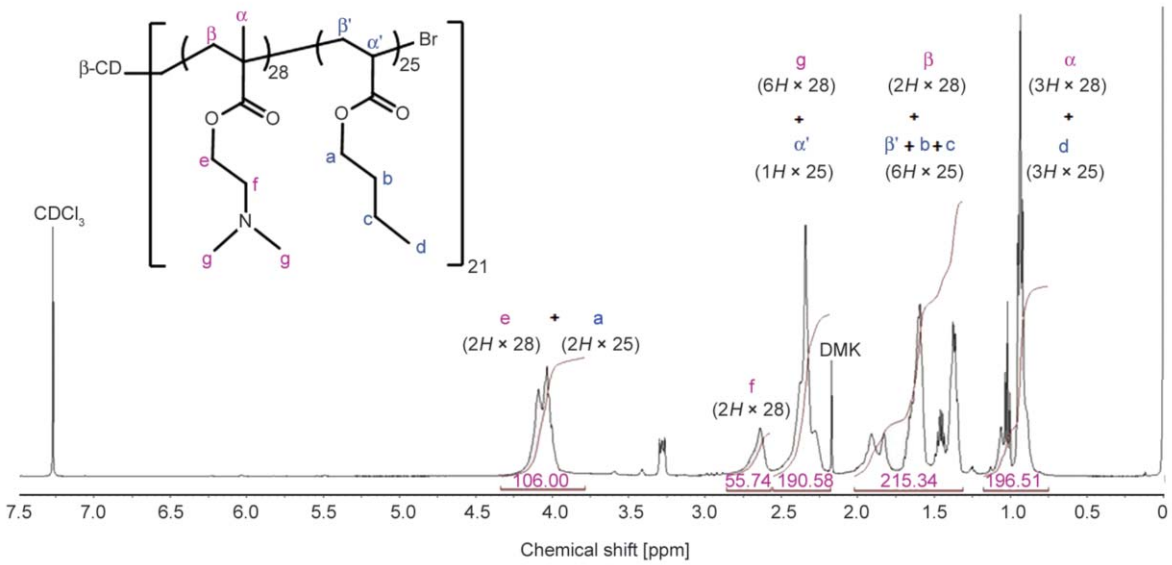

Figure 10. ^{1}H NMR spectrum of star block copolymer (β-CD-(PDMAEMA$_{28}$-PBA$_{25}$)$_{21}$; Table 1, entry 7; M_n = 165 100, $Đ$ = 1.14) after purification (in $CDCl_3$)

arms, respectively, indicating the presence of PBA chains [15].

4. Conclusions

The controlled 21-arm star polymers consisting of a β-CD core and PDMAEMA arms were successfully prepared *via* simplified electrochemically mediated atom transfer radical polymerization with low concentrations of catalyst (40 ppm of Cu^{II} species). The rate of the polymerizations was controlled by applying less negative E_{app} and therefore eliminating intermolecular termination reactions between growing arms. Chain extension of the initially formed hydrophilic star polymer with a more hydrophobic monomer (BA), confirmed the preservation of terminal halogen end group during the *se*ATRP of methacrylates. The use of a galvanostatic technique provided similar results to polymerizations conducted under potentiostatic conditions, providing polymers with molecular weight evolution close to theoretical values, while generating stars with narrow molecular weight distribution. Furthermore, the results from ^{1}H NMR spectral studies support the formation of star block (co)polymers. These new amphiphilic polyelectrolyte star copolymers are promising candidates for potential applications in biomedical fields, such as drug delivery, gene delivery, and antifouling coatings.

Acknowledgements

Financial support from U-553/DS is gratefully acknowledged. NMR spectra were recorded in the Laboratory of Spectrometry, Faculty of Chemistry, Rzeszow University of Technology and were financed from DS budget.

References

[1] Wang J-S., Matyjaszewski K.: Controlled/'living' radical polymerization. Atom transfer radical polymerization in the presence of transition-metal complexes. Journal of the American Chemical Society, **117**, 5614–5615 (1995).
DOI: 10.1021/ja00125a035

[2] Matyjaszewski K., Jo S. M., Paik H-J., Shipp D. A.: An investigation into the CuX/2,2′-bipyridine (X = Br or Cl) mediated atom transfer radical polymerization of acrylonitrile. Macromolecules, **32**, 6431–6438 (1999).
DOI: 10.1021/ma9905526

[3] Ishizu K., Satoh J., Sogabe A.: Architecture and solution properties of AB-type brush–*block*–brush amphiphilic copolymers *via* ATRP techniques. Journal of Colloid and Interface Science, **274**, 472–479 (2004).
DOI: 10.1016/j.jcis.2004.03.044

[4] Ayres N.: Atom transfer radical polymerization: A robust and versatile route for polymer synthesis. Polymer Reviews, **51**, 138–162 (2011).
DOI: 10.1080/15583724.2011.566402

[5] Matyjaszewski K.: Atom transfer radical polymerization (ATRP): Current status and future perspectives. Macromolecules, **45**, 4015–4039 (2012).
DOI: 10.1021/ma3001719

[6] He W., Jiang H., Zhang L., Cheng Z., Zhu X.: Atom transfer radical polymerization of hydrophilic monomers and its applications. Polymer Chemistry, **4**, 2919–2938 (2013).
DOI: 10.1039/C3PY00122A

[7] Ran J., Wu L., Zhang Z., Xu T.: Atom transfer radical polymerization (ATRP): A versatile and forceful tool for functional membranes. Progress in Polymer Science, **39**, 124–144 (2014).
DOI: 10.1016/j.progpolymsci.2013.09.001

[8] Pangilinan K., Advincula R.: Cyclic polymers and catenanes by atom transfer radical polymerization (ATRP). Polymer International, **63**, 803–813 (2014).
DOI: 10.1002/pi.4717

[9] Joubert F., Musa O. M., Hodgson D. R. W., Cameron N. R.: The preparation of graft copolymers of cellulose and cellulose derivatives using ATRP under homogeneous reaction conditions. Chemical Society Reviews, **43**, 7217–7235 (2014).
DOI: 10.1039/C4CS00053F

[10] Hadasha W., Klumperman B.: Atom transfer radical polymerization as a powerful tool in the synthesis of molecular brushes. Polymer International, **63**, 824–834 (2014).
DOI: 10.1002/pi.4697

[11] Król P., Chmielarz P.: Recent advances in ATRP methods in relation to the synthesis of copolymer coating materials. Progress in Organic Coatings, **77**, 913–948 (2014).
DOI: 10.1016/j.porgcoat.2014.01.027

[12] Ding M., Jiang X., Zhang L., Cheng Z., Zhu X.: Recent progress on transition metal catalyst separation and recycling in ATRP. Macromolecular Rapid Communications, **36**, 1702–1721 (2015).
DOI: 10.1002/marc.201500085

[13] Rwei S-P., Shu K-T., Way T-F., Chang S-M., Chiang W-Y., Pan W-C.: Synthesis and characterization of hyperbranched copolymers hyper-*g*-(NIPAAm-*co*-IAM) *via* ATRP. Colloid and Polymer Science, **294**, 291–301 (2015).
DOI: 10.1007/s00396-015-3775-5

[14] Park S., Chmielarz P., Gennaro A., Matyjaszewski K.: Simplified electrochemically mediated atom transfer radical polymerization using a sacrificial anode. Angewandte Chemie International Edition, **54**, 2388–2392 (2015).
DOI: 10.1002/anie.201410598

[15] Chmielarz P., Park S., Sobkowiak A., Matyjaszewski K.: Synthesis of β-cyclodextrin-based star polymers *via* a simplified electrochemically mediated ATRP. Polymer, **88**, 36–42 (2016).
DOI: 10.1016/j.polymer.2016.02.021

[16] Bortolamei N., Isse A. A., Magenau A. J. D., Gennaro A., Matyjaszewski K.: Controlled aqueous atom transfer radical polymerization with electrochemical generation of the active catalyst. Angewandte Chemie International Edition, **50**, 11391–11394 (2011).
DOI: 10.1002/anie.201105317

[17] Chmielarz P., Park S., Simakova A., Matyjaszewski K.: Electrochemically mediated ATRP of acrylamides in water. Polymer, **60**, 302–307 (2015).
DOI: 10.1016/j.polymer.2015.01.051

[18] Chmielarz P., Krys P., Park S., Matyjaszewski K.: PEO-*b*-PNIPAM copolymers *via* SARA ATRP and eATRP in aqueous media. Polymer, **71**, 143–147 (2015).
DOI: 10.1016/j.polymer.2015.06.042

[19] Magenau A. J. D., Bortolamei N., Frick E., Park S., Gennaro A., Matyjaszewski K.: Investigation of electrochemically mediated atom transfer radical polymerization. Macromolecules, **46**, 4346–4353 (2013). DOI: 10.1021/ma400869e

[20] Magenau A. J. D., Strandwitz N. C., Gennaro A., Matyjaszewski K.: Electrochemically mediated atom transfer radical polymerization. Science, **332**, 81–84 (2011).
DOI: 10.1126/science.1202357

[21] Li B., Yu B., Huck W. T. S., Zhou F., Liu W.: Electrochemically induced surface-initiated atom-transfer radical polymerization. Angewandte Chemie International Edition, **124**, 5182–5185 (2012).
DOI: 10.1002/anie.201201533

[22] Li B., Yu B., Huck W. T. S., Liu W., Zhou F.: Electrochemically mediated atom transfer radical polymerization on nonconducting substrates: Controlled brush growth through catalyst diffusion. Journal of the American Chemical Society, **135**, 1708–1710 (2013). DOI: 10.1021/ja3116197

[23] Park S., Cho H. Y., Wegner K. B., Burdynska J., Magenau A. J. D., Paik H-J., Jurga S., Matyjaszewski K.: Star synthesis using macroinitiators *via* electrochemically mediated atom transfer radical polymerization. Macromolecules, **46**, 5856–5860 (2013).
DOI: 10.1021/ma401308e

[24] Chmielarz P., Sobkowiak A., Matyjaszewski K.: A simplified electrochemically mediated ATRP synthesis of PEO-*b*-PMMA copolymers. Polymer, **77**, 266–271 (2015).
DOI: 10.1016/j.polymer.2015.09.038

[25] Shida N., Koizumi Y., Nishiyama H., Tomita I., Inagi S.: Electrochemically mediated atom transfer radical polymerization from a substrate surface manipulated by bipolar electrolysis: Fabrication of gradient and patterned polymer brushes. Angewandte Chemie International Edition, **54**, 3922–3926 (2015).
DOI: 10.1002/ange.201412391

[26] Guo J-K., Zhou Y-N., Luo Z-H.: Kinetic insight into electrochemically mediated ATRP gained through modeling. AIChE Journal, **61**, 4347–4357 (2015).
DOI: 10.1002/aic.14969

[27] Hosseiny S. S., van Rijn P.: Surface initiated polymerizations *via e*-ATRP in pure water. Polymers, **5**, 1229–1240 (2013).
DOI: 10.3390/polym5041229

[28] Fantin M., Isse A. A., Gennaro A., Matyjaszewski K.: Understanding the fundamentals of aqueous ATRP and defining conditions for better control. Macromolecules, **48**, 6862–6875 (2015).
DOI: 10.1021/acs.macromol.5b01454

[29] Sun Y., Du H., Deng Y., Lan Y., Feng C.: Preparation of polyacrylamide *via* surface-initiated electrochemical-mediated atom transfer radical polymerization (SI-eATRP) for Pb^{2+} sensing. Journal of Solid State Electrochemistry, **20**, 105–113 (2016).
DOI: 10.1007/s10008-015-3008-3

[30] Strover L. T., Malmström J., Stubbing L. A., Brimble M. A., Travas-Sejdic J.: Electrochemically-controlled grafting of hydrophilic brushes from conducting polymer substrates. Electrochimica Acta, **188**, 57–70 (2016).
DOI: 10.1016/j.electacta.2015.11.106

[31] Sun Y., Du H., Lan Y., Wang W., Liang Y., Feng C., Yang M.: Preparation of hemoglobin (Hb) imprinted polymer by Hb catalyzed eATRP and its application in biosensor. Biosensors and Bioelectronics, **77**, 894–900 (2016).
DOI: 10.1016/j.bios.2015.10.067

[32] Li J., Xiao H., Kim Y. S., Lowe T. L.: Synthesis of water-soluble cationic polymers with star-like structure based on cyclodextrin core *via* ATRP. Journal of Polymer Science Part A: Polymer Chemistry, **43**, 6345–6354 (2005).
DOI: 10.1002/pola.21058

[33] Georgiou T. K., Vamvakaki M., Phylactou L. A., Patrickios C. S.: Synthesis, characterization, and evaluation as transfection reagents of double-hydrophilic star copolymers: Effect of star architecture. Biomacromolecules, **6**, 2990–2997 (2005).
DOI: 10.1021/bm050307w

[34] Xu F. J., Zhang Z. X., Ping Y., Li J., Kang E. T., Neoh K. G.: Star-shaped cationic polymers by atom transfer radical polymerization from β-cyclodextrin cores for nonviral gene delivery. Biomacromolecules, **10**, 285–293 (2009).
DOI: 10.1021/bm8010165

[35] Li J., Guo Z., Xin J., Zhao G., Xiao H.: 21-arm star polymers with different cationic groups based on cyclodextrin core for DNA delivery. Carbohydrate Polymers, **79**, 277–283 (2010).
DOI: 10.1016/j.carbpol.2009.08.006

[36] Wu Y., Ni P., Zhang M., Zhu X.: Fabrication of microgels *via* supramolecular assembly of cyclodextrin-containing star polycations and oppositely charged linear polyanions. Soft Matter, **6**, 3751–3758 (2010).
DOI: 10.1039/C000979B

[37] Xiu K. M., Yang J. J., Zhao N. N., Li J. S., Xu F. J.: Multiarm cationic star polymers by atom transfer radical polymerization from β-cyclodextrin cores: Influence of arm number and length on gene delivery. Acta Biomaterialia, **9**, 4726–4733 (2013).
DOI: 10.1016/j.actbio.2012.08.020

[38] Durmaz Y. Y., Lin Y-L., ElSayed M. E. H.: Development of degradable, pH-sensitive star vectors for enhancing the cytoplasmic delivery of nucleic acids. Advanced Functional Materials, **23**, 3885–3895 (2013).
DOI: 10.1002/adfm.201203762

[39] Li S., Xiao M., Zheng A., Xiao H.: Synthesis and characterization of a novel water-soluble cationic diblock copolymer with star conformation by ATRP. Materials Science and Engineering: C, **43**, 350–358 (2014).
DOI: 10.1016/j.msec.2014.06.031

[40] Wang L., Yang Y-W., Zhu M., Qiu G., Wu G., Gao H.: β-cyclodextrin-conjugated amino poly(glycerol methacrylate)s for efficient insulin delivery. RSC Advances, **4**, 6478–6485 (2014).
DOI: 10.1039/C3RA47150K

[41] Pan Y., Xue Y., Snow J., Xiao H.: Tailor-made antimicrobial/antiviral star polymer *via* ATRP of cyclodextrin and guanidine-based macromonomer. Macromolecular Chemistry and Physics, **216**, 511–518 (2015).
DOI: 10.1002/macp.201400525

[42] Zhang M., Shen W., Xiong Q., Wang H., Zhou Z., Chen W., Zhang Q.: Thermo-responsiveness and biocompatibility of star-shaped poly[2-(dimethylamino)ethyl methacrylate]-*b*-poly(sulfobetaine methacrylate) grafted on a β-cyclodextrin core e. RSC Advances, **5**, 28133–28140 (2015).
DOI: 10.1039/C5RA02115D

[43] Loh X. J., Wu Y-L.: Cationic star copolymers based on β-cyclodextrins for efficient gene delivery to mouse embryonic stem cell colonies. Chemical Communications, **51**, 10815–10818 (2015).
DOI: 10.1039/C5CC03686K

[44] Jiang X., Wu J., Zhang L., Cheng Z., Zhu X.: A facile strategy for catalyst separation and recycling suitable for ATRP of hydrophilic monomers using a macroligand. Macromolecular Rapid Communications, **37**, 143–148 (2016).
DOI: 10.1002/marc.201500439

[45] Plamper F. A., Ruppel M., Schmalz A., Borisov O., Ballauff M., Müller A. H. E.: Tuning the thermoresponsive properties of weak polyelectrolytes: Aqueous solutions of star-shaped and linear poly(*N,N*-dimethylaminoethyl methacrylate). Macromolecules, **40**, 8361–8366 (2007).
DOI: 10.1021/ma071203b

[46] Yancheva E., Paneva D., Maximova V., Mespouille L., Dubois P., Manolova N., Rashkov I.: Polyelectrolyte complexes between (cross-linked) *N*-carboxyethylchitosan and (quaternized) poly[2-(dimethylamino)ethyl methacrylate]: Preparation, characterization, and antibacterial properties. Biomacromolecules, **8**, 976–984 (2007).
DOI: 10.1021/bm061029j

[47] Plamper F. A., McKee J. R., Laukkanen A., Nykänen A., Walther A., Ruokolainen J., Aseyev V., Tenhun H.: Miktoarm stars of poly(ethylene oxide) and poly(dimethylaminoethyl methacrylate): Manipulation of micellization by temperature and light. Soft Matter, **5**, 1812–1821 (2009).
DOI: 10.1039/B822143J

[48] Rezaei S. J. T., Nabid M. R., Niknejad H., Entezami A. A.: Folate-decorated thermoresponsive micelles based on star-shaped amphiphilic block copolymers for efficient intracellular release of anticancer drugs. International Journal of Pharmaceutics, **437**, 70–79 (2012). DOI: 10.1016/j.ijpharm.2012.07.069

[49] Loh X. J.: Poly(DMAEMA-*co*-PPGMA): Dual-responsive 'reversible' micelles. Journal of Applied Polymer Science, **127**, 992–1000 (2013). DOI: 10.1002/app.37530

[50] Loh X. J., Ong S. J., Tung Y. T., Choo H. T.: *Co*-delivery of drug and DNA from cationic dual-responsive micelles derived from poly(DMAEMA-*co*-PPGMA). Materials Science and Engineering: C, **33**, 4545–4550 (2013). DOI: 10.1016/j.msec.2013.07.011

[51] Matyjaszewski K., Nakagawa Y., Jasieczek C. B.: Polymerization of *n*-butyl acrylate by atom transfer radical polymerization. Remarkable effect of ethylene carbonate and other solvents. Macromolecules, **31**, 1535–1541 (1998). DOI: 10.1021/ma971444r

[52] Zhang H., van der Linde R.: Atom transfer radical polymerization of *n*-butyl acrylate catalyzed by CuBr/*N*-(*n*-hexyl)-2-pyridylmethanimine. Journal of Polymer Science Part A: Polymer Chemistry, **40**, 3549–3561 (2002). DOI: 10.1002/pola.10460

[53] Xia J., Matyjaszewski K.: Controlled/'living' radical polymerization. Atom transfer radical polymerization catalyzed by copper(I) and picolylamine complexes. Macromolecules, **32**, 2434–2437 (1999). DOI: 10.1021/ma981694n

[54] Li J., Xiao H.: An efficient synthetic-route to prepare [2,3,6-tri-*O*-(2-bromo-2-methylpropionyl]-β-cyclodextrin). Tetrahedron Letters, **46**, 2227–2229 (2005). DOI: 10.1016/j.tetlet.2005.02.027

[55] Matyjaszewski K., Shipp D. A., Wang J-L., Grimaud T., Patten T. E.: Utilizing halide exchange to improve control of atom transfer radical polymerization. Macromolecules, **31**, 6836–6840 (1998). DOI: 10.1021/ma980476r

[56] Peng C-H., Kong J., Seeliger F., Matyjaszewski K.: Mechanism of halogen exchange in ATRP. Macromolecules, **44**, 7546–7557 (2011). DOI: 10.1021/ma201035u

[57] Shipp D. A., Wang J-L., Matyjaszewski K.: Synthesis of acrylate and methacrylate block copolymers using atom transfer radical polymerization. Macromolecules, **31**, 8005–8008 (1988). DOI: 10.1021/ma981033q

[58] Dufour B., Koynov K., Pakula T., Matyjaszewski K.: PBA–PMMA 3-arm star block copolymer thermoplastic elastomers. Macromolecular Chemistry and Physics, **209**, 1686–1693 (2008). DOI: 10.1002/macp.200800151

[59] Matyjaszewski K., Tsarevsky N. V.: Macromolecular engineering by atom transfer radical polymerization. Journal of the American Chemical Society, **136**, 6513–6533 (2014). DOI: 10.1021/ja408069v

[60] Matyjaszewski K., Bortolamei N., Magenau A., Gennaro A., Isse A. A.: Electrochemically mediated atom transfer radical polymerization. U.S. Patent 20140183055 A1, USA (2014).

[61] Tang W., Nanda A. K., Matyjaszewski K.: Effect of [pyridylmethanimine]/[Cu^{I}] ratio, ligand, solvent and temperature on the activation rate constants in atom transfer radical polymerization. Macromolecular Chemistry and Physics, **206**, 1171–1177 (2005). DOI: 10.1002/macp.200500058

[62] Seeliger F., Matyjaszewski K.: Temperature effect on activation rate constants in ATRP: New mechanistic insights into the activation process. Macromolecules, **42**, 6050–6055 (2009). DOI: 10.1021/ma9010507

[63] Cheng G., Böker A., Zhang M., Krausch G., Müller A. H. E.: Amphiphilic cylindrical core–shell brushes *via* a 'grafting from' process using ATRP. Macromolecules, **34**, 6883–6888 (2001). DOI: 10.1021/ma0013962

[64] Nakamura Y., Lee R., Coote M. L., Yamago S.: Termination mechanism of the radical polymerization of acrylates. Macromolecular Rapid Communications, **37**, 506–513 (2016). DOI: 10.1002/marc.201500677

[65] Sevimli S., Sagnella S., Kavallaris M., Bulmus V., Davis T. P.: Synthesis, self-assembly and stimuli responsive properties of cholesterol conjugated polymers. Polymer Chemistry, **3**, 2057–2069 (2012). DOI: 10.1039/C2PY20112G

eXPRESS Polymer Letters Vol.10, No.10 (2016) 822–834
Available online at www.expresspolymlett.com
DOI: 10.3144/expresspolymlett.2016.77

Temperature-dependent rigidity and magnetism of polyamide 6 nanocomposites based on nanocrystalline Fe-Ni alloy of various geometries

M. A. A. Mohamed[1*], *D. Pedrazzoli*[2], *N. Nady*[3], *K. Kalaitzidou*[2,4]

[1]Fabrication Technology Department, Advanced Technology and New Materials Research Institute, City of Scientific Research and Technological Applications (SRTA City), New Borg El-Arab, 21934 Alexandria, Egypt
[2]The George W. Woodruff School of Mechanical Engineering, Georgia Institute of Technology (Georgia Tech), Atlanta, GA 30332-0405, USA
[3]Polymer Department, Advanced Technology and New Materials Research Institute, City of Scientific Research and Technological Applications (SRTA City), New Borg El-Arab, 21934 Alexandria, Egypt
[4]School of Materials Science and Engineering, Georgia Institute of Technology (Georgia Tech), Atlanta, GA 30332-0405, USA

Received 21 March 2016; accepted in revised form 22 May 2016

Abstract. The focus of this study is to explore the potential use of Polyamide 6 nanocomposite reinforced with nanocrystalline (nc) $Fe_{20}Ni_{80}$ alloy ($Fe_{20}Ni_{80}$/PA6 PNC) in electromagnetic applications and provide understanding of how the alloy particle geometry is controlling the nanocomposite's physical properties. Thermomechanical rigidity, room-temperature soft magnetic performance and thermal soft magnetic stability of $Fe_{20}Ni_{80}$/PA6 PNCs based on spherical-sea urchin alloy particles (UMB2-SU) and necklace-like alloy chains (UMB2-NC) have been investigated. Both PNCs have considerably superior bulk properties compared to neat PA6 and UMB2-SU exhibits the most remarkable overall performance. Morphological observations disclose two relevant phenomena: i) improved dispersion and distribution of the SU alloy particles than the NC ones within PA6 matrix, leading to stronger filler-matrix interfacial interactions within the UMB2-SU as compared to the UMB2-NC and ii) presence of constraint polymer regions in between alloy segments within the UMB2-SU that provide secondary reinforcing and soft magnetic mechanisms. Such phenomena along with the lower alloy crystallite size and PA6 γ-crystal type content within the UMB2-SU than in the UMB2-NC, are considered the main responsible factors for the distinctive performance of UMB2-SU. Overall, compared to various ferromagnetic nanocrystalline metallic materials, the research proposes the SU nc $Fe_{20}Ni_{80}$ alloy as a valuable nanofiller in polymers for electromagnetic applications.

Keywords: *polymer composites, nanomaterials, reinforcements, thermal properties, industrial applications*

1. Introduction

Magnetic nanomaterials are essential components of modern technology in a wide range of applications, including catalysis [1], sensors [2], data storage [3], biotechnology/biomedicine [4], magnetic resonance imaging [5], environmental remediation [6], spintronic [7] and microwave devices [8, 9]. Nanoscale magnetic materials are so attractive because they show remarkable novel phenomena compared to their bulk counterparts, such as superparamagnetism, ultrahigh magnetic anisotropy and coercive force, and giant magnetoresistance. These phenomena arise from finite size and surface effects that dominate the magnetic behavior of individual nanoparticles [10, 11]. Among magnetic nanomaterials, ferromagnetic nanosized metals, metal alloys and metal oxides are the

*Corresponding author, e-mail: mmohamed@mucsat.sci.eg

most exploited ones due to their distinctive magnetic properties [12, 13]. However, drawbacks of such materials, including corrosion, high density (weight), and physical rigidity, make alternatives desirable in many technological areas. Incorporation of ferromagnetic metallic nanomaterials into polymer matrices is regarded as a good strategy to overcome their shortcomings. Polymer nanocomposites doped with ferromagnetic metallic nanomaterials (FMNMs-PNCs) retain the key features of polymers such as lightweight, exceptional processability, flexibility and corrosion resistance. Meanwhile, they display new functionalities such as magnetism and electrical conductivity as well as enhanced mechanical and thermal properties as compared to the neat polymer due to metallic inclusions. Therefore, FMNMs-PNCs can emerge as promising alternatives to ferromagnetic metallic nanomaterials in various disciplines [14, 15]. It is well known that, intensive filler-matrix interfacial interactions should dominate the PNC structure, in order to attain a unique combination of constituents' properties. Accordingly, this has become a focal point of significant interest in the design and development of PNCs, by controlling the size, geometry, orientation, dispersion and distribution of nano-sized fillers within polymer matrix and bonding at the filler-matrix interface [15, 16].

Nanocrystalline (nc) Fe-Ni alloy is among the most attractive ferromagnetic metallic nanomaterials for electro-magnetic applications including magnetic-field sensors, read-write heads in magnetic data storage devices, magnetic actuators and motors, electromagnetic shielding and transformers magnetic cores [17]. The attention to this alloy is attributed to its unique soft magnetic properties, excellent mechanical stiffness, strength and thermal dimensional stability (rigidity) and good electrical properties [17–19]. In particular, nc $Fe_{20}Ni_{80}$ alloy is known of permalloy anomaly [17, 20]. The potential of using nc Fe-Ni alloy, as a nano-filler in polymers has been explored for the first time by the authors [21]. In that study, the room-temperature mechanical properties of nc Fe-Ni alloy/Polyamide 6 nanocomposites (Fe-Ni/PA6 PNCs) were determined as a function of the compounding technique and nano-filler content. It was concluded that the mechanical stiffness and strength of PA6 were significantly enhanced for low content of nc Fe-Ni alloy (up to 3 wt%) when the Fe-Ni/PA6 PNCs were prepared by ultrasound-assisted master batch (UMB) technique, indicating the great promise of nc Fe-Ni alloy as a nano-reinforcement to polymers.

In electro-magnetic applications, components are exposed to thermal stresses, thus requiring the material to have good thermal stability in terms of rigidity, magnetism and electrical properties [17]. Accordingly, this study focuses on the investigation of the rigidity and magnetic properties of Fe-Ni/PA6 PNC as function of temperature, in order to explore the potential use of such nanocomposite in electromagnetic applications. The alteration of the nanocomposite microstructure and subsequently thermal stability in terms of rigidity and magnetism due to different alloy geometries, was the focal point of interest throughout the research. 2 wt% Fe-Ni/PA6 PNCs based on nc $Fe_{20}Ni_{80}$ alloy with two different particle geometries; spherical-sea urchin particles and necklace-like chains, were prepared by compounding via the UMB process followed by injection molding. The morphology, crystalline structure, softening temperature and temperature-dependent coefficient of thermal expansion and magnetic properties of the nanocomposites were investigated.

2. Experimental

2.1. Materials

The polymer used is PA6 pellets (Tecomid® NB40 NL E). It was obtained in a sealed package from Eurotec® Engineering Plastics, Tekirdag, Turkey. Formic acid (HCO_2H, 98%) and ethanol (C_2H_5OH, 96%) used as a solvent and a precipitant for PA6, respectively, were obtained from Chem-Lab NV, Zedelgem, Belgium and VWR, Pennsylvania, USA, respectively.

2.2. Preparation of $Fe_{20}Ni_{80}$/PA6 PNCs

nc $Fe_{20}Ni_{80}$ fine particles with two different geometries; spherical-sea urchin particles (SU) and necklace-like chains (NC), were chemically synthesized. Crystal sizes are 16 and 20 nm for the alloy particles with SU and NC geometries, respectively. Detailed information on the synthesis process as well as on the morphology, nanocrystalline structure and magnetic properties of the alloys with the two geometries can be found in Mohamed's prior study [22]. The 2 wt% $Fe_{20}Ni_{80}$/PA6 PNCs samples were made in a two-step process: i) SU and NC nc $Fe_{20}Ni_{80}$ particles were separately compounded with PA6 pellets and ii) the com-

pounded material was injection molded into standard Izod bars (ASTM-D256).

The typical compounding process is as follows. nc $Fe_{20}Ni_{80}$ particles were compounded with half of the PA6 amount via ultrasound-assisted solution mixing (USM) to prepare concentrated USM composite powder containing 4 wt% nc $Fe_{20}Ni_{80}$. The USM PNCs were then compounded (diluted) with the rest of PA6 pellets via melt mixing to prepare UMB PNCs with 2 wt% nc $Fe_{20}Ni_{80}$. Specifically, a 15 wt% PA6-formic acid solution was prepared. Then, nc $Fe_{20}Ni_{80}$ particles were dispersed and sonicated into a second very dilute 1 wt% PA6-formic acid solution for 30 min, using ultrasonic bath. The alloy particles/PA6 ratio was 1:1 wt/wt. The particles suspension was then added to the 15 wt% PA6-formic acid solution, so that the concentration of polymer in the mixture was 10 wt% and the mixture was vigorously stirred for 1 h. Addition of ethanol, with the volumetric ethanol/formic acid ratio being 2:1, initiated the precipitation of PA6 after 30 min and led to formation of the composite powder which was completed within 30 minutes. The composite powder was separated from mixed solvent through filtration and dried in vacuum oven at 80 °C for 48 h.

A DSM Micro 15 cc extruder (vertical, co-rotating twin-screw micro extruder) and 10 cc injection molding machine (Xplore Instruments, Geleen, The Netherlands) were then used for compounding the USM PNCs with the rest of PA6 pellets and fabrication of the UMB PNCs, respectively. The conditions used were: 240 °C as T_{barrel} in the compounder and injection molding machine, screw speed of 150 rpm, residence time of 4 min, T_{mold} of 70 °C and injection pressure of 0.8 MPa. Before compounding, the PA6 pellets were dried in a vacuum oven at 80 °C for 48 h. After molding, the specimens were sealed and placed in a desiccator for a minimum of 24 h prior to testing. The detailed codes of PNCs' samples are listed in Table 1.

Table 1. Nanocomposite samples' codes

Sample	Code
Control PA6	UMB0
2 wt% spherical-sea urchine $Fe_{20}Ni_{80}$/PA6 PNC	UMB2-SU
2 wt% necklace-like chains $Fe_{20}Ni_{80}$/PA6 PNC	UMB2-NC

2.3. Characterizations

Thermomechanical (TMA) analysis measurements were performed, using a Shimadzu TMA-60H thermomechanical analyzer (Shimadzu Corporation, Tokyo, Japan). Compression and penetration testing modes were employed to determine the coefficient of thermal expansion (CTE, ASTM-D696) and softening temperature, respectively, for neat PA6, UMB2-SU and UMB2-NC PNCs. Samples with dimensions of 5×5×3 mm were cut from the standard Izod bars and heated at a rate of 5 °C/min to 180 °C. Constant loads of 0.05 and 0.3 N were applied during the TMA analysis, when compression and penetration testing modes have been respectively employed. The reported results reflect an average of three measurements.

The magnetic properties of neat PA6, UMB2-SU and UMB2-NC PNCs were measured at room-temperature using a vibrating sample magnetometer (7410-S VSM, Lake Shore Cryotronics Inc, Ohio, USA), with an applied field –25 kG≤H≤25 kG. The magnetic properties of the composite sample with the best room-temperature soft magnetic performance were also characterized as a function of temperature up to 150 °C. For magnetization measurements, thin sheets with dimensions of 10 mm×5 mm×0.5 mm were cut from the central region of the Izod bars and tested along their longitudinal direction.

Morphology of the composites was investigated by scanning electron microscopy (SEM) of the impact fracture surfaces, using a JEOL JSM 6360 LV SEM (JEOL Ltd., Tokyo, Japan) operating at accelerating voltage of 20 kV. The samples were gold coated to avoid charging.

Melting and crystallization behaviors of neat PA6 and PA6 phase in the PNCs were studied using modulated differential scanning calorimeter (MDSC Q200, TA instruments, Delaware, USA). The degree of crystallinity, melting and crystallization temperatures were determined. Slices had a net weight of about 8 mg were cut from the standard Izod bars. The sliced samples were heated from ambient temperature to 270 °C, held at this temperature for 3 min to erase the thermal history and then cooled to 25 °C. All MDSC runs were conducted under nitrogen atmosphere with heating/cooling rates of 5 °C/min. The degree of crystallinity, X_C, was calculated from

the enthalpy evolved during melting based on the heating scans, using Equation (1):

$$X_C = \frac{\Delta H_m}{(1-\Phi)\Delta H_m^0} \cdot 100 \quad (1)$$

where ΔH_m is the apparent heat of fusion of the sample, ΔH_m^0 is the heat of fusion of the 100% crystalline pure PA6, which is 190 J/g, and Φ is weight fraction of nc $Fe_{20}Ni_{80}$ in the PNCs [23, 24].

X-ray diffraction (XRD) was employed to determine the relative fraction of α and γ crystalline phases in neat PA6 and PA6 phase within the PNCs. This is important in interpreting the thermomechanical performance of Nylon compounds, because α-phase is much stronger and less ductile than the γ-phase [25, 26]. The average crystallite sizes of nc $Fe_{20}Ni_{80}$ alloys within the UMB2-SU and UMB2-NC PNCs were also determined, in order to understand the influence of thermal processing on the alloy nanocrystalline structure. XRD patterns were obtained using X'Pert PRO Alfa-1 diffractometer (PANalytical, Almelo, The Netherlands) in reflection mode (45 kV, 40 mA; Cu Kα + Ni-filtered radiation, λ = 0.154 nm). The analysis was performed on the Izod specimens, at ambient temperature with a 2θ range between 8 and 80°, at a scanning rate of about 4°/min and a scanning step of 0.016°. Diffraction peaks assigned to PA6 were de-convolved to peaks corresponding to amorphous phase and crystalline phase, which is composed of α and γ crystal forms, using xPert Pro software. The percentage of γ-phase with respect to the total crystalline PA6 phase was calculated by Equation (2):

$$\gamma\,[\%] = \frac{A_\gamma}{A_a + A_\gamma} \cdot 100 \quad (2)$$

where A_α is the area under α diffraction peaks and A_γ is the area under γ diffraction peaks [27].

3. Results and discussion

3.1. Thermomechanical behavior of $Fe_{20}Ni_{80}$/PA6 PNCs

Figure 1 presents the coefficient of thermal expansion (CTE) of neat PA6, UMB2-SU and UMB2-NC PNCs at different temperature intervals. It is obvious that UMB2-SU and UMB2-NC PNCs possess considerably lower CTE values than that of neat PA6, through the temperature interval of 25–50 °C that is

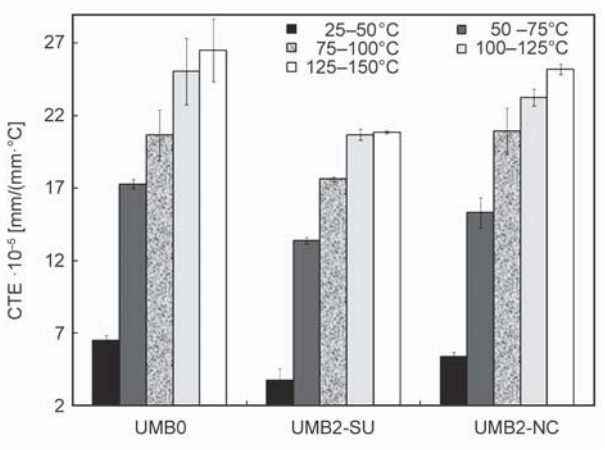

Figure 1. Coefficient of thermal expansion of neat PA6, UMB2-SU and UMB2-NC PNCs at different temperature intervals

below the T_g of PA6 (~50–60 °C) [28]. This indicates that the interfacial interactions between nc-$Fe_{20}Ni_{80}$ alloy of either SU or NC geometry and glassy PA6 phase are strong enough to modify the polymer chains dynamics and lead to significantly improved bulk thermal dimensional stability of PNCs relative to that of neat PA6. It is notable that the improvement in thermal dimensional stability is much more pronounced for the case of alloy particles with the SU geometry rather than the NC one as the CTE of UMB2-SU PNC is 43% lower while that of UMB2-NC PNC is only 18% lower, compared to that of neat PA6.

For temperature intervals above the T_g of PA6 and up to 150 °C, although PA6 becomes in the rubbery state, UMB2-SU PNC still exhibits better thermal dimensional stability relative to neat PA6. The CTE UMB2-SU PNC at higher temperatures i.e., 100–125 and 125–150 °C range, is almost the same as that of neat PA6 at lower temperatures i.e., 75–100 °C range, indicating that more energy is required to activate the segmental motion of polymer chains in the presence of SU nc $Fe_{20}Ni_{80}$ particles. However, the enhancement of PA6 thermal dimensional stability by SU nc $Fe_{20}Ni_{80}$ particles when the polymer is in the rubbery state is decreased to around half that when it is in the glassy state. This is expected and can be attributed to the increased mobility of polymer molecules in the rubbery state. Such phenomenon counteracts the reinforcing effect of SU nc $Fe_{20}Ni_{80}$ particles which restricts the PA6 chains mobility, leading to less net improvement in the nanocomposite thermal dimensional stability. On the other hand, the en-

hancement of PA6 thermal dimensional stability by NC nc $Fe_{20}Ni_{80}$ particles is highly deteriorated beyond PA6 T_g. Thus, UMB2-NC PNC exhibits slightly improved thermal dimensional stability relative to neat PA6 within temperature range 50–150 °C. The remarkable thermal dimensional stability of UMB2-SU PNC over neat PA6 and UMB2-NC PNC, in both glassy and rubbery states of PA6, implies stronger filler-matrix interfacial interactions within the $Fe_{20}Ni_{80}$/PA6 PNC when alloy particles assume the SU geometry rather than the NC one.

In penetration test, a fixed load of 0.3 N was applied on the sample by a needle and the variation of needle level with increased temperature from ambient to 180 °C was recorded. The plots, demonstrating needle level versus temperature, for PA6, UMB2-SU and UMB2-NC PNCs are displayed in Figure 2. For all the samples, the needle level increases initially with increased temperature until a certain temperature beyond which decreases dramatically. This is due to thermal expansion of samples with heating up until could be penetrated by the needle at a certain temperature that expresses the material softening temperature (T_S). Beyond T_S the penetration depth within sample is increased as the temperature is getting higher due to further material softening. It is clearly obvious that UMB2-SU and UMB2-NC PNCs have significantly higher T_S than neat PA6 and UMB2-SU PNC shows synergistic softening temperature as compared to UMB2-NC one. Thus, the T_S of UMB2-SU and UMB2-NC PNCs are higher by 113 and 63% respectively relative to that of neat PA6. Higher T_S is in good agreement with lower CTE of $Fe_{20}Ni_{80}$/PA6 PNCs compared to neat PA6, confirming pinning of

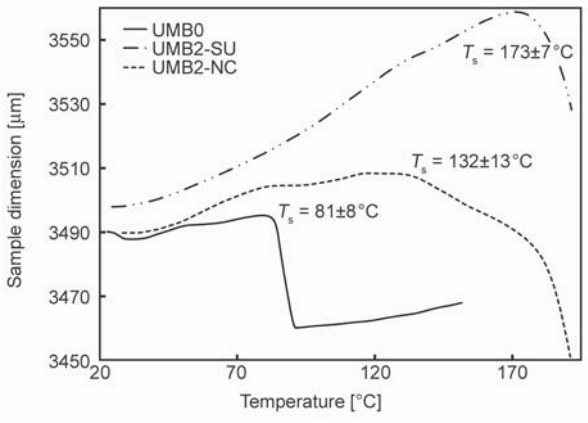

Figure 2. Thermomechanical penetration behavior of neat PA6, UMB2-SU and UMB2-NC PNCs

polymer chains by nc $Fe_{20}Ni_{80}$ particles of either SU or NC morphology leading to restricted molecular segmental motions within nanocomposites under thermomechanical stresses. Further, the highly synergistic T_S agrees well with the significantly suppressed CTE of UMB2-SU PNC as compared to those of UMB2-NC one, indicating remarkable rigidity of UMB2-SU PNC against thermomechanical stresses rather than UMB2-NC PNC does.

3.2. Microstructure of $Fe_{20}Ni_{80}$/PA6 PNCs

3.2.1. Morphology

SEM micrographs of SU and NC nc $Fe_{20}Ni_{80}$ particles and their corresponding nanocomposites are presented in Figure 3. SU nc $Fe_{20}Ni_{80}$ alloy, Figures 3a–b, exhibits spherical morphology with average particle diameter of about 230 nm. In addition, many sea urchin-like particles are also observed. Such sea urchin-like architecture is composed of several dendrites with average diameter of about 122 nm, growing out from the surface of the spherical core, as clearly seen in the high magnification image (Figure 3b). On the other hand, necklace-like chains with average diameter of about 225 nm dominate the architecture of NC nc $Fe_{20}Ni_{80}$ alloy, as shown in Figures 3c–d. Unlike the spherical-sea urchin like particles, the necklace-like chains appear quite smooth and little bit branched, few dendritic branches can be hardly seen at high magnification (Figure 3d). At this point the architecture of SU nc $Fe_{20}Ni_{80}$ alloy can be considered quasi-isotropic while that of NC nc $Fe_{20}Ni_{80}$ alloy is anisotropic.

Regarding UMB2-SU PNC, Figure 3e illustrates good distribution of submicron aspheric nc $Fe_{20}Ni_{80}$ particles within PA6 matrix. In the high magnification SEM image, Figure 3f, spherical and sea-urchin alloy particles, denoted by black and white arrows respectively, can be clearly distinguished within PA6 matrix. The good distribution of SU nc $Fe_{20}Ni_{80}$ particles within PA6 matrix along with the highly branched nature of sea-urchin particles allow large filler-matrix interface and therefore extensive interfacial interactions between the two phases, leading to efficient reinforcement of PA6 phase by SU alloy particles. Magnified view of the area within the white square shows constrained polymer regions, with a width in the order of tens nanometer, in between dendrites of alloy sea urchin particles. Often, confinement effect

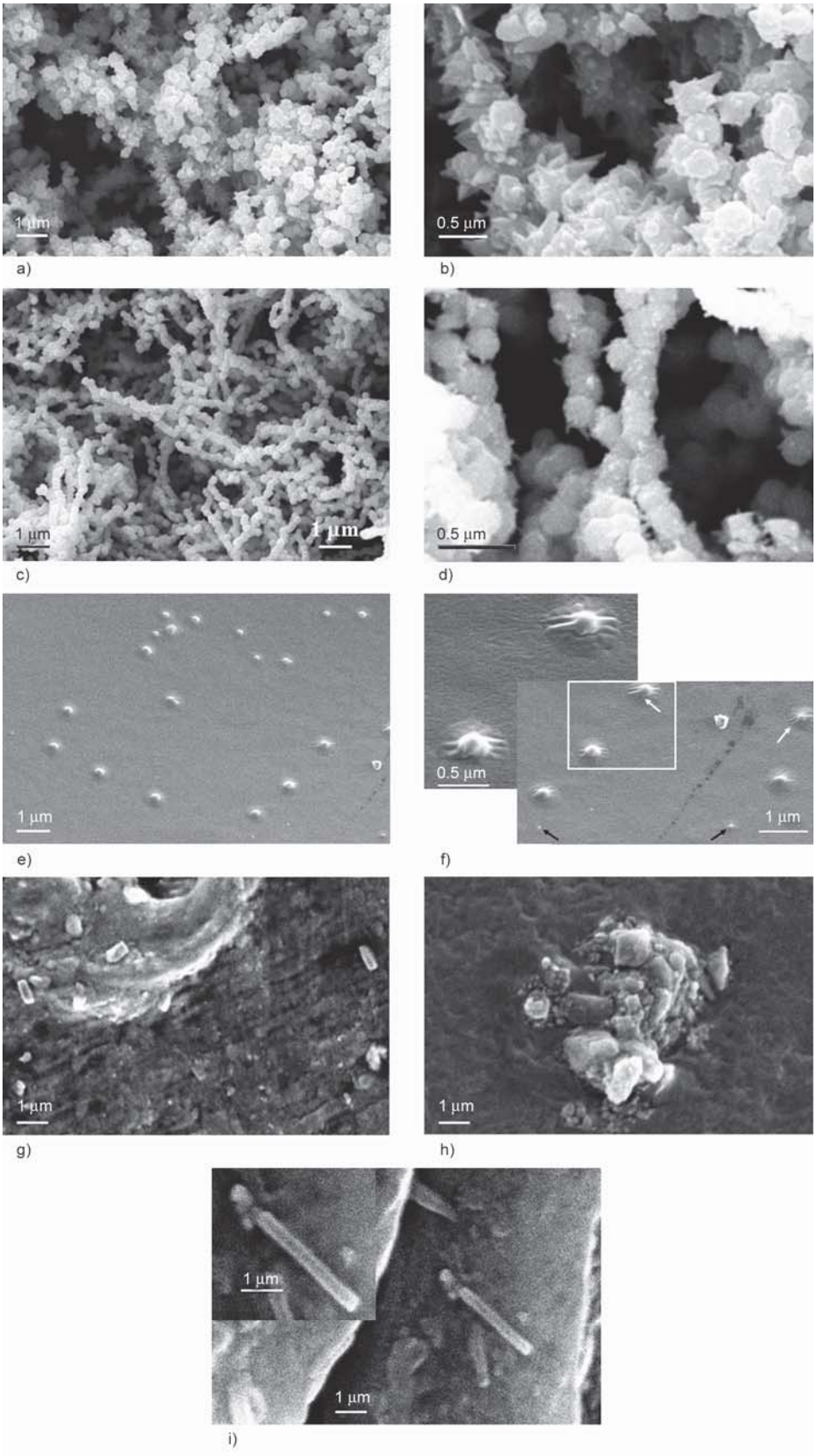

Figure 3. SEM micrographs of (a–b) SU nc $Fe_{20}Ni_{80}$ alloy, (c–d) NC nc $Fe_{20}Ni_{80}$ alloy, (e–f) UMB2-SU PNC and (g–i) UMB2-NC PNC

of SU nc $Fe_{20}Ni_{80}$ particles on the polymer chains in these narrow constraint regions is much more pronounced than on those in the free volume of UMB2-SU PNC. Therefore, such constrained polymer regions are characterized by dramatically restricted chains mobility rather than polymer segments in the free volume of UMB2-SU PNC. Thus, their abundance within UMB2-SU PNC can enable a secondary reinforcing mechanism which in addition to the primary reinforcing effect of SU nc $Fe_{20}Ni_{80}$ particles significantly contributes to the macroscopic properties of the nanocomposite, leading to the dramatically enhanced thermomechanical rigidity of UMB2-SU PNC as compared to that of neat PA6.

SEM micrographs of UMB2-NC PNC, Figures 3g–i, at various regions of the specimen reveal the presence of three different forms of NC nc $Fe_{20}Ni_{80}$ particles within PA6 matrix. Thus, NC nc $Fe_{20}Ni_{80}$ particles appear either as short dispersed rods, agglomeration of short rods or long dispersed rods within PA6 matrix, as seen in Figures 3g, h and i respectively. Obviously, the short rods, with a length of hundreds nanometers, are considerably shorter than the nc $Fe_{20}Ni_{80}$ necklace-like chains, which are few microns in length as depicted in Figures 3c–d. On the other hand, the long rods are almost comparable in length to the nc $Fe_{20}Ni_{80}$ necklace-like chains. This reveals the breaking up of some alloy necklace chains while preparing UMB2-NC PNC, due to the intensive mixing forces applied during the UMB compounding process. Such intensive mixing forces, however, could not homogeneously disperse the nc $Fe_{20}Ni_{80}$ short rods, originated from breakage of alloy necklace chains, as SU nc $Fe_{20}Ni_{80}$ particles, leading to some extent of nc $Fe_{20}Ni_{80}$ agglomeration within UMB2-NC PNC. The worse dispersibility of NC nc $Fe_{20}Ni_{80}$ particles compared to SU nc $Fe_{20}Ni_{80}$ particles can be attributed to the substantial increase of the alloy permanent magnetic moment as the degree of particle anisotropy increases. It has been noted that the remanent magnetization value at zero magnetic field (M_r) for the NC nc $Fe_{20}Ni_{80}$ alloy is 12.3 emu/g as compared to 8.5 emu/g for the SU nc $Fe_{20}Ni_{80}$ alloy [22]. The crucial role of the magnetic nanofiller's geometry in controlling its particles' dispersion and distribution within PNCs due to changing their magnetic characteristics, can be considered among the most important new findings of this study.

It is possible that few filler agglomerates within UMB2-NC PNC reduce the available interface and therefore the interfacial interactions between NC nc $Fe_{20}Ni_{80}$ particles and PA6 matrix, limiting thus the reinforcing effect of alloy particles on polymer chains. Further, short and long dispersed rods of NC nc $Fe_{20}Ni_{80}$ alloy within UMB2-NC PNC appear unbranched, as shown in the inset in Figure 3i, which clearly indicates that the rod surface is entirely smooth and unbranched. This results in absence of constrained polymer regions in between alloy segments which, in turn, eliminates the secondary reinforcing effect within UMB2-NC PNC. The limited reinforcing effect of NC alloy particles as compared to SU alloy particles on PA6 chains along with the absence of the secondary reinforcing effect within UMB2-NC PNC, are mainly responsible for the worse thermomechanical rigidity of UMB2-NC PNC as compared to the UMB2-SU one.

3.2.2. Crystalline structure

The degree of crystallinity (X_C), melting (T_m) and crystallization temperatures (T_c) of neat PA6 and PA6 phase within the nanocomposites have been characterized, using DSC melting and crystallization thermograms. The results, which reflect an average of three measurements, are listed in Table 2. It is noted that the T_m of PA6, dictated by the lamellar thickness of crystals, is insensitive to the presence of nc $Fe_{20}Ni_{80}$ alloy of either SU or NC particle geometry within polymer matrix. Unlike T_m, clearly the PA6 degrees of crystallinity in UMB2-SU and UMB2-NC PNCs are higher than that of neat PA6. Also, the PNCs exhibit slightly higher T_c of PA6 phase, as compared to neat PA6. This can be because the nc $Fe_{20}Ni_{80}$ particles act as effective nucleating centers, allowing thus the PA6 crystallization to start earlier and inducing the rate of crystallization leading eventually to increased degree of crystallinity. Figure 4 further supports such hypothesis, as the observed sub-T_m exotherm in the displayed DSC heating scans is more

Table 2. DSC data for neat PA6, UMB2-SU and UMB2-NC PNCs

Sample	X_C [%]	T_m [°C]	T_c [°C]
UMB0	32.3±0.4	222.7±1.2	198.3±0.10
UMB2-SU	37.5±0.9	222.3±0.5	198.9±0.30
UMB2-NC	36.4±0.4	221.7±1.0	199.1±0.07

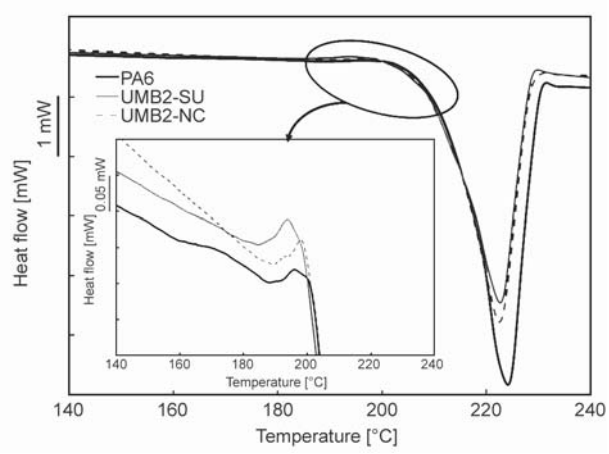

Figure 4. MDSC heating traces of neat PA6, UMB2-SU and UMB2-NC PNCs

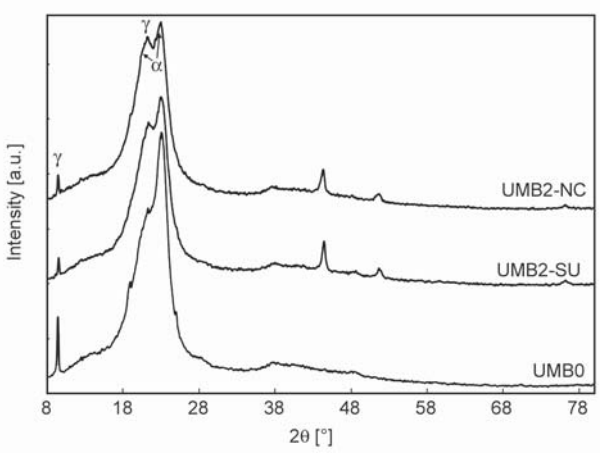

Figure 5. XRD patterns of neat PA6, UMB2-SU and UMB2-NC PNCs

pronounced for UMB2-SU and UMB2-NC PNCs as compared to neat PA6. The enhancement of the sub-Tm exotherm, which is attributed to the recrystallization of PA6 chains prior to melting, upon addition of nc $Fe_{20}Ni_{80}$ alloy to PA6 confirms the nucleating action of alloy particles within both PNCs. Although the alloy surface available for nucleation of polymer chains is significantly larger within UMB2-SU PNC than in UMB2-NC one, as evidenced from the SEM micrographs, crystallization of PA6 phase has not been further induced within UMB2-SU PNC; values of the area under the sub-T_m exotherm, T_c and X_C for the PA6 phase are almost comparable within both PNCs. Most probably, this is due to the increased restriction of PA6 chain mobility which, in turn, increasingly hinders the crystallization of PA6 molecules within UMB2-SU PNC as compared to the UMB2-NC one.

It is worth mentioning that the increased degree of crystallinity of PA6 phase in both PNCs is a possible reinforcing mechanism that contributes to the significantly enhanced thermomechanical rigidity of such nanocomposites as compared to neat PA6. However, the parameter doesn't contribute to the considerably improved thermomechanical rigidity of UMB2-SU PNC over UMB2-NC one, as both nanocomposites possess a comparable PA6 degree of crystallinity.

XRD patterns for neat PA6 and the nanocomposites are presented in Figure 5. The peaks around $2\theta \approx 20$ and 23° are assigned to α1 and α2 crystal planes of PA6, respectively while those around $2\theta \approx 10$ and 21° are assigned to γ1 and γ2 crystal planes of PA6, respectively [24, 29]. The observed peaks at $2\theta =$ 44.4, 51.6, 76.2° in the XRD patterns of UMB2-SU and UMB2-NC PNCs, are corresponding to the (111), (200) and (220) crystal planes of FCC-Awaruite $FeNi_3$, respectively [22].

It is noticed that the nanocomposites exhibit increased relative fraction of γ-form to α-form PA6 crystals, as compared to neat PA6. Thus, the percentage of γ-form crystals with respect to the total crystalline PA6 phase measures 20, 26 and 41% for neat PA6, UMB2-SU and UMB2-NC PNCs, respectively. This indicates that the less ordered γ PA6 crystalline phase is favored in the presence of nc $Fe_{20}Ni_{80}$ particles, in particular, when alloy particles assume the NC geometry. This is probably because the nc $Fe_{20}Ni_{80}$ particles disturb the PA6 crystals while being formed during the crystallization process. Higher degree of alloy particles agglomeration within the UMB2-NC PNC as compared to the UMB2-SU one, may be responsible for the significantly increased PA6 γ-phase [%] within the former nanocomposite than in the latter one. This is because as the alloy particles are getting larger in size, they further disturb the PA6 crystalline order, leading to the profusion of less ordered PA6 γ-phase crystals in the nanocomposite. The significantly higher PA6 γ-phase [%] within UMB2-NC PNC than in UMB2-SU one, might be one reason for the smaller thermomechanical rigidity of the former nanocomposite as compared to the latter one.

The average crystallite sizes of nc $Fe_{20}Ni_{80}$ alloys within the UMB2-SU and UMB2-NC PNCs, calculated based on the full width at half maximum of the (111) peak using the Scherrer formula [30], are 27 and 43 nm, respectively. They are significantly larger

than the crystallite sizes of the corresponding as synthesized nc $Fe_{20}Ni_{80}$ alloys; which are 16 and 20 nm for the alloy particles with SU and NC geometries, respectively [22]. This indicates some extent of alloy crystal growth during the thermal processing of PNCs, but eventually the nanocrystalline nature of $Fe_{20}Ni_{80}$ alloy is still preserved within both nanocomposites. The significantly lower nanocrystallite size of SU nc $Fe_{20}Ni_{80}$ alloy versus NC nc $Fe_{20}Ni_{80}$ alloy, reveals remarkable thermomechanical rigidity and soft magnetic properties of the alloy within the UMB2-SU PNC as compared to the UMB2-NC one. This contributes to the considerably improved overall performance of UMB2-SU PNC over UMB2-NC one.

3.3. Magnetic properties of $Fe_{20}Ni_{80}$/PA6 PNCs

Figure 6 shows the room-temperature magnetic hysteresis loops, representing the magnetization (M) versus magnetic field (H), for neat PA6, UMB2-SU and UMB2-NC PNCs. Neat PA6 exhibits a weak diamagnetic response to the applied magnetic field; the up-right inset in Figure 6 indicates a very low magnetization of 0.01 emu/g for neat PA6 at the maximum applied magnetic field (≈25 kG). Thus, it can be considered a nonmagnetic material. Impressively, UMB2-SU and UMB2-NC PNCs exhibit a ferromagnetic behavior with dramatically higher saturation magnetization (M_s) than the maximum magnetization of neat PA6; M_s equals 0.43 emu/g for UMB2-SU PNC and 0.54 emu/g for UMB2-NC one. It is found elsewhere that PNCs filled with other pristine (not functionalized or surface modified) ferromagnetic nanocrystalline metallic materials such as Fe_3O_4 [31], Fe_2O_3 [32], Ni-Zn ferrite [33], and Ba-ferrite [34] exhibit M_s of about 0.5 emu/g at 5–9 wt% filler content. Herein, $Fe_{20}Ni_{80}$/PA6 PNCs (UMB2-SU and UMB2-NC PNCs) can attain such M_s value at significantly lower filler content, indicating that nc $Fe_{20}Ni_{80}$ alloy based PNCs can be of great potential in the electromagnetic applications.

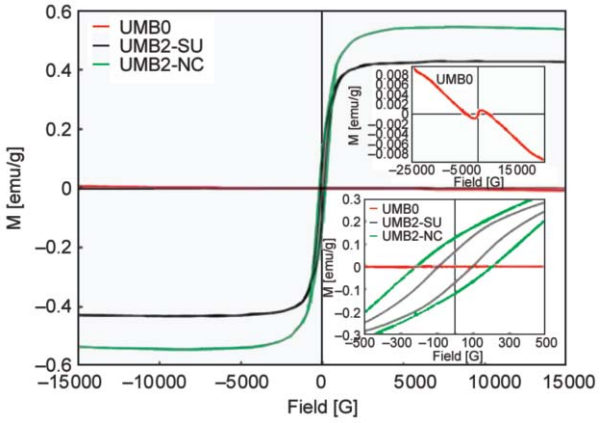

Figure 6. Room temperature magnetic hysteresis loops of neat PA6, UMB2-SU and UMB2-NC PNCs

Important magnetic parameters including initial magnetic susceptibility (χ_{ini}), saturation magnetization (M_s), saturation field (H_s), remanent magnetization (M_r), squareness (M_r/M_s) and coercivity (H_c), have been extracted from the M-H initial curves and hysteresis loops of the UMB2-SU and UMB2-NC PNCs, using IDEAS-VSM4 software. The data are summarized in Table 3. The corresponding magnetic parameters of the as synthesized SU and NC nc $Fe_{20}Ni_{80}$ alloys, reported in Mohamed's previous work [22], are also listed in Table 3. χ_{ini} is equal to $(dM/dH)_{H\to 0}$; it is determined from the initial magnetization curve. M_s is the magnetization value to $(1/H) = 0$, H_s is the magnetization field when $dM/dH \to 0$, M_r is the remanent material magnetization value at zero field, M_r/M_s is a measure of how square the hysteresis loop is and H_c is the field strength required to bring the material back to zero magnetization. As shown the SU nc $Fe_{20}Ni_{80}$ alloy possesses slightly higher χ_{ini} and M_s and lower H_s by 6, 3 and 3% respectively, as compared to the NC nc $Fe_{20}Ni_{80}$ alloy. On the other hand, M_r, M_r/M_s and H_c of the SU nc $Fe_{20}Ni_{80}$ alloy are significantly smaller than those of the NC nc $Fe_{20}Ni_{80}$ alloy by 45, 48 and 26% respectively. Higher χ_{ini} implies greater permeability of alloy particles to the magnetic moment when assuming quasi-iso-

Table 3. Room-temperature magnetic properties of nc $Fe_{20}Ni_{80}$ alloys of SU and NC geometries and their PA6 based nanocomposites

Sample	χ_{ini} [emu/g/G]	M_s [emu/g]	H_s [G]	M_r [emu/g]	M_r/M_s	H_c [G]
SU-$Fe_{20}Ni_{80}$	0.146	78.820	14848	8.500	0.108	85.760
UMB2-SU	$0.76\cdot10^{-3}$	0.433	6233	0.066	0.153	92.584
NC-$Fe_{20}Ni_{80}$	0.138	76.650	15290	12.300	0.160	108.330
UMB2-NC	$0.63\cdot10^{-3}$	0.544	7500	0.123	0.227	197.980

tropic architecture (SU geometry) rather than anisotropic one (NC geometry). Therefore the SU nc $Fe_{20}Ni_{80}$ alloy exhibits easier magnetization/demagnetization behavior, evidenced by higher χ_{ini} and M_s along with lower H_s, M_r, M_r/M_s and H_c, i.e. improved soft magnetic character than the NC nc $Fe_{20}Ni_{80}$ alloy does.

Considering the effect of alloy crystallite size besides the predominant effect of alloy geometrical architecture on the magnetic properties, interprets why M_s is slightly decreased but M_r and H_c are significantly increased as transfer from SU to NC nc $Fe_{20}Ni_{80}$ alloy. It is known that the M_s of ferromagnetic nanocrystalline metallic materials is suppressed with decreased crystallite size due to the enhanced surface spin disorder which conflicts with the magnetic moment induced by the external applied magnetic field. On the other hand, M_r and H_c are reduced with the decreased crystallite size because the crystal magnetic behavior is getting toward the single-domain behavior. Such single-domain behavior, characterized by M_r and H_c tend to zero, dominates at crystallite size lower than the critical size (d_c). The estimated d_c is about 20–30 nm for ferromagnetic nanocrystalline metallic materials [35]. Thus, the little increase of crystallite size from 16 nm in the SU nc $Fe_{20}Ni_{80}$ alloy to 20 nm in the NC nc $Fe_{20}Ni_{80}$ alloy, has resulted in a small increase in the alloy M_s. This counteracted the main decrease in M_s due to the increased anisotropy of alloy architecture. Consequently, a slight net decrease in the M_s value is observed for the NC nc $Fe_{20}Ni_{80}$ alloy. On contrary, both factors i.e., increased anisotropy of alloy architecture and alloy crystallite size, enhance the M_r and H_c values. Accordingly, NC nc $Fe_{20}Ni_{80}$ alloy possesses considerably higher M_r and H_c than SU nc $Fe_{20}Ni_{80}$ alloy.

Regarding the polymer nanocomposites, χ_{ini} of UMB2-SU PNC is higher than that of UMB2-NC PNC by 20%, indicating that the UMB2-SU PNC is significantly more permeable to the magnetic moment than the UMB2-NC one. Therefore, the magnetization/demagnetization of UMB2-SU PNC is considerably facile, as compared to that of UMB2-NC PNC. This is confirmed as H_s of the UMB2-SU PNC is 20% smaller than that of the UMB2-NC one. Moreover, the UMB2-SU PNC possesses almost one-half M_r and H_c and two-third M_r/M_s, compared to the UMB2-NC one. Thus, UMB2-SU PNC with a coercivity less than 95 G can be considered a magnetically soft material [36], whereas UMB2-NC PNC with a coercivity of about twice that limit is a hard magnetic material.

Lower M_s of UMB2-SU PNC than that of UMB2-NC PNC by about 20%, doesn't mean difficult magnetization of the former PNC as compared to the latter one. This is because the behavior of other magnetic properties, χ_{ini}, H_s, M_r, M_r/M_s and H_c, contradicts such hypothesis. The magnetic performances of the $Fe_{20}Ni_{80}$/ PA6 PNCs are determined by, in addition to the magnetic properties of the corresponding as synthesized alloys, other three factors: (a) filler-matrix interfacial interactions, (b) presence of narrow constrained polymer regions in between branches of the sea urchin alloy particles within the UMB2-SU PNC and (c) different crystallite sizes of the nc $Fe_{20}Ni_{80}$ alloys within PNCs as compared to the as synthesized ones. The constrained polymer regions in between alloy segments are often largely influenced by the alloy characteristics rather than polymer segments in the free volume and therefore can enable a secondary soft magnetic effect within the UMB2-SU PNC. Thus, the extensive interfacial interactions between PA6 matrix and SU alloy particles rather than NC ones and the secondary soft magnetic effect present in the UMB2-SU PNC, have made the PA6 matrix within the UMB2-SU PNC less resistive to the magnetic moment than that within the UMB2-NC PNC. Consequently, this lead to considerably easier magnetization/demagnetization of UMB2-SU PNC. The increased gap between crystallite sizes of SU nc $Fe_{20}Ni_{80}$ alloy (27 nm) and NC nc $Fe_{20}Ni_{80}$ alloy (43 nm) within PNCs, as compared to the case for the as synthesized alloys, has resulted in two effects. First, it has caused the M_r and H_c of SU alloy to be lower than those of NC alloy within PNCs, by significantly more percentages than those recorded for the as synthesized alloys. This has subsequently contributed to the large gap between the M_r and H_c of UMB2-SU PNC and those of UMB2-NC one. Second, it might cause the M_s to invert its trend i.e. M_s of SU alloy becomes lower than that of NC alloy and this may be the reason for the lower M_s of the UMB2-SU PNC than that of the UMB2-NC one.

The UMB2-SU PNC is regarded a better suit for the electromagnetic devices requiring good soft magnetic properties, where the nc $Fe_{20}Ni_{80}$ alloy has been

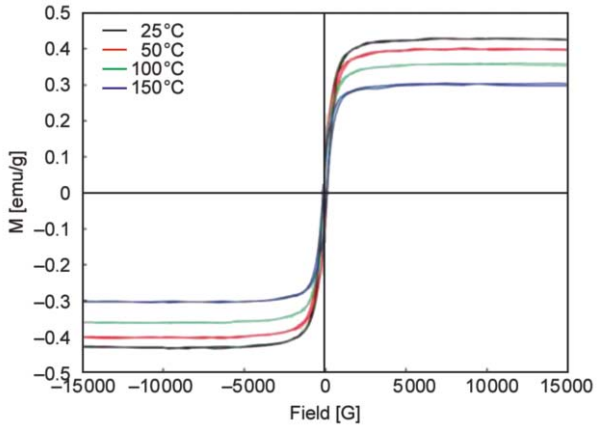

Figure 7. Magnetic hysteresis loop of UMB2-SU PNC as a function of temperature

Table 4. Magnetic properties of UMB2-SU PNC at different temperatures

Temperature [°C]	χ_{ini} [emu/g/G]	M_s [emu/g]	M_r [emu/g]	H_s [G]
25	$0.76 \cdot 10^{-3}$	0.433	0.066	92.584
50	$0.76 \cdot 10^{-3}$	0.404	0.064	87.615
100	$0.69 \cdot 10^{-3}$	0.363	0.051	75.145
150	$0.63 \cdot 10^{-3}$	0.305	0.042	66.630

extensively exploited, due to its distinctive morphological features, remarkable thermomechanical rigidity and room-temperature soft magnetic character. Accordingly, the temperature-dependent magnetic behavior has been only investigated for the UMB2-SU PNC, in order to explore its thermal soft magnetic stability.

Figure 7 displays the *M-H* hysteresis loop of UMB2-SU PNC as a function of temperature up to 150 °C. The corresponding magnetic parameters are listed in Table 4. It is noted that all the magnetic parameters including χ_{ini}, M_s, M_r and H_c are reduced; indicating suppressed ferromagnetic nature of the nanocomposite, with the increased temperature. This is due to the greater thermal activation energy of spins at higher temperature [37]. Interestingly, χ_{ini} and M_s at 100 °C are little lower than those at room temperature by 9 and 16% respectively. This reveals that the ferromagnetic performance of the UMB2-SU PNC is still relatively good at such high temperature, i.e. good thermal soft magnetic stability of the nanocomposite.

4. Conclusions

Results of the study reveal a major role of the nc $Fe_{20}Ni_{80}$ alloy geometry in controlling the bulk properties of the 2 wt% $Fe_{20}Ni_{80}$/PA6 PNC. The UMB2-SU PNC, filled with alloy particles of SU geometry, exhibits remarkable thermomechanical rigidity and room-temperature soft magnetic properties, relative to neat PA6 and to the UMB2-NC PNC, which is filled with alloy particles of NC geometry. Variant nanocomposites' overall performances can be due to the distinctive microstructural differences between them, evidenced from the SEM and XRD analyses. Morphological observations disclose good dispersion and distribution of SU nc $Fe_{20}Ni_{80}$ particles within the UMB2-SU PNC while some agglomerates of NC nc $Fe_{20}Ni_{80}$ short rods are present in the UMB2-NC PNC. The crucial role of the magnetic nanofiller's geometry in controlling its particles' dispersion and distribution within PNCs is first recognized in this study and attributed to changes in the filler magnetic properties. Thus, improved filler-matrix interfacial interactions dominate the UMB2-SU PNC as compared to the UMB2-NC one. Additionally, the SEM images reveal the presence of narrow constraint polymer regions in between branches of the sea urchin alloy particles within the UMB2-SU PNC. Whereas such phenomenon is absent in the UMB2-NC PNC because NC alloy particles are unbranched. These constrained polymer regions enable secondary reinforcing and soft magnetic effects within the UMB2-SU PNC. Thus, the extensive filler-matrix interfacial interactions and the significantly lower alloy crystallite size within the UMB2-SU PNC as compared to the UMB2-NC one, along with the secondary reinforcing and soft magnetic effects present in the UMB2-SU PNC are the main factors responsible for the superior overall performance of UMB2-SU PNC. The considerably lower PA6 γ-crystal type [%] within the UMB2-SU PNC than in the UMB2-NC one, contributes also to the improved thermomechanical rigidity of the UMB2-SU PNC. The PA6 degree of crystallinity, however, is comparable in both nanocomposites and therefore doesn't contribute to their variant thermomechanical rigidities. On the other hand, the temperature-dependent magnetic behavior of the UMB2-SU PNC indicates that its ferromagnetic performance is quite good up to 100 °C. Overall, the good thermomechanical rigidity and thermal soft magnetic stability of UMB2-SU PNC infer that the material can sustain the thermal stresses present in the electromagnetic applications. Accordingly, the $Fe_{20}Ni_{80}$/PA6 PNCs based on nc $Fe_{20}Ni_{80}$ alloy of SU

particle geometry can lead to new promising structural material for electromagnetic applications.

Acknowledgements

Authors deeply appreciate Mr. Mahmoud Darwish, Mrs. Basant Ewida and Ms. Sarah Abdelaziz, Central Lab. Engineers at SRTA City, for performing the SEM imaging and thermomechanical analysis. This research received no specific grant from any funding agency. Thus, financial support for this research has been provided by the authors' universities; SRTA City, Egypt and Georgia Tech, USA.

References

[1] Moreno-Mañas M., Pleixates R.: Formation of carbon–carbon bonds under catalysis by transition-metal nanoparticles. Accounts of Chemical Research, **36**, 638–643 (2003).
DOI: 10.1021/ar020267y

[2] Sellmyer D. J., Yu M., Kirby R. D.: Nanostructured magnetic films for extremely high density recording. Nanostructured Materials, **12**, 1021–1026 (1999).
DOI: 10.1016/S0965-9773(99)00291-3

[3] Hyeon T.: Chemical synthesis of magnetic nanoparticles. Chemical Communications, **8**, 927–934 (2003).
DOI: 10.1039/B207789B

[4] Gupta K., Gupta M.: Synthesis and surface engineering of iron oxide nanoparticles for biomedical applications. Biomaterials, **26**, 3995–4021 (2005).
DOI: 10.1016/j.biomaterials.2004.10.012

[5] Mornet S., Vasseur S., Grasset F., Verveka P., Goglio G., Demourgues A., Portier J., Pollert E., Duguet E.: Magnetic nanoparticle design for medical applications. Progress in Solid State Chemistry, **34**, 237–247 (2006).
DOI: 10.1016/j.progsolidstchem.2005.11.010

[6] Elliott D. W., Zhang W-X.: Field assessment of nanoscale bimetallic particles for groundwater treatment. Environmental Science and Technology, **35**, 4922–4926 (2001).
DOI: 10.1021/es0108584

[7] Panigrahi P., Pati R.: Tuning the ferromagnetism of one-dimensional Fe/Pt/Fe multilayer barcode nanowires *via* the barcode layer effect. Physical Reviews B, **76**, 024431/1–024431/6 (2007).
DOI: 10.1103/PhysRevB.76.024431

[8] Ma F., Qin Y., Li Y-Z.: Enhanced microwave performance of cobalt nanoflakes with strong shape anisotropy. Applied Physical Letters, **96**, 202507/1–202507/3 (2010).
DOI: 10.1063/1.3432441

[9] Li J., Huang J., Qin Y., Ma F.: Magnetic and microwave properties of cobalt nanoplatelets. Materials Science and Engineering B, **138**, 199–204 (2007).
DOI: 10.1016/j.mseb.2006.12.001

[10] Batlle X., Labarta A.: Finite-size effects in fine particles: Magnetic and transport properties. Journal of Physics D: Applied Physics, **35**, R15–R42 (2002).
DOI: 10.1088/0022-3727/35/6/201

[11] Gubin S. P.: Magnetic nanoparticles. Wiley, Weinheim (2009).

[12] McCarthy J. R., Weissleder R.: Multifunctional magnetic nanoparticles for targeted imaging and therapy. Advanced Drug Delivery Reviews, **60**, 1241–1251 (2008).
DOI: 10.1016/j.addr.2008.03.014

[13] Maleki H., Simchi A., Imami M., Costa B. F.: Size-controlled synthesis of superparamagnetic iron oxide nanoparticles and their surface coating by gold for biomedical applications. Journal of Magnetism and Magnetic Materials, **324**, 3997–4005 (2012).
DOI: 10.1016/j.jmmm.2012.06.045

[14] Wilson J. L.: Synthesis and magnetic properties of polymer nanocomposites. MsC Thesis, Department of Physics, College of Arts and Sciences, University of South Florida (2004).

[15] Jeon I-Y., Baek J-B.: Nanocomposites derived from polymers and inorganic nanoparticles. Materials, **3**, 3654–3674 (2010).
DOI: 10.3390/ma3063654

[16] Jordan J., Jacob K. I., Tannenbaum R., Sharaf M. A., Jasiuk I.: Experimental trends in polymer nanocomposites – A review. Materials Science and Engineering: A, **393**, 1–11 (2005).
DOI: 10.1016/j.msea.2004.09.044

[17] McCrea J. L., Palumbo G., Hibbard G. D., Erb U.: Properties and applications for electrodeposited nanocrystalline Fe-Ni alloys. Reviews on Advanced Materials Science, **5**, 252–558 (2003).

[18] Lima E. Jr., Drago V., Bolsoni R., Fichtner P. F. P.: Nanostructured $Fe_{50}Ni_{50}$ alloy formed by chemical reduction. Solid State Communications, **125**, 265–270 (2003).
DOI: 10.1016/S0038-1098(02)00773-1

[19] Yeh Y-M., Tu G. C., Fang T-H.: Nanomechanical properties of nanocrystalline Ni–Fe mold insert. Journal of Alloys and Compounds, **372**, 224–230 (2004).
DOI: 10.1016/S0925-8388(03)01041-7

[20] Prieto P., Camarero J., Marco J. F., Jimenez E., Benayas J. M., Sanz J. M.: Characterization of nanocrystalline permalloy thin films obtained by nitrogen IBAD. IEEE Transactions on Magnetics, **44**, 3913–3916 (2008).
DOI: 10.1109/TMAG.2008.2002483

[21] Mohamed M. A. A., El-Maghraby A., Abd EL-Latif M., Farag H., Kalaitzidou K.: Nanocrystalline Fe-Ni alloy/polyamide 6 composites of high mechanical performance made by ultrasound-assisted master batch technique. Polymer Composites, **35**, 2343–2352 (2014).
DOI: 10.1002/pc.22901

[22] Mohamed M. A. A.: Facile directing agent-free synthesis and magnetism of nanocrystalline Fe–Ni alloy with tunable shape. Materials Science and Engineering: B, **190**, 7–12 (2014).
DOI: 10.1016/j.mseb.2014.09.007

[23] Wu Q., Liu X., Berglund L. A.: An unusual crystallization behavior in polyamide 6/montmorillonite nanocomposites. Macromolecular Rapid Communications, **22**, 1438–1440 (2001).
DOI: 10.1002/1521-3927(20011101)22:17<1438::AID-MARC1438>3.0.CO;2-U

[24] Hassani A. J., Mohd Ishak Z. A., Mohamed A. R.: Preparation and characterization of polyamide 6 nanocomposites using MWCNTs based on bimetallic Co-Mo/MgO catalyst. Express Polymer Letters, **8**, 177–186 (2014)
DOI: 10.3144/expresspolymlett.2014.21

[25] Shen L., Phang I. Y., Liu T.: Nanoindentation studies on polymorphism of nylon 6. Polymer Testing, **25**, 249–253 (2006).
DOI: 10.1016/j.polymertesting.2005.09.019

[26] Ito M., Mizuochi K., Kanamoto T.: Effects of crystalline forms on the deformation behaviour of nylon-6. Polymer, **39**, 4593–4598 (1998).
DOI: 10.1016/S0032-3861(97)10132-X

[27] Seltzer R., Frontini P. M., Mai Y-W.: Effect of hygrothermal ageing on morphology and indentation modulus of injection moulded nylon 6/organoclay nanocomposites. Composites Science and Technology, **69**, 1093–1100 (2009).
DOI: 10.1016/j.compscitech.2009.01.029

[28] Evstatiey M.: Polyamides. in 'Handbook of thermoplastics' (ed.: Olabisi O.) Marcel Dekker, New York, 641–664 (1997).

[29] Hu X., Zhao X.: Effects of annealing (solid and melt) on the time evolution of polymorphic structure of PA6/silicate nanocomposites. Polymer, **45**, 3819–3825 (2004).
DOI: 10.1016/j.polymer.2004.03.055

[30] Cullity B. D.: Elements of X-ray diffraction. Addison-Wesley Publishing, Boston (1978).

[31] Sun D. C., Sun D. S.: The synthesis and characterization of electrical and magnetic nanocomposite: PEDOT/PSS–Fe_3O_4. Materials Chemistry and Physics, **118**, 288–292 (2009).
DOI: 10.1016/j.matchemphys.2009.07.060

[32] Pour Z. S., Ghaemy M.: Fabrication and characterization of superparamagnetic nanocomposites based on epoxy resin and surface-modified γ-Fe_2O_3 by epoxide functionalization. Journal of Materials Science, **49**, 4191–4201 (2014).
DOI: 10.1007/s10853-014-8114-6

[33] Moeen Sh. J., Yousefi A. A.: Magnetic properties of PVDF-$Ni_{0.5}$ $Zn_{0.5}$ Fe_2O_4 nanocomposite. in 'Proceedings of the 4th International Conference on Nanostructures (ICNS4). Kish Island, Iran' 1371–1373 (2012).

[34] Kanapitsas A., Tsonos C., Psarras G. C., Kripotou S.: Barium ferrite/epoxy resin nanocomposite system: Fabrication, dielectric, magnetic and hydration studies. Express Polymer Letters, **10**, 227–236 (2016).
DOI: 10.3144/expresspolymlett.2016.21

[35] Mohammad-Beigi H., Yaghmaei S., Roostaazad R., Bardania H., Arpanaei A.: Effect of pH, citrate treatment and silane-coupling agent concentration on the magnetic, structural and surface properties of functionalized silica-coated iron oxide nanocomposite particles. Physica E: Low-dimensional Systems and Nanostructures, **44**, 618–627 (2011).
DOI: 10.1016/j.physe.2011.10.015

[36] Neelakanta P. S.: Handbook of electromagnetic materials monolithic and composite versions and their applications. CRC Press, Boca Raton (1995).

[37] Wilson J. L., Poddar P., Frey N. A., Srikanth H., Mohomed K., Harmon J. P., Kotha S., Wachsmuth J.: Synthesis and magnetic properties of polymer nanocomposites with embedded iron nanoparticles. Journal of Applied Physics, **95**, 1439–1443 (2004).
DOI: 10.1063/1.1637705

eXPRESS Polymer Letters Vol.10, No.10 (2016) 835–848
Available online at www.expresspolymlett.com
DOI: 10.3144/expresspolymlett.2016.78

Bark polyflavonoids from *Pinus radiata* as functional building-blocks for polylactic acid (PLA)-based green composites

D. E. García[1,2,3*], *J. C. Carrasco*[4], *J. P. Salazar*[5], *M. A. Pérez*[6], *R. A. Cancino*[5], *S. Riquelme*[5,7]

[1]Laboratorio de Fitoquímica, Departamento de Química Ambiental, Facultad de Ciencias, Universidad Católica de la Santísima Concepción (UCSC), Concepción, Biobío, Chile
[2]Centro de Investigación en Biodiversidad y Ambientes Sustentables (CIBAS), UCSC, Concepción, Biobío, Chile
[3]Investigador Asociado Área de Productos Químicos, Unidad de Desarrollo Tecnológico (UDT), Universidad de Concepción, Concepción, Biobío, Chile
[4]Área de Biomateriales, UDT, Universidad de Concepción, Concepción, Biobío, Chile
[5]Área de Productos Químicos, UDT, Universidad de Concepción, Concepción, Biobío, Chile
[6]Departamento de Polímeros, Facultad de Ciencias Químicas, Universidad de Concepción, Concepción, Chile
[7]Programa de Doctorado en Ciencias y Tecnologías Analíticas, Universidad de Concepción, Concepción, Biobío, Chile

Received 1 April 2016; accepted in revised form 22 May 2016

Abstract. Polylactic acid (PLA) was melt-blended with *Pinus radiata* unmodified and modified (hydroxypropyled) bark polyflavonoids in order to use such polyphenolic building-blocks as functional additives for envisaged applications. Rheological, morphological, molecular, thermal, and flexural properties were studied. Polyflavonoids improved blend processability in terms of short-time mixing. Furthermore, hydroxypropylated polyflavonoids improve miscibility in binary and ternary blends. Blend-composition affects crystallization-, melting-, and glass transition-temperature of PLA, as well as thermal resistance, and flexural properties of the blends. Polyflavonoids induced PLA-crystallization, and polymer-chain decomposition. Modified and unmodified bark polyflavonoids from radiata pine can be used successfully in PLA-based green composites beyond the food-packaging applications. The high compatibility between PLA and hydroxypropyled polyflavonoids highlights the potential of such phenolic derivatives for PLA-based material design.

Keywords: *polymer composites, hydroxypropyl polyflavonoid, radiata pine, polymer processability*

1. Introduction

The most important polymers in bioplastic engineering are aliphatic polyesters such as polylactic acid (PLA) [1]. Blending of PLA with other polymers such as polypropylene, natural rubbers, polyglycols (PEG), polyvinyl acetate, polyolefins, polymethyl methacrylate, and polycarbonate is an useful route towards modifying properties [2]. In addition, oligomers/polymers from lignocellulosic resources have been used as additives in order to reduce cost [3–5]. In fact, many advantages are recognized in binary and ternary blends regarding well dispersion into the PLA-matrix, and the nucleating effect of certain biopolymers which induced dramatic changes on mechanical properties [6].

Moreover, lignin and condensed tannin (polyflavonoids) have been successfully blended with PLA [7]. However, there are few reports which describe the effect of polyflavonoids on the PLA physicochemical properties. Polyphenols properties such as an-

*Corresponding author, e-mail: d.garcia@udt.cl

tioxidant capacity, strong UV-absorption, and remarkable biological activity (antibacterial/antifungal) enables utilizing polyflavonoids as functional building-blocks for PLA-based composites. Such selected properties might be considered in order to design functional materials based on key polyphenols properties such as O_2-active barrier for food packaging, UV-filter for selected outdoor applications, antimicrobial surfaces for food industry, as well as functional films and plastic devices for agriculture.

On the other hand, polyflavonoids are highly abundant in bark that is expected to play an important role in bioplastics engineering, and thermosetting systems [8, 9]. However, limited solubility in organic solvents and molten thermoplastics, and low thermal resistance of polyflavonoids are well-known drawbacks for polymer formulation, that is why chemical modification with alkylene oxides enabling less polar derivatives highly desirable for biomaterial design [10]. Hydroxypropyl polyflavonoids (HPT, Figure 1) from pine bark is easily synthesized at room temperature with propylene oxide, and the versatility as macro building-blocks has been demonstrated in several chemistries [11].

This work reports the preparation and characterization of several PLA-based blends using bark polyflavonoids (with and without chemical modification) as the main functional additive. Rheological, morphological, molecular, thermal, and flexural analyses were performed. The new types of PLA-based coloured materials are expected to play an important role beyond the traditional food-packaging applications of PLA.

2. Materials and methods

2.1. Chemicals

2.1.1. Polylactic acid (PLA)

Partially crystalline PLA (Polylactic acid) of Natureworks Ingeo™ Biopolymer 3251 grade supplied by NatureWorks® Co. LLC, USA, was the thermoplastic used in this study: average M_w 90 000–150 000 Dalton, polydispersity (D) 1.6, melting tempetarure (T_m) 170 °C, glass transition temperature (T_g) 61 °C, and L-lactide content of 98%.

2.1.2. Polyflavonoid

Non-water soluble radiata pine bark polyflavonoids (PRI) extracted with methanol/water solution (1:20, w/v) at 120 ºC was used [12]. Briefly, PRI are represented by a broad mixture of polyphenols (D: 1.5–2.8) mostly 4→8 linked [13, 14].

2.1.3. Hydroxypropyl polyflavonoid (PRI-3)

PRI-3 was synthesized by open-ring reaction (S_N2) using propylene oxide (PO) in alkali media (pH: 12) at room temperature (20–22 °C) as described by García *et al*. [8]. The parameters of the derivatization were described in detail elsewhere [9].

Briefly, PRI (100 g, ca. 80 mmol) was dissolved in 500 mL aq. 2 molL-1 NaOH, adjusted to pH 12 and stoichiometric PO-charge added. The reaction was carried out for 24 h with stirring. Before that, HCl (40% v/v) was added to adjust the pH to 2, producing a precipitate that was centrifuged. The supernatant was collected by decantation and the precipitate was washed five times with distilled water and freeze-

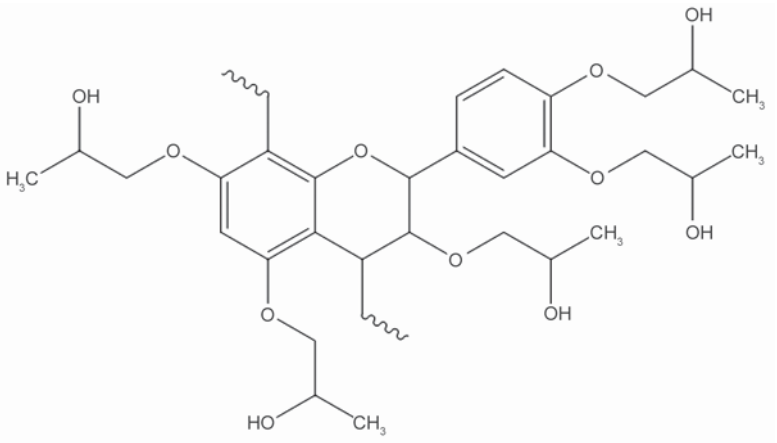

Figure 1. Chemical structure of hydroxypropyl polyflavonoid (C_{15} unit fully modified by hydroxypropylation)

dried. Reaction yields ranged from 82–90 wt% and the substitution degree (DS) was determined by ^{1}H-NMR (DS: 3.0±0.2).

2.1.4. Plasticizer

CARBOWAX™ (polyethylene glycol-M_w 400 g·mol^{-1}) supplied by Dow Chemical Company (Chile) was used as a conventional plasticizer. Technical specifications are described as follow: density: 1.13 g·cm^{-3}, viscosity (100 °C): 7.3 mPa·s, average number of repeating oxyethylene units (n): 8.7.

2.2. Blends formulation

Blends based on PLA were prepared at 170 °C for 15 min in a torque rheometer (Brabender 50 EHT, Germany). Binary blends were prepared in order to understand the effect of components on physicochemical properties (Table 1). Ternary blends were formulated with modified and unmodified polyflavonoids (10, 20, 30 wt%), as well as PEG.

2.3. Preparation of the blends

Solid components (PLA, PRI, and PRI-3) were pretreated by oven-drying at 60 °C for 72 h to eliminate possible absorbed water on the surface of the particles. In a specific order components were added in a rheometer. PLA and polyflavonoids were mixed for 2 min in a mixer (mini SWJB Lab mixing equipment, China), and loaded into the chamber (time mixing, t_{mix}: 0). In ternary blends, PEG was loaded after the PLA-melting (t_{mix}: 1.5 min). Three blends of each formulation were prepared.

2.3.1. Cold-blend processing

Blends were ground in an electric mill (IKA, Basic MF10, China) and 30 g charges were compression moulded on a LabTech LP20-B press (T: 175 °C, t: 5 min, p: 32 bar). Laminates of 100 mm^2 (thickness: 1.5 mm) were used for the flexural, and microscopy testing.

2.4. Physicochemical properties

2.4.1. Rheology

Rheology measurements were carried out in a torque rheometer with roller blades. The rotor speed was 50 rpm, and the free volume of the chamber was 20% of the total volume.

2.4.2. Confocal microscopy (particle size distribution)

Particle morphology of the blends was assessed by confocal fluorescence microscopy.

The fluorescense emission pattern of polyflavonoids (powder), and blends (laminate) were assessed by a systematic analysis. Dry samples were irradiated (Laser I: $\lambda_{405\ nm}$, Laser II: λ_{488nm}, and Laser III: $\lambda_{561\ nm}$), and fluorescence emission recovered. A Zeiss LSM 780 confocal microscope with several diode laser and a Coherent Chameleon laser (Ti:sapphire) for one-photon, was used in the experiments. Samples were

Table 1. Composition of PLA-based blends prepared at 170 °C

Blend	Component [wt%]				Code
	PLA	PRI	PRI-3	PEG	
PLA/PRI	80	20	0	0	PLA_{80}/PRI_{20}
	70	30	0	0	PLA_{70}/PRI_{30}
	60	40	0	0	PLA_{60}/PRI_{40}
PLA/PRI-3	80	0	20	0	$PLA_{80}/PRI\text{-}3_{20}$
	70	0	30	0	$PLA_{70}/PRI\text{-}3_{30}$
	60	0	40	0	$PLA_{60}/PRI\text{-}3_{40}$
PLA/PEG	80	0	0	20	PLA_{80}/PEG_{20}
	70	0	0	30	PLA_{70}/PEG_{30}
	60	0	0	40	PLA_{60}/PEG_{40}
PLA/PRI/PEG	60	10	0	30	$PLA_{60}/PRI_{10}/PEG_{30}$
	60	20	0	20	$PLA_{60}/PRI_{20}/PEG_{20}$
	60	30	0	10	$PLA_{60}/PRI_{30}/PEG_{10}$
PLA/PRI-3/PEG	60	0	10	30	$PLA_{60}/PRI\text{-}3_{10}/PEG_{30}$
	60	0	20	20	$PLA_{60}/PRI\text{-}3_{20}/PEG_{20}$
	60	0	30	10	$PLA_{60}/PRI\text{-}3_{30}/PEG_{10}$

PLA: poly-lactic acid, PRI: unmodified radiada pine polyflavonoid, PRI-3: hydroxypropyl radiata pine polyflavonoid (DS: 3), PEG: polyethylene glycol

observed with a C-Apochromat objective lens (63×, numerical aperture 1.2) in the opposite side of the cover slip. The images were obtained by the average of two scans. In all experiments, at least three sites of the blend were studied, and no appreciable variation was observed in the fluorescence properties among or within-sample. Considering the numerical aperture and the wavelength of excitation, the spatial resolution was approximately 200 nm. The optical zoom was 63×. A further digital zoom was used. The percentages of the lasers nominal powers were 1.2% (~20 μW) for a 20× objective.

Image-analysis of the maximum intensity projection was used in order to estimate the polyflavonoid particle size distribution as a referential parameter of component miscibility. IMARIS software (version 7.5.2, module Pro program) allowed estimating various types of numerical values based on the three-dimensional structures in confocal images.

Volume calculation of polyflavonoid particles was carried out using an automatic segmentation tool (Spots). The following parameters were considered: (1) different sizes, (2) estimated diameter, (3) quality above automatic threshold, (4) region growing -absolute intensity threshold with 7000 (for red channel) and 7500 (for green channel)-, and (5) diameter from volume. The segmented particles volume values of each image were plotted in a normalized histogram (in logarithmic scale). A range of relationship between volume, and volume sum of particles corresponding to this range was performed. Three replicates were averaged in order to define particle size distribution trends.

2.4.3. Molecular weight (M_w) distribution

Molecular weight distribution of the PLA after processing was acquired by size exclusion chromatography (SEC). Neat-PLA, processed-PLA and powdered blends (1 g) were dissolved in 70 mL of chloroform at room temperature (20–22 °C) during 7 days under stirring. The resulting suspension was centrifuged for 5 min at 4000 rpm, and an aliquot (50 μL) was analyzed using isocratic chloroform-eluted at 22 °C. Instrument (GPC Shimadzu, Japan) was equipped with DAD, and RID detectors. Polystyrene-divinylbenzene standards (Phenogel®) were used for calibration.

2.4.4. Thermal properties

Differential scanning calorimetry (DSC)

DSC analysis was performed on a NETZSCH DSC instrument (204 F1 Phoenix, Germany). Samples (7±3 mg) were sealed in high pressure steel pans; at a cooling rate of 10 °C·min^{-1}, and heated from 50 to 160 °C at 20 °C·min^{-1} heating rate under N_2 atmosphere, flow rate 20 mL·min^{-1}. The sample was then cooled back to 50 °C at 10 °C·min^{-1}, and heated again from 50 to 250 °C at 20 °C·min^{-1}. The glass transition temperature (T_g) of the blends was taken as the mid-point in the C_p step on the 2nd run associated at the second order thermal transition.

Thermal stability

Thermal stability was carried out using thermogravimetric analysis (TGA) performed on a NETZSCH TGA instrument (TG 209 F3 Tarsus, Germany). Samples of 6±2 mg was heated at 10 °C·min^{-1} from 25 to 600 °C under N_2 atmosphere, flow rate 20 mL·min^{-1}. The degradation temperature (T_d) was determined from the temperature peak obtained in the 1st derivative curve. The $T_{5\%}$ (5% of mass loss) was determined based on the TGA thermogram.

2.5. Flexural testing

Pressed laminated samples were cut with a die (gage length 60 mm, width 1.5±0.2 mm) and kept in a climate chamber oven overnight (T: 23±1 °C, p: 1.0 atm, relative humidity: 50±3%), and the Young's modulus (E) were determined [15]. Universal tensile testing machine (SmarTens 005, KARG Industrietechnik, Germany) was used employing a crosshead speed of 10 mm·min^{-1}. Eight laminate samples for each treatment were used for the flexural test analysis.

3. Results and Discussion

3.1. Evaluation of processability by torque rheometer

Selected torque-rheometer plots as a function of time at 50 rpm is provided (Figure 2).

Modified (PRI-3), and unmodified polyflavonoids (PRI) reduced the PLA-softening point. The decreasing of the torque on PRI-based blends associated to the PLA-softening point was clear, and it can be observed around 1.5 min. Modified polyflavonoid favors the earliest PLA-softening point (t_{mix}: 0.8 min) re-

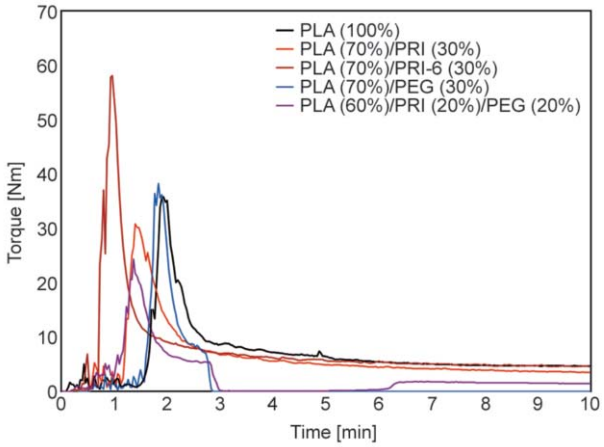

Figure 2. Rheological behaviour of neat PLA, and selected PLA-based blends prepared at mixture temperature of 170 °C (t_{mix}: 15 min)

gardless blend-composition. The dramatic influence of polyflavonoids on the PLA behavior is unexpected. However, the structure of polyphenol in terms of aromatic-content might be affecting the heat-transfer process during the mixing. In addition, the low heat-capacity of aromatic compounds in binary and ternary thermodinamical systems is a well-known issue [16]. However, the apparent low heat-capacity of polyflavonoids is not enough reason for the remarkable shifting of the PLA-softening point. Chemical interaction between PLA-chain and modified polyflavonoids grafting moieties apparently affects PLA-thermal behavior. In fact, is important to bring the homogenization times to a minimum. However, modified polyflavonoid reduced the mixing-time significantly at the expense of the higher torque values (torque: 40–80 Nm). In contrast, unmodified polyflavonoids reduced slightly the torque in comparison to the neat PLA (Figure 3).

Blends prepared with modified polyflavonoid (PRI-3) induced the higher torque values. The high aliphatic OH-content of polyflavonoid derivatives in comparison to the lower ones of neat polyflavonoids apparently increases the viscosity during the melting, and in consequence the resistance to the rheometer blades. The differences in torque values can be explained considering that the viscoelastic properties of polyflavonoids dramatically change upon hydroxypropylation [9–11]. Is well-known that the aliphatic –OH functionalities enhance hydrogen-bridge interaction between polymer chains. In addition, strong association between linear aliphatic PLA's chain, and the hydroxypropyl grafting from the derivatives during blending might be also considered.

On the other hand, low interaction between neat polyflavonoids and PLA-chains can be explained in terms of the high differences in polarity of the two biopolymers [10, 17]. However, molecular association between PLA and polyflavonoids in the molten-state has not been documented before.

3.2. Molecular weight distribution

A dramatic effect of the blend-composition, and the processing strategy on the PLA-M_w was observed (Figure 4).

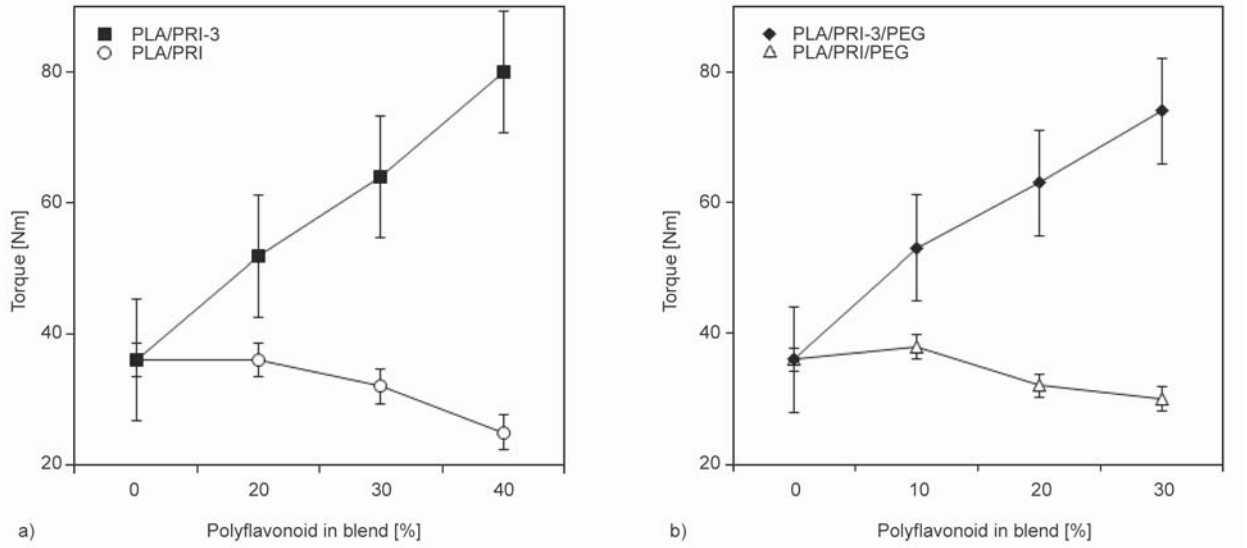

Figure 3. Maximal torque associated to the PLA-melting in function of the polyflavonoid-content for PLA-based blends prepared at 170 °C (t_{mix}: 15 min). (a) binary blends (PLA/PRI, and PLA/PRI-3). (b) ternary blends (PLA/PRI/PEG, and PLA/PRI-3/PEG). $N = 3$. Note: data illustrate the torque variation during the first two minutes of mixing.

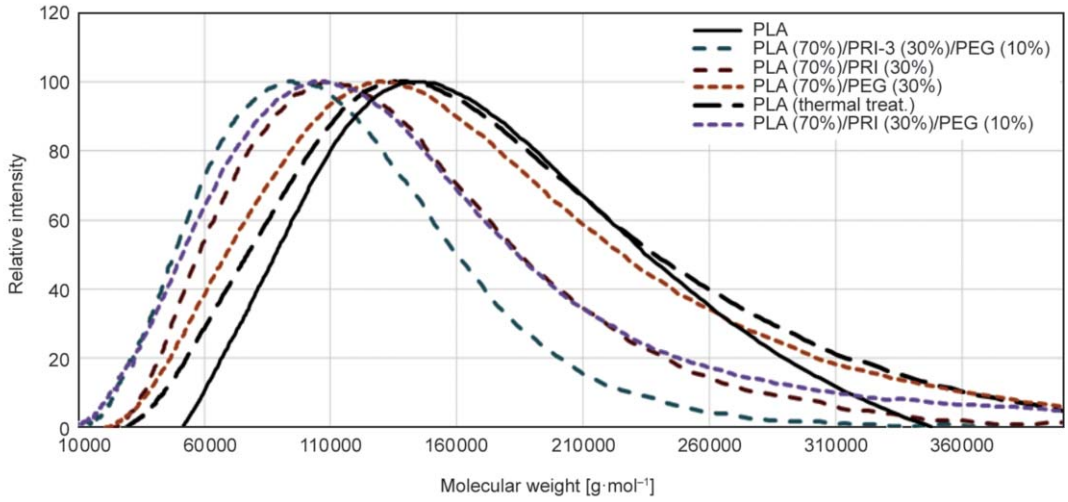

Figure 4. Selected GPC-traces of PLA from PLA-based blends illustrating changes of the molecular weight distribution. Thermal treatment:170 °C, 15 min.

PEG as a blend-components affected sligtly the M_{wPLA}. However, degradation of PLA in polyflavonoid-based binary blends was the highest regardless the polyflavonoid-type. The degradation mechanisms of PLA-based materials have been well-described [1, 17, 18]. In fact, several components on blends have been recognized as degradation promoters of PLA-degradation [22–26]. M_{wPLA} decreased in ca 40 000 g·mol^{-1} suggesting random cleavages on the polymer chains apparently by the effect of the polyflavonoid acidity (natural pH: 3.0–4.5). However, 15 minutes of PLA-proccesing on the rheometer (T: 170 °C) also affects the M_{wPLA} from $15.4 \cdot 10^4$ to $13.8 \cdot 10^4$ g·mol^{-1}.

Unmodified polyflavonoids had the biggest influence in PLA-degradation (Figure 5a). The results highlight the influence of polyphenols as the main source of PLA-degradation.

On the other hand, increased D as (dispersity) a function of the polyflavonoid-content can be interpreted as a greater diversity of degraded polymer-chains during the blending [11].

It is worth noticing that the modified polyflavonoids (PRI-3) had a minor effect on polydispersity even at the highest derivatives-charge (Figure 5b). Apparently the replacement of the acidic hydroxyl groups (–OH, *pKa*: 9–10) by the hydroxypropyl chain (–OH, *pKa*: 13–16) decreases the detrimental effect of polyflavonoids on PLA-degradation during processing.

The remarkable influence of polyflavonoids on the M_{wPLA} can be used as an advantage for PLA/polyflavonoid blend formulation, considering that the

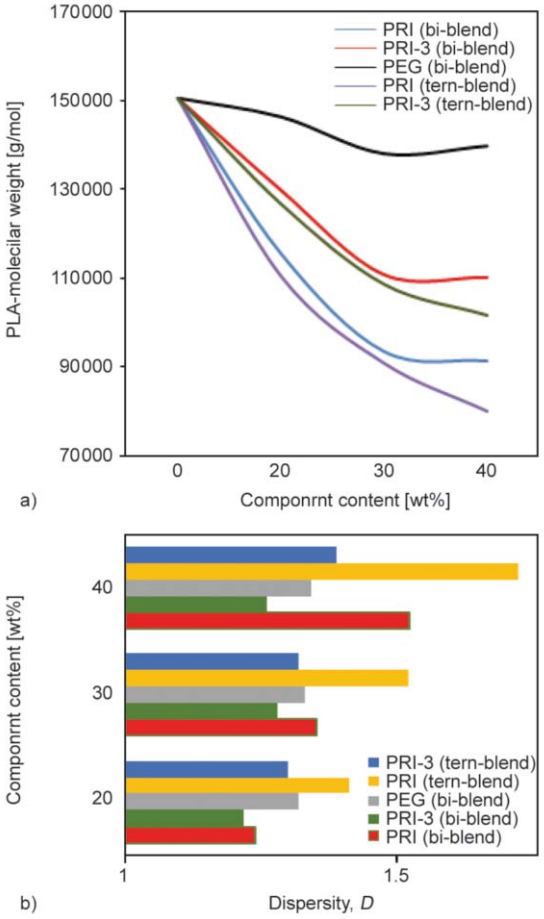

Figure 5. Molecular weight features of PLA-based blends prepared at 170 °C (t_{mix}: 15 min). (a) Molecular weight distribution in function of the component-content, (b) dispersity values (D) in function of the blend-type. $N = 3$.

biodegradability and disintegration of PLA, and PLA-based materials are strongly associated to the M_w of

the polymer-matrix, the crystallinity degree, and the chemical lability of selected functional groups [18]. That is why polyflavonoids can be used for tailoring PLA's molecular properties. In addition, polyflavonoids also might be advantageous as functional additives for several biopolymers such as starch, cellulose, and commercial biodegradable aliphatic copolymers (Ecoflex® and Ecovio®) [3, 24, 26].

3.3. Morphology

3.3.1. Confocal fluorescence microscopy (spectrum pattern)

Confocal fluorescence microscopy is an extremely useful tool enabling polyphenols quantification [19]. The strong fluorescence pattern of polyflavonoids can be used to estimate particle size and particle shape, considering the fact that polyflavonoid-derived composites have a typical dark appearance.

Considering that polyflavonoid blends are colored composites (image not-shown), the evaluation of fluorescence emission pattern was performed considering that PLA, and PEG are not-active fluorescent molecules. Such features were utilized in order to study the morphological features of PLA-based blends [11, 20].

The emission spectra of PRI and PRI-3 were assessed by the three types of lasers (λ_I: 405 nm, λ_{II}: 488 nm, λ_{III}: 561 nm). Chemical modification has a negligible influence on the emission pattern (Figure 6a). Results allowed concluding that fluorescence measurements are not affected significantly by hydroxypropylation. Apparently, the structural variations upon derivatization do not affect the energy emission pattern.

Based on such findings, fluorescence emission pattern of binary and ternary PLA-based blends was assessed by two lasers (λ_I and λ_{III}) covering the entire range of wavelength. As expected, marginal differences regarding emission pattern in function of blend-composition were observed (Figure 6b).

Regardless blend-composition, maximal fluorescence emission (λ_I) oscillated between 480 and 520 nm, while Laser III (λ: 561 nm) induces an emission pattern in a narrow range of wavelength (600–630 nm). That is why red light was used in order to assess the morphological features of the blends.

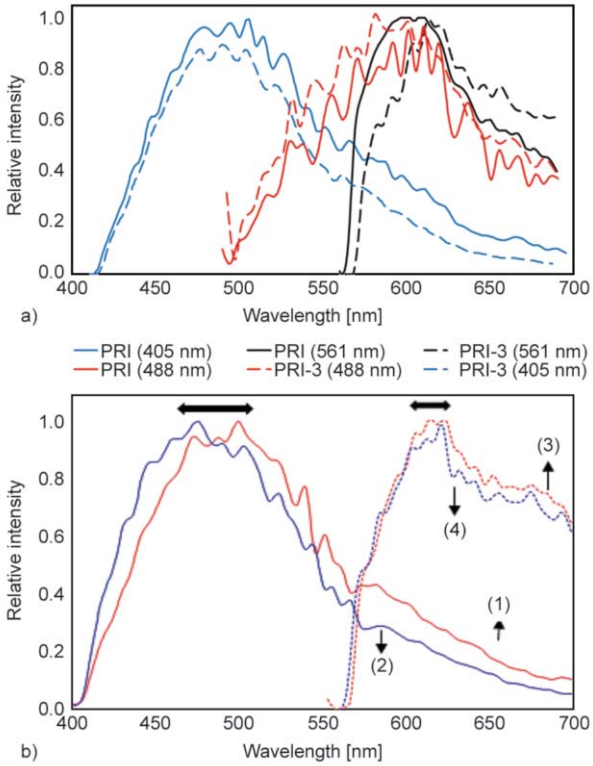

Figure 6. Fluorescense emission features of polyflavonoids, and polyflavonoids-based blends prepared at 170 °C (t_{mix}: 15 min). (a) emission spectra of modified (PRI-3), and unmodified (PRI) polyflavonoids, (b) emission spectra of PLA-based blends, (1) PLA_{70}/PRI_{30} (Laser λ_I: 405 nm), (2) PLA_{70}/PRI_{30} (Laser λ_{II}: 561 nm), (3) $PLA_{60}/PRI\text{-}3_{20}/PEG_{20}$ (Laser λ_I: 405 nm), and (4) $PLA_{60}/PRI\text{-}3_{20}/PEG_{20}$ (Laser λ_{II}: 561 nm).

3.3.2. Particle size distribution (image-processing)

Maximal intensity projection of selected PLA-based blends is shown (Figure 7).

Image-processing revealed remarkable differences in morphology of polyflavonoid particles dispersed on the PLA-matrix (*N*). The methodology allowed a high count of particles. Particle volumes were determined on the basis of a selective channel (red, λ_{III}: 561 nm). PRI-3-based blends exhibited the smallest particles volume, which describes the better miscibility of polyflavonoid derivatives (Figure 8a), whereas the particle size of PRI, and PRI-3 were rather similar (see Figure 8b).

However, PRI particles volume was the biggest in ternary blends. Apparently, certain interaction between polyflavonoids and PEG affects significantly the con-

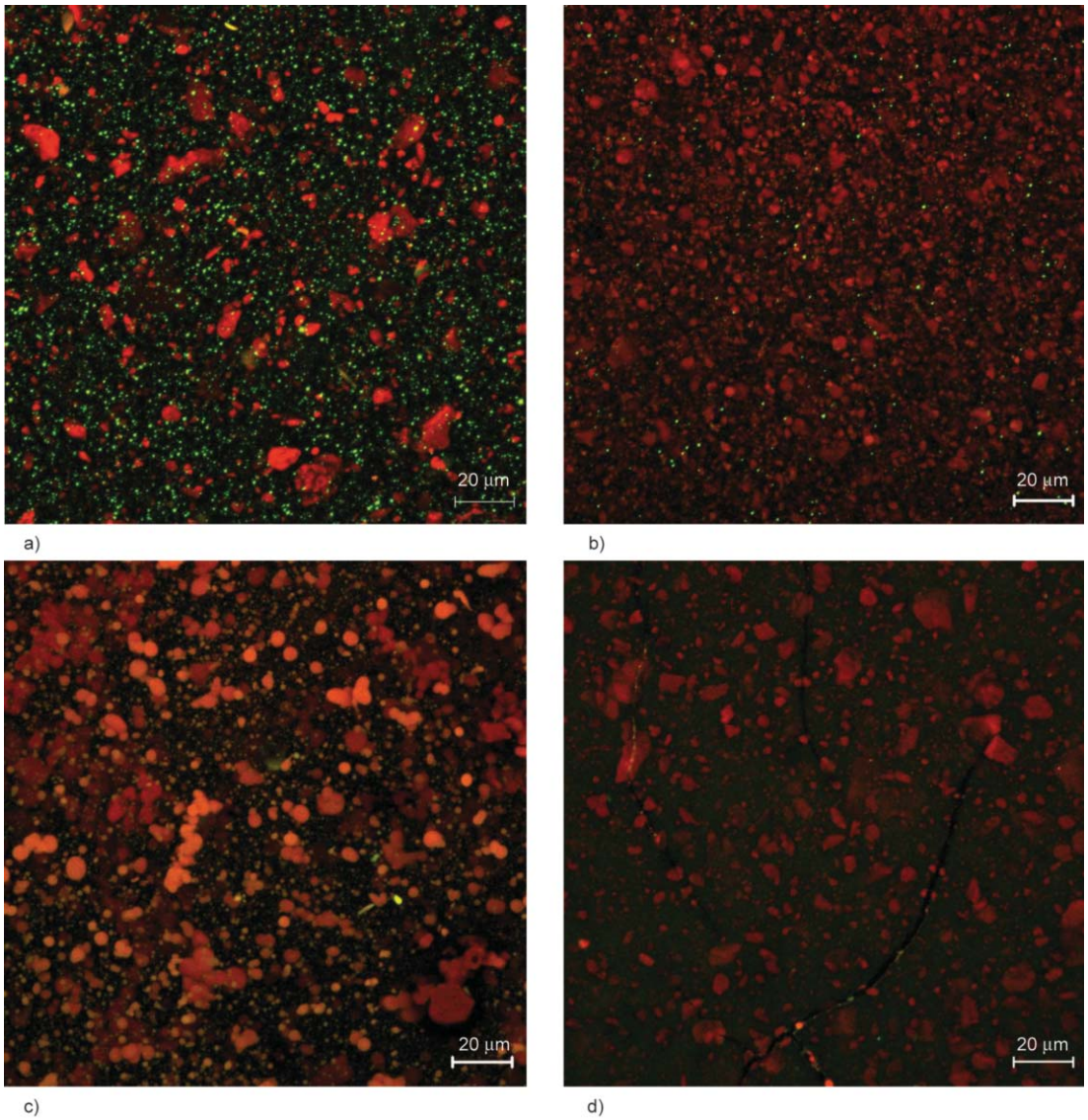

Figure 7. Maximum intensity projection of selected PLA-based blends prepared at 170 °C (t_{mix}: 15 min). (a) PLA_{70}/PRI_{30}, (b) $PLA_{70}/PRI\text{-}3_{30}$, (c) $PLA_{60}/PRI_{20}/PEG_{20}$, (d) $PLA_{60}/PRI\text{-}3_{20}/PEG_{20}$.

formational features during the blending. The result matches with the spherical particle morphology clearly visible on the maximum intensity projection image (see Figure 7c). In fact, is well-known that PEG interacts strongly with polyflavonoids via hydrophobic domains [11, 21]. The H–H interaction enables an open-conformation of the polyflavonoid molecules, so increasing volumen was apparently associated to molecular complexation during the melt-blending.

Normalized histogram (Figure 8) shows that polyflavonoid chemical modification enhances the miscibility on the PLA-matrix regardless the blend-type. On the other hand, unmodified polyflavonoids show similar particle volume distribution to the referential PRI volume (see Figure 8b). Limited solubility of polyphenols on the PLA-matrix can be explained considering the high difference in polarity between PRI, and PLA.

As described previously by image-processing, PEG affects dramatically the polyflavonoid particle volume.

The low polarity of PRI-3 is a key factor to understand the better compatibility features of modified polyflavonoids on the PLA-matrix. Maximum interaction between the hydroxypropyl moieties with the PLA-chain, and PEG during the mixing highlights that the chemical modification is a feasible strategy in using polyflavonoids in bioplastics.

In addition, it worth to highlight that confocal microscopy (fluorescense emission) coupling to image-

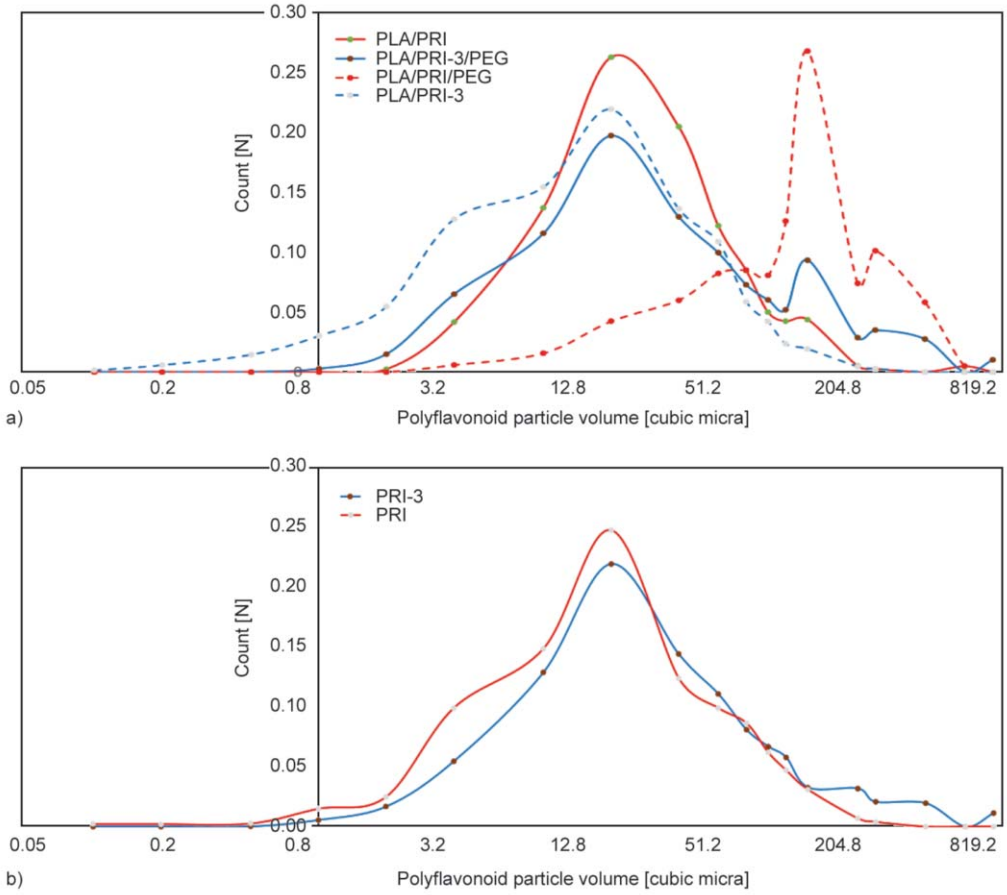

Figure 8. Normalized polyflavonoids particle volume of PLA-based blends assessed by emission fluorescence microscopy. (a) Polyflavonoids particle volumen (reference), (b) polyflavonoids particle volumen in blends (binary blend: $PLA_{70\%}$, ternary blends: $PLA_{60\%}/PEG_{10\%}$). Note: polyflavonoid particles volume is expressed in logarithmic scale.

processing is a usefull technique in estimating the morphological parameters of PLA biopolymer blended with natural polyflavonoids.

3.4. Thermal properties

3.4.1. DSC analysis

Selected thermograms illustrate the T_g, and T_m of the neat PLA, and PLA-based blends (Figure 9). It is evident that neat PLA has a T_g of 60 °C, and T_m of 170 °C. In binary blends polyflavonoids did not significantly influence the $T_{g_{PLA}}$ value. However, such polyphenols induce the PLA-crystallization (T_c: 100 °C) to a high extent. The nucleating effect of polyflavonoids in PLA-based blends has been not well-clarified in previous works. Differences in polarity, hydroxyl-content, and conformational features are factors apparently affecting the PLA-crystallization behavior induced by polyflavonoids.

On the other hand, PEG induces a reduction of $T_{g_{PLA}}$ (55.6 °C), as well as the $T_{c_{PLA}}$. The synergetic effect of PEG on the PLA-thermal properties has been previously reported, as well as on the crystallization behavior [22–26]. The remarkable effect on thermal properties can be explained considering that PEG favors the breaking of intermolecular hydrogen bridges of PLA during processing, prone to an early melting, and a significant T_g reduction.

In addition, Figure 9b, 9c shows in detail the thermal behavior of all tested blends according to the component-loading. Polyflavonoid induces a significant $T_{m_{PLA}}$ and $T_{c_{PLA}}$ reduction in ternary blends. However, the variation of T_g, T_c, and T_m in binary blends was negligible. In contrast, PEG significantly affects the $T_{g_{PLA}}$, $T_{m_{PLA}}$ and $T_{c_{PLA}}$ values.

It is worth noticing that the depression of the $T_{g_{PLA}}$, and $T_{c_{PLA}}$ was remarkable in PRI-3-based blends. The results describe the advantageous effect of the chemical modification on the miscibility features.

Apparently, polyflavonoids act as an effective nucleating agent in PLA-based blends. The PLA-crystallization during the blend-cooling has an important impact on the mechanical properties. Several salts

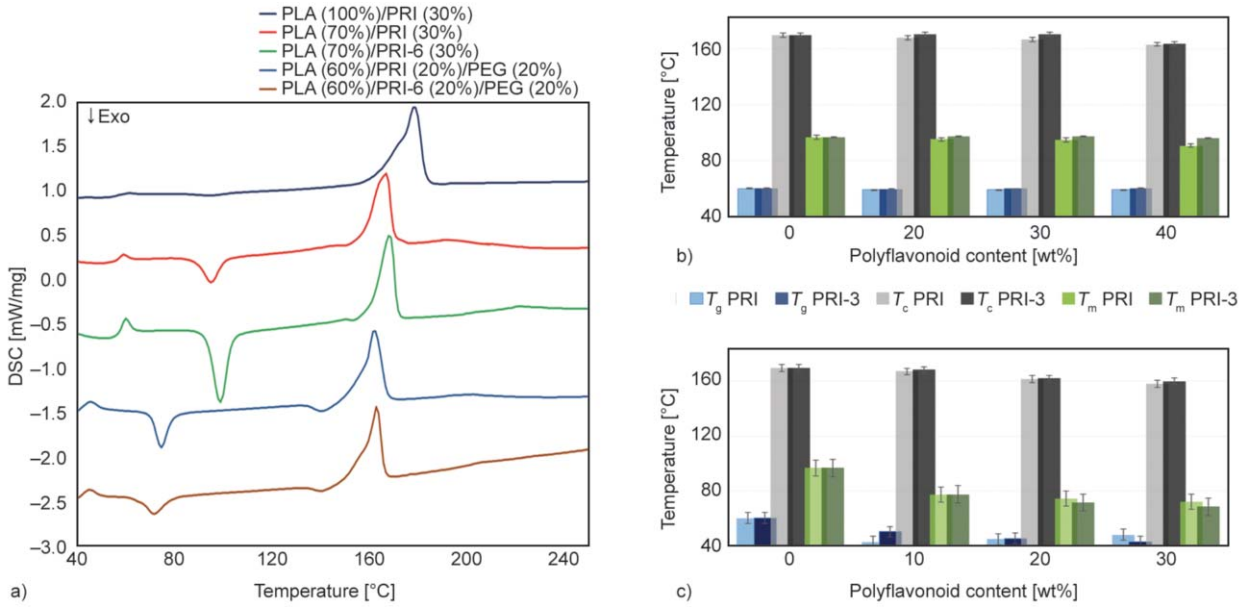

Figure 9. Thermal behavior (DSC) of PLA-based blends prepared at 170 °C (t_{mix}: 15 min) considering the second heating. (a) Selected DSC-traces, (b) transitional temperatures in function of polyflavonoid-content (binary blends), (c) transitional temperatures in function of polyflavonoid-content (ternary blends). $N = 3$.

(talcs), organic compounds (amines), fibers, nanotubes, and commercial nucleating (3801X, and LAK) have been reported as nucleating agent in PLA-based blends [23, 24]. However, to our knowledge it is the first time that polyphenols from pine bark are reported as nucleating agents in PLA-matrix in a wide range of composition.

The synergic effect between PEG and polyflavonoids on the PLA thermal behavior (T_g, T_c, T_m) has been also reported in several systems [25, 26]. The similarities regarding functional groups of PEG and PLA apparently favor the mobility of the chain and breaks the intermolecular hydrogen bonds which reduce transitional temperatures.

Since the T_g value is an excellent indicator of chain mobility, plasticizing efficiency has therefore been evaluated by measuring the T_g shifting as a function of plasticizer concentration. All the binary blends show only one T_g in the DSC-thermogram indicating an apparent good miscibility between PLA, PRI-3, and PEG. The decrease of T_g highlights the effect of the plasticizer in PLA compositions with increasing molecular mobility. The plasticizing effect is confirmed by the modification of T_g which is significantly decreased by comparison to the neat PLA matrix (T_g: ~60 ºC).

3.4.2. TGA analysis

The selected thermograms showed that a significant change to the degradation temperatures according to the blend-composition was observed (Figure 10). The T_d values were above 300 ºC. However, a remarkable effect of components on the $T_{5\%}$, and T_d of ternary blends was noticed.

Thermal behavior of binary and ternary-blends reveals a significant effect of the polyflavonoids-content (Figure 10).

Neat polymers (PLA, PEG), exhibited a single decomposition peak, indicating that they degraded mainly in one step (data not-shown). Polyflavonoid-content affects the $T_{5\%}$, and T_d significantly. The results can be explained considering that polyphenols are thermally unstable building-blocks, prone to yield carbonaceous residues as a consequence of pyrolytic processes [9, 11].

PRI-3-based ternary blends show the lowest T_d. The result is unexpected considering the high thermal stability of PRI-3 in comparison to unmodified bark polyflavonoids described in previous reports [11]. However, polyflavonoid's DS cannot be considered as the unique factor affecting thermal decomposition of the blends. The substitution pattern on the C_{15} polyflavonoid unit (see Figure 1) seems to be a key factor

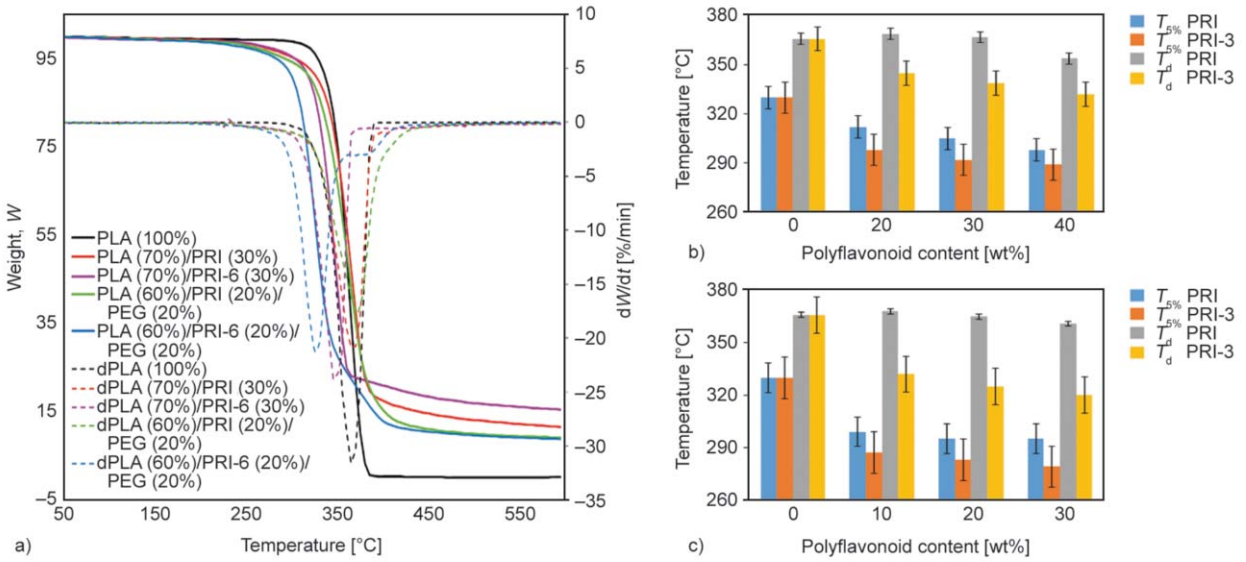

Figure 10. Thermal behavior (TGA) of PLA-based blends prepared at 170 °C (t_{mix}: 15 min). (a) Selected TGA-traces, (b) decomposition temperatures in function of polyflavonoid-content (binary blends), (c) decomposition temperatures in function of polyflavonoid-content (ternary blends). $N = 3$.

for polyphenols degradation [8, 9]. The low M_w distribution of the water-insoluble tannin fraction (PRI), as well as the lipophilic character of such polyflavonoids as a consequence of concomitants apparently affects the thermal stability of the blends in a differentiated manner.

On the other hand, all PLA-blends showed significant residues at 600 °C (<20%). Residual weight increased with increasing polyflavonoid-content, excepting in PLA-based ternary blends (Figure 11).

The results point out that the polyflavonoid-based pyrolytic residues are significant products during the blend decomposition. However, a strong interaction between PEG, and polyflavonoids on the residual weight was evidenced. Apparently, polyphenol-PEG complexation favored the volatilization rate at high temperatures (>400 °C).

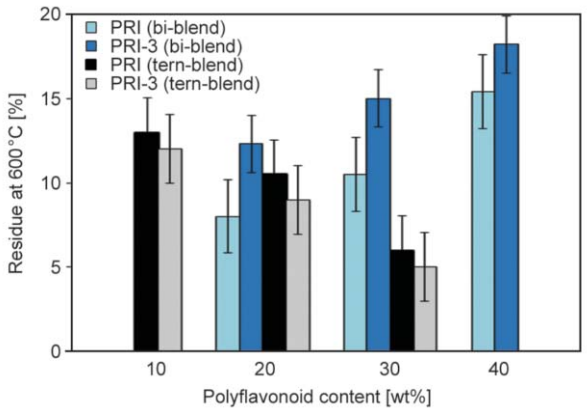

Figure 11. Residual weight at 600 °C of binary-, and ternary-blends prepared at 170 °C (t_{mix}: 15 min). $N = 3$.

3.5. Flexural testing

PLA-based blends exhibited a typical stress-strain curve which describes that the samples breaks before yielding (Figure 12). Curve morphology was affected by the blend-composition.

The flexural behaviour of the neat PLA showed characteristics of glassy polymers with low deformation at break. In contrast, PLA-based blends showed a different behaviour (Table 2).

In general, PLA/PRI blends show poor performance in term of Young's modulus (E). In contrast, the highest PRI-3-charge the highest E-values. The behavior can be explained by incompatibility between the neat polyflavonoids, and the PLA polymer due to the difference in polarity, and molecular features.

In addition, the E-modulus value dropped dramatically from 88 to 22 MPa with incorporation of PRI (10 wt%); indicating incompatibility. In contrast, E-modulus was improved in 15 MPa when PRI-3 was loaded from 10 to 30 wt%. This can be explained by the role of hydroxypropyl-chain which apparently acts as a compatibilizer moiety in binary-, and ternary-blends.

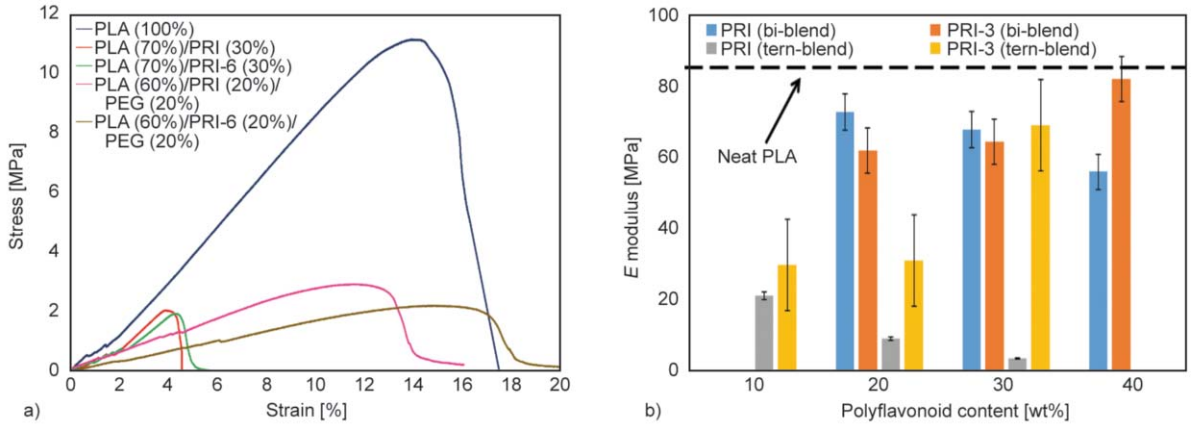

Figure 12. Mechanical performance of PLA-based blends prepared at 170 °C (t_{mix}: 15 min). (a) Selected stress-strain curves, (b) *E*-modulus in function of the polyflavonoid content. $N = 8$.

Table 2. Mechanical performance of PLA-based blends prepared at 170 °C for 15 min

Blend	F_m [N]	σ_{fM} [MPa]	ε_{fM} [%]
PLA	37.5±5	2.70±1.0	16.6±5.0
PLA_{80}/PRI_{20}	18.1±3	0.30±0.01	6.1±0.1
PLA_{70}/PRI_{30}	12.4±2	0.15±0.01	4.5±0.3
PLA_{60}/PRI_{40}	7.2±1	0.11±0.01	2.12±0.1
$PLA_{80}/PRI\text{-}3_{20}$	13.6±5	1.82±0.21	4.13±0.5
$PLA_{70}/PRI\text{-}3_{30}$	10.0±2	1.88±0.30	4.23±0.4
$PLA_{60}/PRI\text{-}3_{40}$	2.0±1	1.62±0.41	1.12±0.1
$PLA_{60}/PRI_{10}/PEG_{30}$	11.3±2	0.46±0.33	14.7±0.9
$PLA_{60}/PRI_{20}/PEG_{20}$	10.6±2	0.19±0.02	12.8±0.9
$PLA_{60}/PRI_{30}/PEG_{10}$	9.6±1	0.09±0.01	11.6±0.7
$PLA_{60}/PRI\text{-}3_{10}/PEG_{30}$	8.0±1	0.21±0.02	12.4±0.9
$PLA_{60}/PRI\text{-}3_{20}/PEG_{20}$	10.4±2	0.25±0.02	10.87±0.6
$PLA_{60}/PRI\text{-}3_{30}/PEG_{10}$	15.0±3	0.46±0.03	14.4±0.3

Average±standard deviation, F_m: maximum force, σ_{fM}: flexural strength, ε_{fM}: flexural strain. $N = 8$.

4. Conclusions

PLA-based blends have been successfully prepared with *P. radiata* bark polyflavonoids, by melt-blending at 170 ºC during 15 min. This compounding strategy is easy and potentially commercially viable for PLA applications beyond the food-packaging.

Modification of radiata pine polyflavonoids is a valuable alternative in order to improve the performance of such building-blocks in binary-, and ternary-blends. Chemical structure of the polyflavonoid's grafting influences: (1) the blend processability, (2) the component miscibility, (3) the PLA's melting-, and crystallization-processes, (4) the thermal resistance, and (5) the flexural performance.

Rheological behavior of PLA-based blends is dramatically affected by the type-, and component-composition. Considering the torque-rheometer data modified, and unmodified radiata pine polyflavonoids improved the processability of PLA in term of a short-mixing.

The image-processing using confocal fluorescence microscopy was successfully utilized in order to estimate the particle volume as an indicator of polyflavonoid's miscibility. The modified polyphenols showed higher compatibility features as a consequence of the dramatic reduction of the particle volume.

Polyflavonoid induces PLA-crystallization in a high extent. The synergetic effect of PEG with polyflavonoids is related to the chemical similarity of the polymer chains enhanced upon grafting (hydroxypropyl-chain). The result is highly relevant in view of polyflavonoid-based composites preparation.

Modified polyphenol decreases slightly the thermal stability of the blends below 300 °C. Such drawback is negligible considering that the PLA-processing temperature is around 170 °C.

On the other hand, the tannin acidity affects the PLA molecular weight distribution which influences the flexural performance. Also the thermal processing of the neat PLA affects the M_w of the polymer.

The increasing of the *E*-modulus of the blends as effect of a good mixing of polyflavonoids derivatives on the PLA-matrix was achieved.

P. radiata bark polyflavonoids might be used for PLA-based blends formulations in view of novel envisaged applications. Polyflavonoid-based composites seem to play a key role in polymer engineering in a near future.

Acknowledgements

D.E. García thanks to the International PhD. Student Exchange Program from Technological Development Unit (UDT), Concepción University, Chile (Basal Project: PFB-27). D.E. García would like to acknowledge to the 'Comisión Nacional de Investigación Científica y Tecnológica CONICYT, Chile' (FONDECYT Project: 11150056) for the financial support. We would also like to show our gratitude to Mrs. Corina Silva, Mrs. Carmen Pradenas, and Mrs. Yohana Sanzana, for their technical assistance. In addition, authors also like to thanks to MSc. Joanna Tereszczuk, and Germán Osorio (Advance Microscopy Center, CMA), from Concepción University, Chile, for the technical assistance regarding confocal microscopy, and image-processing, respectively.

References

[1] James L.: Large-scale production, properties and commercial applications of polylactic acid polymers. Polymer Degradation and Stability, **59**, 145–152 (1998). DOI: 10.1016/S0141-3910(97)00148-1

[2] Cartier L., Okihara T., Ikada Y., Tsuji H., Puiggali J., Lotz B.: Epitaxial crystallization and crystalline polymorphism of polylactides. Polymer, **41**, 8909–8919 (2000). DOI: 10.1016/S0032-3861(00)00234-2

[3] Frone A. N., Berlioz S., Chailan J-F., Panaitescu D. M.: Morphology and thermal properties of PLA–cellulose nanofibers composites. Carbohydrate Polymers, **91**, 377–384 (2003). DOI: 10.1016/j.carbpol.2012.08.054

[4] Grigsby W. J., Kadla J. F.: Evaluating poly(lactic acid) fiber reinforcement with modified tannins. Macromolecular Materials and Engineering, **299**, 368–378 (2014). DOI: 10.1002/mame.201300174

[5] Eisenberg P.: Biocomposites from microfibrillated cellulose and biodegradable polymers (PLA) (in Spanish). in '3er Congreso Iberoamericano sobre Biorrefinerías (CIAB), 4to Congreso Latinoamericano sobre Biorrefinerías y 2do Simposio Internacional sobre Materiales Lignocelulósicos, Concepción, Chile' 108–109 (2015).

[6] Case F. H., Honeycutt J. D.: Will my polymer mix? Methods for studying polymer miscibility. Trends in Polymer Science, **2**, 256–267 (1994).

[7] Anwer M. A. S., Naguib H. E., Celzard A., Fierro V.: Comparison of the thermal, dynamic mechanical and morphological properties of PLA-lignin & PLA-polyflavonoid particulate green composites. Composites Part B: Engineering, **82**, 92–99 (2015). DOI: 10.1016/j.compositesb.2015.08.028

[8] García D. E., Glasser W. G., Pizzi A., Lacoste C, Laborie M-P.: Polyphenolic resins prepared with maritime pine bark tannin and bulky-aldehydes. Industrial Crops and Products, **62**, 84–93 (2014). DOI: 10.1016/j.indcrop.2014.08.010

[9] García D. E., Glasser W. G., Pizzi T. A., Osorio-Madrazo A., Laborie M-P.: Synthesis and physicochemical properties of hydroxypropyl tannins from maritime pine bark (*Pinus pinaster* Ait.). Holzforschung, **68**, 411–418 (2014). DOI: 10.1515/hf-2013-0145

[10] García D. E., Glasser W. G., Pizzi A., Paczkowski S., Laborie M-P.: Hydroxypropyl tannin from *Pinus pinaster* bark as polyol source in urethane chemistry. European Polymer Journal, **67**, 152–165 (2015). DOI: 10.1016/j.eurpolymj.2015.03.039

[11] García D. E.: *Pinus pinaster* (Ait.) bark polyflavonoid and its hydroxypropyl derivatives as building-blocks for bio-material design. PhD Thesis. Freiburg University (2014).

[12] Bocalandro C., Sanhueza V., Gómez-Caravaca A. M., González-Álvarez J., Fernández K., Roeckel M., Rodríguez-Estrada M. T.: Comparison of the composition of *Pinus radiata* bark extracts obtained at bench- and pilot-scales. Industrial Crops and Products, **38**, 21–26 (2012). DOI: 10.1016/j.indcrop.2012.01.001

[13] Jerez M., Selga A., Sineiro J., Torres J. L., Núñez M. J.: A comparison between bark extracts from *Pinus pinaster* and *Pinus radiata*: Antioxidant activity and procyanidin composition. Food Chemistry, **100**, 439–444 (2007). DOI: 10.1016/j.foodchem.2005.09.064

[14] Pizzi A.: Polyflavonoids: Major sources, properties and applications. in 'Monomers, polymers and composites from renewable resources' (eds.: Belgacem N., Gandini A.) Elsevier, Amsterdam 179–199 (2008).

[15] ISO 527-1 5B: Plastics – Determination of tensile properties – Part 2: Test conditions for moulding and extrusion plastics (2012).

[16] Rihani D. N., Doraiswamy L. K.: Estimation of heat capacity of organic compounds from group contributions. Industrial and Engineering Chemistry Fundamentals, **4**, 17–21 (1965). DOI: 10.1021/i160013a003

[17] Vert M., Schwarch G., Coudane J.: Present and future of PLA polymers. Journal of Macromolecular Science Part A: Pure and Applied Chemistry, **32**, 787–796 (1995). DOI: 10.1080/10601329508010289

[18] Tokiwa Y., Calabia B. P., Ugwu U., Aiba S.: Biodegradability of plastics. International Journal of Molecular Sciences, **10**, 3722–3742 (2009). DOI: 10.3390/ijms10093722

[19] Scogings P., Siko S., Taylor R.: Calibration of a handheld instrument for measuring condensed tannin concentration based on UV- and red-excited fluorescence. African Journal of Range and Forage Science, **31**, 55–58 (2014). DOI: 10.2989/10220119.2013.858772

[20] Grigsby W. J., Bridson J. H., Lomas C., Elliot J-A.: Esterification of condensed tannins and their impact on the properties of poly(lactic acid). Polymers, **5**, 344–360 (2013).
DOI: 10.3390/polym5020344

[21] Makkar H. P. S., Blümmel M., Becker K.: Formation of complexes between polyvinyl pyrrolidones or polyethylene glycols and tannins, and their implication in gas production and true digestibility in in vitro techniques. British Journal of Nutrition, **73**, 897–913 (1995).
DOI: 10.1079/BJN19950095

[22] Shi X., Zhang G., Vu Phuong T., Lazzeri A.: Synergistic effects of nucleating agents and plasticizers on the crystallization behavior of poly(lactic acid). Molecules, **20**, 1579–1593 (2015).
DOI: 10.3390/molecules20011579

[23] Li H., Huneault M. A.: Effect of nucleation and plasticization on the crystallization of poly(lactic acid). Polymer, **48**, 6855–6866 (2007).
DOI: 10.1016/j.polymer.2007.09.020

[24] Běhálek L., Maršálková M., Lenfeld P., Habr J., Bobek J., Seidl M.: Study of crystallization of polylactic acid composites and nanocomposites with natural fibres by DSC method. in 'Proceedings of NANOCON 2014, Brno, Czech Republic' p.6 (2013).

[25] Miyata T., Masuko T.: Crystallization behaviour of poly(L-lactide). Polymer, **39**, 5515–5521 (1998).
DOI: 10.1016/S0032-3861(97)10203-8

[26] Ke T., Sun X.: Melting behavior and crystallization kinetics of starch and poly(lactic acid) composites. Journal of Applied Polymer Science, **89**, 1203–1210 (2003).
DOI: 10.1002/app.12162

eXPRESS Polymer Letters Vol.10, No.10 (2016) 849–859
Available online at www.expresspolymlett.com
DOI: 10.3144/expresspolymlett.2016.79

Infrared welding of cross-linkable polyamide 66

C. Leisen, D. Drummer*

Friedrich-Alexander-Universität Erlangen-Nürnberg (FAU), Faculty of Engineering, Department of Mechanical Engineering, Institute of Polymer Technology, Am Weichselgarten 9, 91058 Erlangen, Germany

Received 23 February 2016; accepted in revised form 5 June 2016

Abstract. Radiation cross-linking of polyamide 66 with electron beams alters the material's characteristics. This leads to a varied relationship amongst the process, structure, and properties for infrared welding cross-linked polyamide 66. A three-dimensional network of covalent bonds results in an impeded melt flow and altered welding characteristics. Compared to non-cross linked polyamide, a changed energy input in the weld during infrared heating and a reduced meltdown can be observed. Such thermal developments and a reduced meltdown affect the resulting weld strengths. Welding factors of almost 60% of base material strengths can be achieved. A clear influence of the heating time on the weld strength can be observed. The scope of this article is to investigate the influence of radiation cross-linking on the material characteristics and, by extension, the resulting processing and welding characteristics. Mechanical and optical investigations serve to highlight the influence of radiation cross-linking on the infrared welding process of polyamide 66.

Keywords: *mechanical properties, cross-linking, polymer welding, infrared welding, polyamide 66*

1. Introduction

1.1. Radiation cross-linking of polyamide 66

Radiation cross-linking is a well-known and established technique for enhancing the properties of thermoplastic polymers. Typical radiation sources are gamma rays, electron beams and X-rays [1]. The radiation induced cross-links between the macromolecules lead to improved physical properties and allow a wide range of industrial applications like for example pipes and tubes, hip joint pans, foams, shrinking-fit products or automotive applications [1–3]. In 1952, Charlesby described the influence of radiation on the properties of polyethylene for the first time [4, 5]. Subsequent investigations extended the knowledge about radiation cross-linking and the possible material range [6].

The process of cross-linking can be divided into two main reactions. High-energy radiation transfers energy to the atoms and results in an ionization or excitation of the atoms during the primary reaction [1, 2]. Further reactions lead to the formation of radicals. These radicals enable cross-linking of the polymer in its amorphous region in a secondary reaction [1, 2]. Aside from the formation of covalent bonds, degradation, chain scission and oxidation can occur, possibly causing the material properties to deteriorate [1].

The resulting three dimensional covalent networks between the macromolecules results in an increase in the short-term temperature resistance and a rubbery-elastic behavior above the crystallite melting temperature, Figure 1 [7, 8]. These covalent bonds also influence the melting and crystallization behavior towards lower temperatures [1, 3, 8, 9]. Aside from polyethylene, other polymers, such as polyamide, can be cross-linked by high energy radiation [6]. In order to attain economical radiation exposure rates, cross-linking agents are needed. These polyfunctional monomers, e.g. triallyl isocyanurate (TAIC), allow a cross-linking at lower and economical radiation

*Corresponding author, e-mail: leisen@lkt.uni-erlangen.de

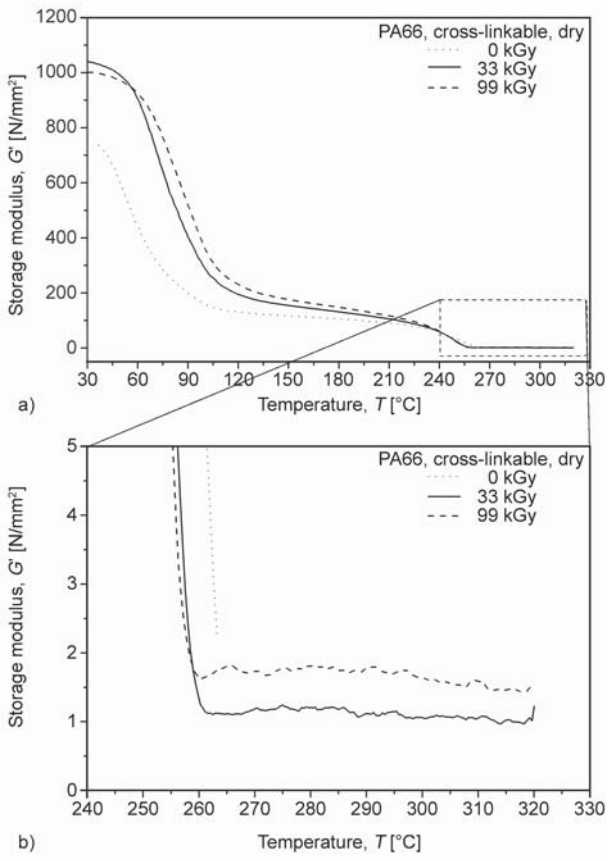

Figure 1. Residual stiffness of radiation cross–linkable, polyamide 66 (DMA) [7]: (a) complete temperature range, (b) within range of crystallite melting temperature

doses and temperatures [10–13]. Previous investigations into vibration welding of radiation cross-linked polyamide 66 have shown that cross-linking with its changed material properties leads to a varied relationship amongst the process, structure, and properties for vibration welding cross-linked polyamides [7, 14]. Especially processing time and temperature influence the material characteristics of cross-linked polyamide [14]. It was shown that during vibration welding the energy input and the resulting weld temperature in the weld zone differs between the selected material and process settings and exhibits an inconsistency with the time [7]. These inconsistencies make it difficult to analyze the influence of the temperature during the joining process on the resulting welds. Therefore a joining technology with a homogenous energy input like infrared welding is used to investigate the influence of the temperature on the process, structure, and properties for welding cross-linked polyamides.

1.2. Infrared welding

Welding is an established way of joining polymer parts. The different welding technologies can be classified according to the heating method employed [15]. Technologies which use friction to heat up the joining area are for example vibration welding or friction stir spot welding. The oscillating movement of the joining partner relative to each other with a defined joining pressure is characteristic for vibration welding. Friction stir spot welding uses a rotating punch to heat up the joining partners. This process can be divided in the typical phases preheating, joining, consolidation, waiting and tool retraction [16, 17]. Infrared welding is a welding technology that uses an infrared (IR) emitter to heat up the samples. Compared to other joining technologies, such as hot plate welding, the temperature in the joining zone is a function of the machine and material parameters [18]. Advantages of infrared welding are the contactless heating of the samples and the higher geometry freedom, compare to hot plate welding, vibration welding or stir spot welding.

The infrared emitters can be separated into short wavelength (near infrared), medium wavelength (near infrared) and long wavelength emitters (mid wavelength and far infrared), Table 1 [19–21].

These radiators emit electromagnetic radiation. The primary, effective radiation is infrared radiation with a maximum intensity dependent on the surface temperature of the radiator [22]. The emitted infrared

Table 1. Classification of infrared emitters and their wavelength, based on DIN 5030 part 2, DIN EN 60519-12 and DIN EN 62798 [19–21]

IR-Radiation	Type	Wavelength [µm]	Wave number [cm^{-1}]	Examples of emitters
IR-A	Short wavelength (near infrared)	0.78–1.4	12 821–7 143	Halogen emitters
IR-B	Medium wavelength (near infrared)	1.4–3.00	7 143–3 333	Metal foil emitters
IR-C	Long wavelength (mid wavelength and far infrared)	3.00–1000	3 333–10	Ceramic emitters

light is, based on the optical properties of the irradiated material, partly reflected from the surface of the polymer [23]. This reduced radiation intensity penetrates the material and is either absorbed or transmitted [23].

The degree of absorption of the infrared light by the thermoplastic polymer depends on the wavelength as well as on the chemical and morphological structure of the polymer [23]. A characteristic absorption band for polymers is at a wavelength of 3.4 μm (wavenumber 2941 cm^{-1}) [18, 23]. This wavelength is characteristic for $[C–H]_n$ groups stretching vibrations [23, 24]. Additives or fillers can also affect the absorption properties [18]. The crystalline structure of semi-crystalline polymers affects the transmission of the infrared light. The light is refracted and reflected on the boundary layer between amorphous and crystalline areas and spherulites. The optical penetration depth decreases at an increasing wavelength, which is caused by increasing scattering [23]. The resulting temperature level depends on the emission spectrum of the emitter and the absorption properties of the material [18].

Therefore, the scope of this article is to investigate the first time for radiation cross-linked polyamide; to what extent radiation dose, the resulting degree of crosslinking and heating time affect the resulting weld line's temperature during infrared welding and whether these parameters influence the weld strength of infrared-welded, cross-linked polyamide 66. Furthermore, these results shall be correlated with non-cross-linked polyamide 66.

2. Experimental section

2.1. Materials and test specimens

For the research, polyamide 66 (V-Creamid A3H2), supplied by PTS Plastic Technologie Service, Adelshofen, Germany was used. The material is radiation cross-linkable due to the modification by 3 wt% of the triallyl isocyanurate (TAIC) cross-linking agent.

Injection molding was used to process the cross-linkable material into plate-shaped specimens with a size of 150 mm×68 mm×4 mm. The specimens were filled through a film gate and produced with an Arburg 370 injection-molding machine (Arburg GmbH + CoKG, Loßburg, Germany) at a mold temperature of 80 °C, a melt temperature of 275 °C and an injection speed of 100 $cm^3 \cdot s^{-1}$. The test specimens were cut and finally milled out of the plates, Figure 2. The joining zone was milled to get a flat surface and a uniform sample height of 51 mm. To avoid moisture absorption and a contamination of the surface, the plates were sealed separately in a vapor proof foil. These plates were exposed to electron irradiation with a 10 MeV electron accelerator. The radiation doses were 33 and 99 kGy. To exceed the radiation dose of 33 kGy, the electron radiation treatment was performed repeatedly, each with a dose of 33 kGy, in order to minimize the thermal load. Tests were also carried out on non-cross-linked material, which is termed 0 kGy in the following.

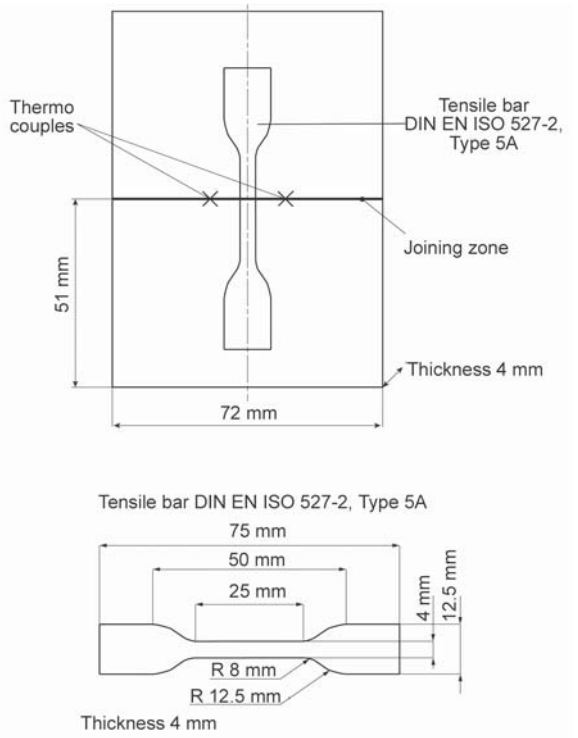

Figure 2. Dimensions of two welded test plates, places of sampling for mechanical investigations and dimensions of tensile bar

2.2. Test methods

Gel value

The degree to which the polyamide 66 plates were crosslinked was determined by a gel value analysis. With reference to DIN 16892, sections of the test specimens were boiled in a solvent (concentrated formic acid) for six hours, filtered through a glass frit POR 2 (pore size 40–100 μm) and were subsequently dried. The gel value was determined as the quotient of the mass remaining after boiling and drying and the initial mass of the specimen. For each gel value analy-

sis, the arithmetic mean and the standard deviation of the gel value from three separate measurements were determined.

Fourier transform infrared spectroscopy (FTIR)

To determine the optical properties of cross-linked polyamide in infrared wavelength ranges, a Fourier transform infrared spectroscopy (FTIR) analysis was performed with a Nicolet 6700 device from Thermo Scientific Inc. (Waltham, USA).

Transmission of cross-linked and non-cross-linked polyamide was identified between a wavenumber of 550 and 4000 cm^{-1} (wavelength of 2.5 to 19 μm) based on the attenuated total reflectance (ATR). The polyamide's extinction is defined as the measured transmission as reduced by reflection and absorption.

Infrared welding

To determine to which extent the material and processing parameters influenced the weld strength, infrared welding tests were conducted. The infrared welding tests were performed on the infrared and linear vibration welding machine Branson M-112HR (Branson Ultraschall, Dietzenbach, Germany). The welding machine is equipped with an inductive sensor to pick up the meltdown. Two, 1.6 kW, medium-wavelength metal foil emitters from Krelus AG (Oberentfelden, Switzerland) were used to heat up the upper and lower samples. The wavelength range was between 2.5 and 8 μm (wavenumber 1250 to 4000 cm^{-1}). The distance between the samples and IR emitter was 3 mm. To measure the temperature in the weld area, thermocouples Type K were used. The thermocouples were placed between the two welding plates, Figure 2. After welding, the thermocouples were cut off and new couples were used for the next trial. Simultaneously, measuring the meltdown and temperature during the process facilitates accurately detecting the weld line temperature when the samples come into first contact (T_c) with one another. This temperature was used to gauge the effect of the different processes and materials on the resulting temperature before joining. For the initial heating trials, thermocouples in different depths were placed in the welding plate. In the infrared welding tests, the heating time varied between 8 to 15 s and the joining pressure between 3 and 5 $N \cdot mm^{-2}$, Table 2.

Table 2. Welding parameters

Welding partner	Joining pressure [$N \cdot mm^{-2}$]	Heating time [s]
PA66 0 kGy/PA66 0 kGy	3/5	10/15
PA66 33 kGy/PA66 33 kGy	3/5	8/10/12/15
PA66 99 kGy/PA66 99 kGy	3/5	8/10/12

Mechanical testing (tensile test)

Tensile tests were carried out in accordance with DIN ISO 527-2 [25]. Tensile test bars of type 5 A according to EN ISO 527 were milled from the welded plates, Figure 2. Each test was performed under standard testing conditions (T = 23 °C, relative air humidity: 50%). Before testing, the specimens were dried to a constant weight at 70 °C in a vacuum furnace. The tensile strength, strain at break as well as stress at break of 3 samples were recorded. The mean and standard deviation were calculated from these 3 samples. The pull-off speed was 3 $mm \cdot min^{-1}$ for all specimens.

Light microscopic investigations

Light microscopic investigations on welds before and after mechanical testing were performed with an Axioplan light microscope from Carl Zeiss AG (Oberkochen, Germany). In order to avoid any thermal influences on the welds while preparing the specimen, the weld region was cut out of the welded plates (before mechanical testing) and the tested tensile bars with a water-cooled, low-revolution saw.

The microscopic analysis of the specimens was conducted in the transmitted light procedure on 10 μm thin cuts. Polarized light was utilized in order to characterize the morphology and geometry of the weld.

3. Results and discussion

3.1. Effect of the radiation dose on the degree of cross-linking

The electron irradiation of the polymer results in a three-dimensional network of covalent bonds between the macromolecules. With radiation at 33 kGy, a gel value of 49% with a standard deviation of 0.44 is attained. With a higher radiation dose of 99 kGy, the gel value increased to 64% with a standard deviation of 0.62.

3.2. Effect of cross-linking on the optical properties of cross-linkable polyamide 66

The extinction in relation to the wavenumber of cross-linkable polyamide 66 with and without electron

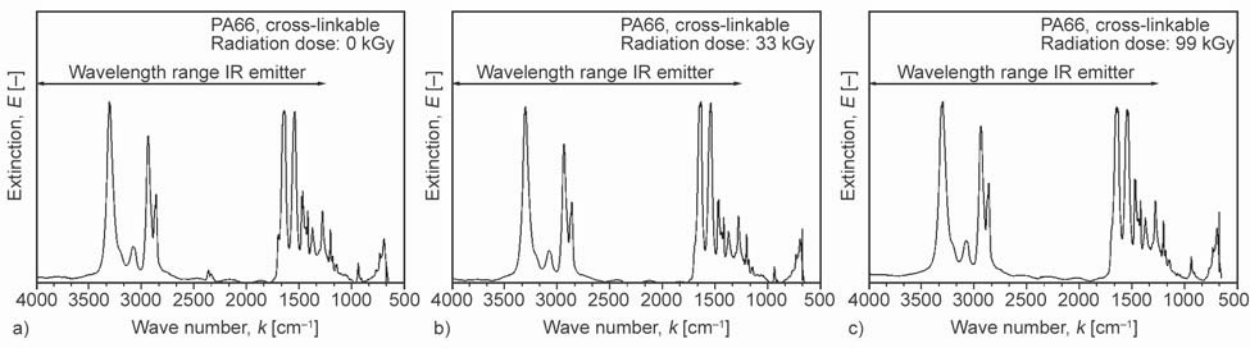

Figure 3. Extinction of radiation cross-linkable polyamide 66 (FTIR), a) radiation dose 0 kGy, b) radiation dose 33 kGy, c) radiation dose 99 kGy

beam irradiation is shown in Figure 3. At around 3000 cm^{-1}, polyamide has the typical characteristic absorption bands for $[C–H]_n$ groups stretching vibrations [23, 24]. Further, the absorption for the bending vibration of the amide group is visible at bands between 1640 and 1550 cm^{-1} [24]. The peak around 2360 cm^{-1} could be related to the absorption doublet band of carbon dioxide from the ambient air during the measurement [26]. This peak height may also likely change between measurements and is independent from the tested material. The covalent bonds between the macromolecules do not seem to be IR-active in the wavelength range of a metal foil IR emitter and therefore do not affect the absorption of cross-linkable polyamide 66 or the heating during the infrared welding process.

3.3. Temperature and meltdown of cross-linkable polyamide 66 during infrared welding

During infrared heating, the temperature measured in the weld line rapidly increased, as is evident in Figure 4. The initial peak the first couple of seconds could be attributed to the melting of the non-cross-linked polyamide. At the beginning of the heating process, no melt layer exists and the thermocouples lie on the surface of the weld line. At this position, the measurement can be affected by the environment (e.g. hot air) and lead to an inaccurate weld line temperature. At temperatures above the crystallite melting temperature, a melt layer forms and the thermocouples sink inside the melt. Here, the environmental influences are reduced and the temperature of the molten material can be measured. Inside the molten material the temperature is lower than on the weld line surface. This fact can be seen in the temperature plateauing

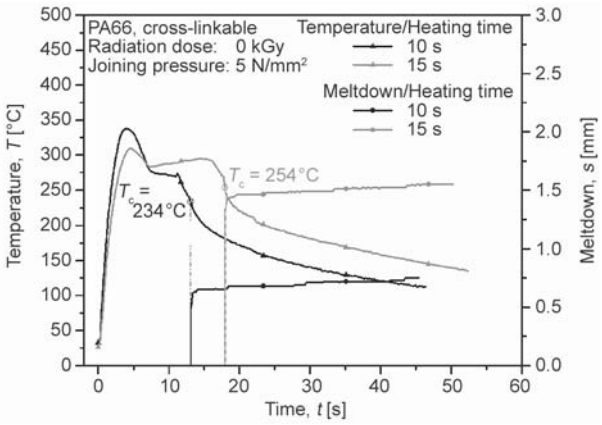

Figure 4. Influence of heating time on temperature in the weld line and meltdown while infrared welding non-cross-linked polyamide 66

before joining. Longer heating times caused the temperature at the moment of joining (T_c) to rise from 234 to 254 °C. This fact could be explained by the increasing heat energy saved in the molten material. Additionally, longer heating times increased the melt layer's thickness and the resulting meltdown from 0.4 mm after 10 seconds of heating to 1.4 mm after 12 seconds.

Cross-linked polyamide 66 showed a rapid increase in temperature within the first seconds, Figures 5 to 8. The temperature rose over time without any temperature reductions or plateaus as was the case with the non-cross-linked polyamide. This permanent rising of the temperature is also visible in different depths of the material, Figure 5. The temperature on the surface of the weld line is higher and reaches a value of 485 °C. In this stage, the thermocouples on the surface can be affected by the environment and lead to an inaccurate measurement. Therefore the temperature at moment of joining (T_c) was used to compare the different measurements. In a depth of 0.3 mm,

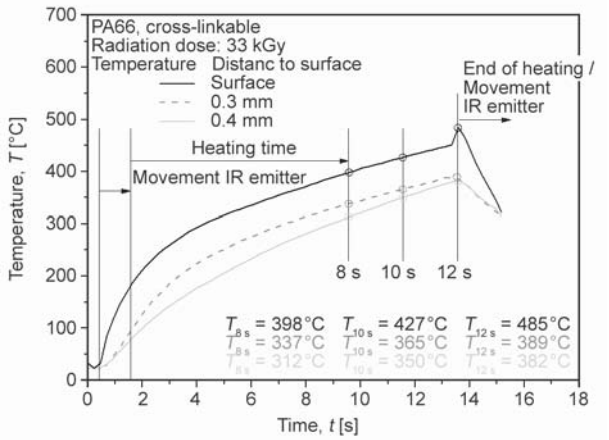

Figure 5. Influence of infrared heating cross-linked polyamide 66 on temperature in the weld zone in different depths

with a minimized impact of the environment on thermocouples, the temperature rose to a maximum of 389 °C. At this temperature a thermal degradation of the material is possible. The convergence of the temperature between 0.3 and 0.4 mm could be explained with the increasing of the temperature affected area during heating. After the heating, during the movement of the IR emitter, a convergence of the temperature of all three measured depths is visible. After this movement, the temperature at the moment of joining (T_c) rose from 238 °C after 10 seconds of heating to 277 °C after 12 seconds, Figure 6. The increase in temperature is higher than for non-cross-linked polyamide. This fact could be explained by the rubbery, elastic state of the cross-linked polyamide above the crystallite melting temperature, Figure 1. In this state, the material cannot flow. The cross-linked material remains in its rubbery, elastic state at a distance of 3 mm between the IR emitter and the sample. This allows energy inputs and resulting temperatures higher than non-cross-linked polyamide at increasing distances based on melt flow. Further, the energy outflow from the melt flow is impeded and the contact with oxygen during the heating could lead to a thermal degradation.

The increased temperature affected areas of the cross-linked polyamide 66 can be estimated with the resulting meltdown, Figure 7. The material has significantly lower mechanical properties (Figure 1) than the base material unaffected by heat and can be squeezed by the joining pressure. Therefore, the meltdown rose with longer heating times, Figure 7. The squeezing of the material leads also to a stretching of the heated material in the weld line. The maximum stretching is in the middle of the weld line [27]. The gap between the peak temperature and the temperature at the moment of joining (T_c) is based on the IR welding process. After heating, the IR emitters must be removed between the samples, whereupon the same samples must be pushed together by the joining pressure. During this period, the temperature in the joining area decreases.

As depicted in Figure 8, the radiation dose hardly affected the contact temperature (T_c) in the weld line. This could be due to nearly equal absorption bands in the wavelength range of the metal foil emitter, Figure 3. The meltdown also showed minimal effects on the radiation dose. This could be attributed to differing residual stiffness in the cross-linked material beyond the crystallite melting temperature being induced by the radiation, Figure 1. The higher sample stiffness with the higher dose of 99 kGy leads to a reduced deformation from the joining pressure. The impact of the

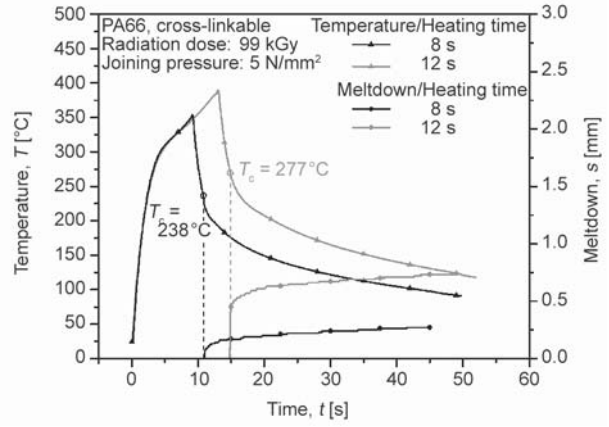

Figure 6. Influence of heating time on temperature in the weld line and meltdown while infrared welding cross-linked polyamide 66

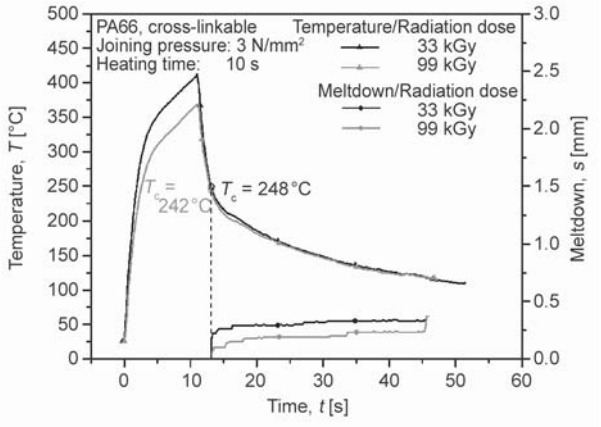

Figure 7. Influence of the radiation dose on temperature in the weld line and meltdown while infrared welding cross-linked polyamide 66

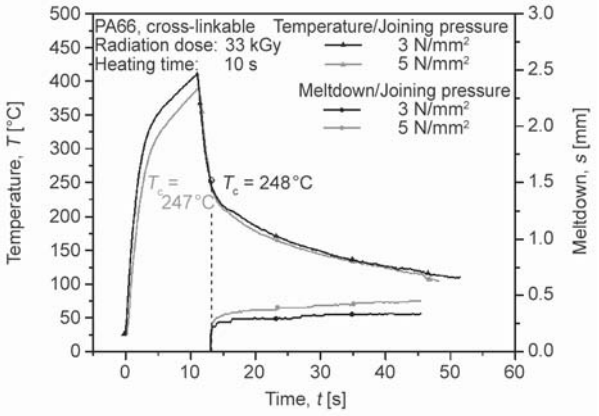

Figure 8. Impact of joining pressure on temperature in the weld line and meltdown while infrared welding cross-linked polyamide 66

joining pressure could also be seen in Figure 8. Higher pressures while joining resulted in an increase in the meltdown. Compared to non-cross-linked polyamide, the measured meltdown is, in general, lower.

3.4. Weld strength of cross-linkable polyamide 66 from infrared welding

The representative stress-strain curves from the tensile test on cross-linked polyamide 66 base material and the infrared welded samples with no radiation, a dose of 33 kGy and a dose of 99 kGy are shown in Figure 9. The curves of the base material show a ductile mechanical fracture of the samples and the samples without radiation show a lower stress at break. After exposing polyamide 66 to radiation, the base material strength increased from 80.5 $N \cdot mm^{-2}$ for the non-cross-linked polyamide to 92.8 $N \cdot mm^{-2}$ for the polyamide with a radiation dose of 99 kGy, Figure 9a and 10. Compare to the base material the infrared welded samples show a brittle mechanical fracture, Figure 9b.

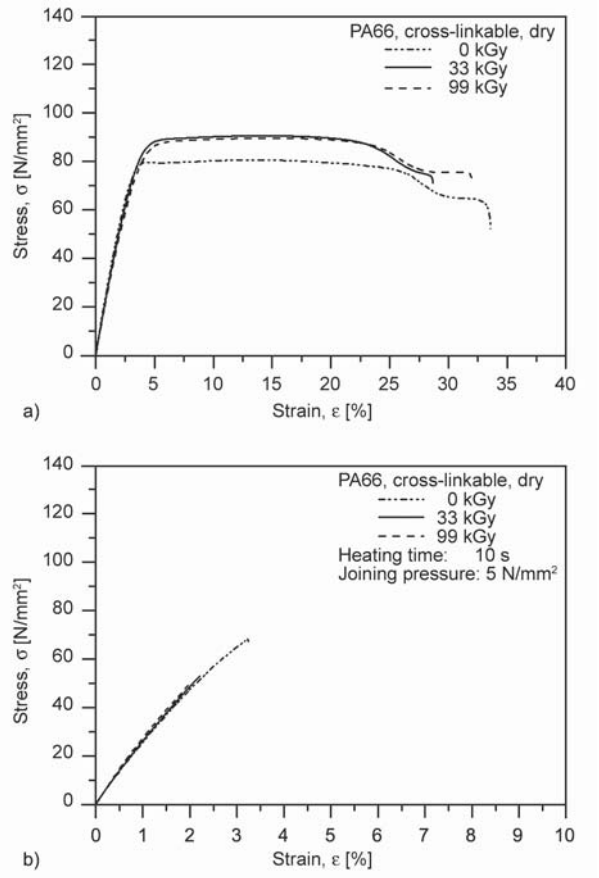

Figure 9. Stress-strain curve of cross linkable polyamide 66: (a) base material, (b) infrared welded samples

The average contact temperature and weld strength attained by the weld specimen in contrast to non-cross-linked polyamide 66 and the base material is shown in Figure 10. The resulting weld strength exhibited a dependency on the chosen processing parameters. For the non-cross-linked polyamide 66, there is no clear correlation between the weld strength, the contact temperature and the processing parameter joining pressure and the heating time, Figure 10.

For the non-cross-linked polyamide with a heating time of 10 seconds and a joining pressure of 5 $N \cdot mm^{-2}$, the maximum weld strength was 67 $N \cdot mm^{-2}$ with an average contact temperature of 239 °C. In contrast to a lower joining pressure, an increasing joining time led to a small decrease in the weld strength at 65 $N \cdot mm^{-2}$ with an increasing average contact temperature of 278 °C. The decrease in the mechanical properties could be attributed to the thermal aging of the material with longer heating times. At higher joining pressures, the aged material is transferred to the weld flash and comes into contact with the unaged material. At lower joining pressures and with shorter heating times, the transfer of the aged material into the weld flash is reduced and

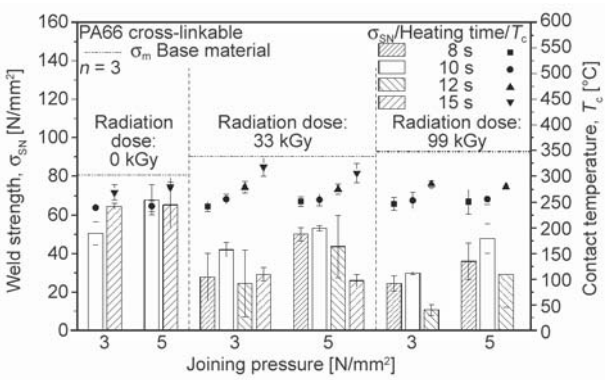

Figure 10. Weld strength and contact temperature of radiation cross-linkable polyamide 66

the requisite thickness of the melt layer cannot be achieved. Fuhrich indicated that a sufficient melt layer thickness is necessary for a high weld strength [18].

For the cross-linked polyamide 66, a correlation between joining pressure and the weld strength is evident, Figure 10. With identical heating times, the weld strength increased at higher joining pressures. A reason for the joining pressure affecting the weld strength could be the increase in the joining area, based on the squeeze of the heat-affected material and better surface contact with the joining partner.

For both radiation doses, their maximum strength was at 10 seconds heating time and at an average contact temperature of around 250 °C. Bonten showed for hot plate welding cross-linked polyethylene, that a specific temperature leads to maximum weld strength. An increasing or decreasing of this temperature leads to lower weld strength [28]. The maximum weld strength was 53 $N \cdot mm^{-2}$, with a radiation dose of 33 kGy and a joining pressure of 5 $N \cdot mm^{-2}$. For 99 kGy, the maximum weld strength was 48 $N \cdot mm^{-2}$. An increasing heating time led to the weld strength decreasing. These weld strengths are lower than the results of vibration welding radiation cross-linked polyamide 66. In these investigations weld strength up to 86 $N \cdot mm^{-2}$ have been achieved [7]. An explanation for this decrease in the weld strength of infrared welded cross-linked polyamide 66 could be the thermal aging of the material. Figure 6 shows in the heat affected zone a temperature of 389 °C after a heating duration of 12 seconds. This temperature could cause a thermal ageing of the material, especially in conjunction with the oxygen on the surface. In contrast to the non-cross linked polyamide 66, the aged material transferring out from the weld line due to the squeeze flow is impeded. With longer heating times, the aging in the weld line increases and could lead to worse adhesion between the joining partner. A higher radiation dose with possible degradation, chain scission or oxidation could enhance the effect of thermal aging.

3.5. Morphology of the weld of cross-linkable polyamide 66 from infrared welding

The results from the light microscope investigations into radiation cross-linked polyamide 66 that had been welded are shown in Figure 11 and Figure 12.

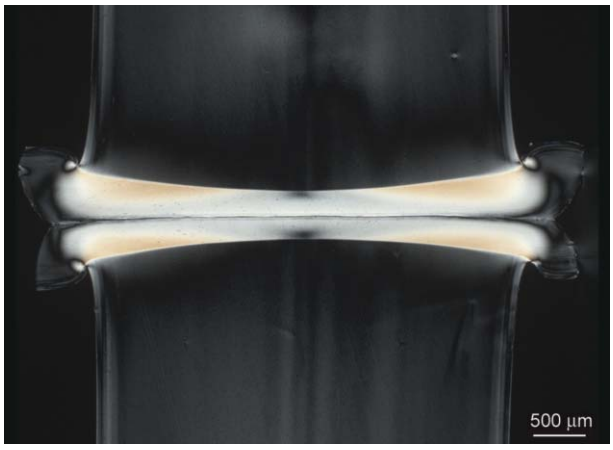

Figure 11. Transmitted light microscopy upon welding radiation cross-linkable polyamide 66 (photographs' conditions: linearly polarized light, polarization axes in the depicted image at 45°): IR heating time 10 s, 33 kGy (both parts), joining pressure 5 $N \cdot mm^{-2}$, weld strength 53.1 $N \cdot mm^{-2}$

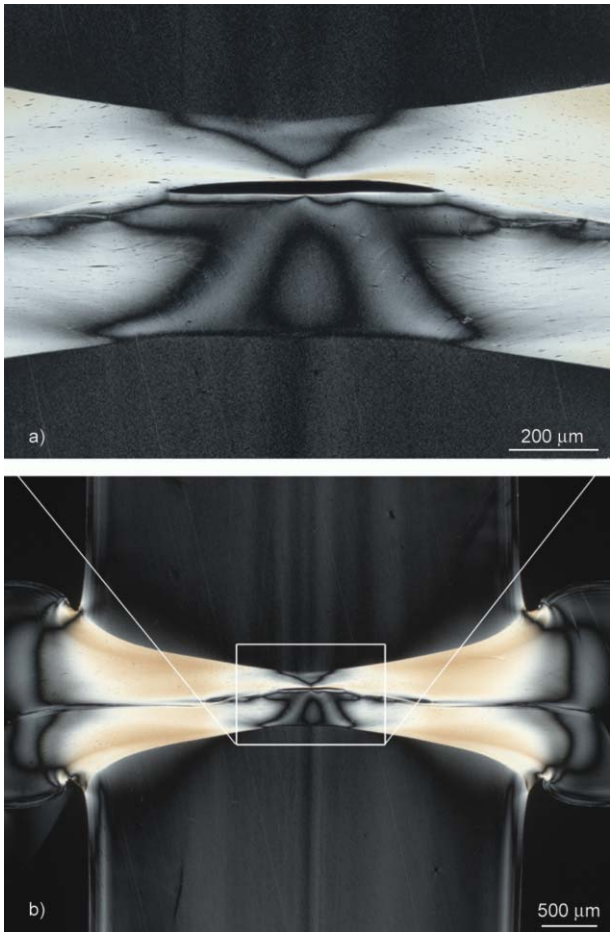

Figure 12. Transmitted light microscopy upon welding radiation cross-linkable polyamide 66 (photographs' conditions: linearly polarized light, polarization axes in the depicted image at 45°): IR heating time 15 s, 33 kGy (both parts), joining pressure 5 $N \cdot mm^{-2}$, weld strength 25.9 $N \cdot mm^{-2}$, a) detail view, b) overview

The light microscopic investigations of the tested samples are shown in Figure 13 and 14. A welded, cross-linked polyamide 66 with a high weld strength of 53 N·mm^{-2} can be seen in Figure 11. The birefringent regions originating from the center of the specimen are clearly recognizable. These may indicate orientations of the cross-linked material caused by the squeeze deformation during the joining process. Further, a smooth weld line is visible. In contrast to conventional welds between semicrystalline thermoplastics, no typical flow structures are visible. Figure 12 shows a weld with low weld strength. The size of the heat-affected material with the birefringent region is larger than the size of the sample with 10 seconds heating time and further an increase in the zone towards the edges of the sample is visible. This fact is due to longer heating times and the lateral radiation from the metal foil IR emitter, which results in a higher energy input particularly around the edges. Additionally, a hole in the wavy weld line is visible. This may be attributed to the longer heating times with the material's resulting aging.

The light microscopy investigations of specimens after the tensile tests are shown in Figure 13 and Figure 14. The position of failure during the test was mostly located in the weld line. For the specimen with the highest and the lowest weld strength a similar fracture surface, with a smooth fracture along the weld line, is visible, Figure 13 and Figure 14. With a higher joining pressure of 5 N·mm^{-2} the length of the weld line increased slightly. The notches of the weld seam were probably not a starting point for the fracture of the samples. The specimen with a heating duration of 15 seconds shows a fracture across the temperature affected area.

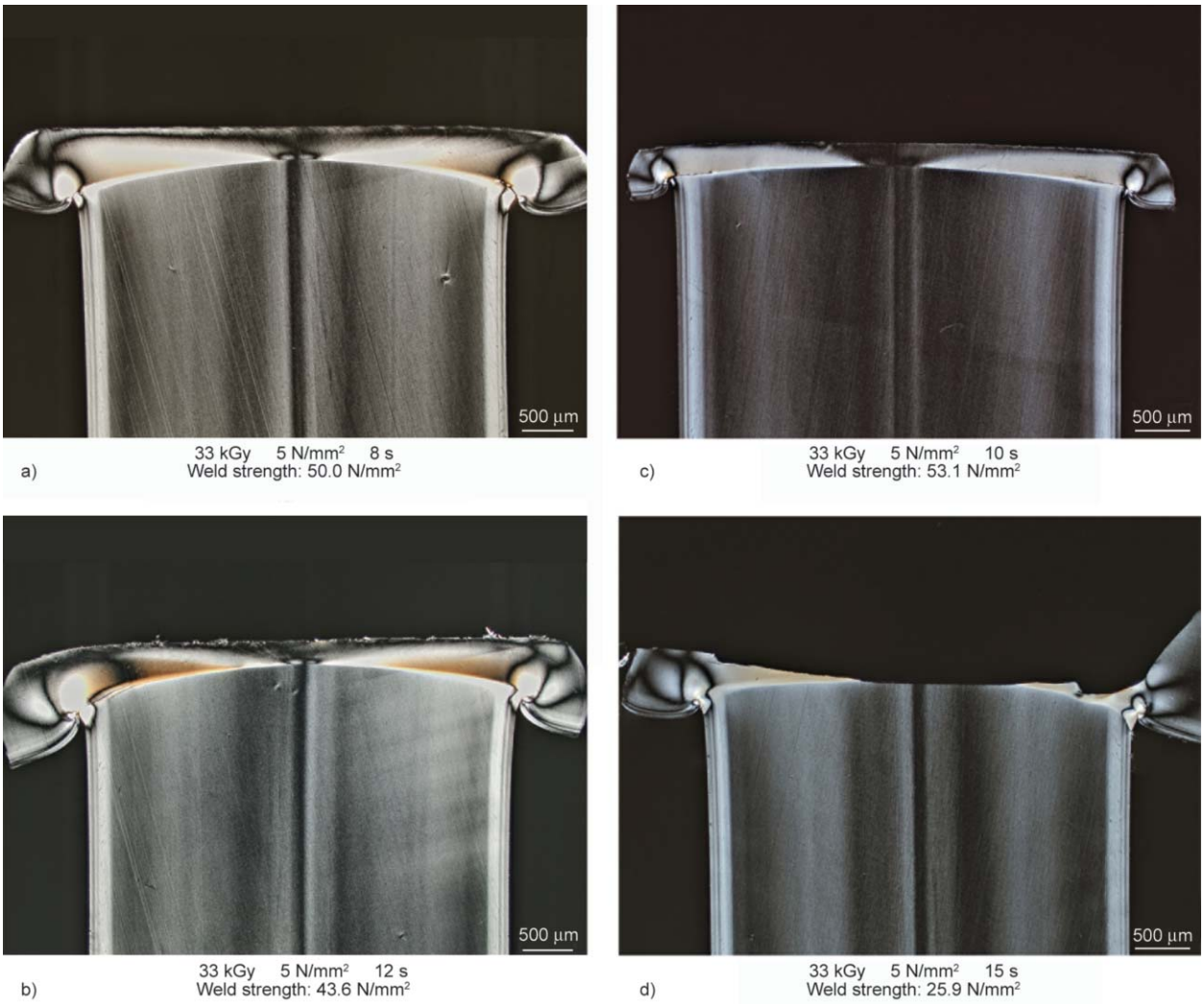

Figure 13. Transmitted light microscopy upon tensile tests of radiation cross-linkable polyamide 66 (photographs' conditions: linearly polarized light, polarization axes in the depicted image at 45°), a) 33 kGy, 5 N·mm^{-2} , 8 s, b) 33 kGy, 5 N·mm^{-2}, 12 s, c) 33 kGy, 5 N·mm^{-2}, 10 s, d) 33 kGy, 5 N·mm^{-2}, 15 s

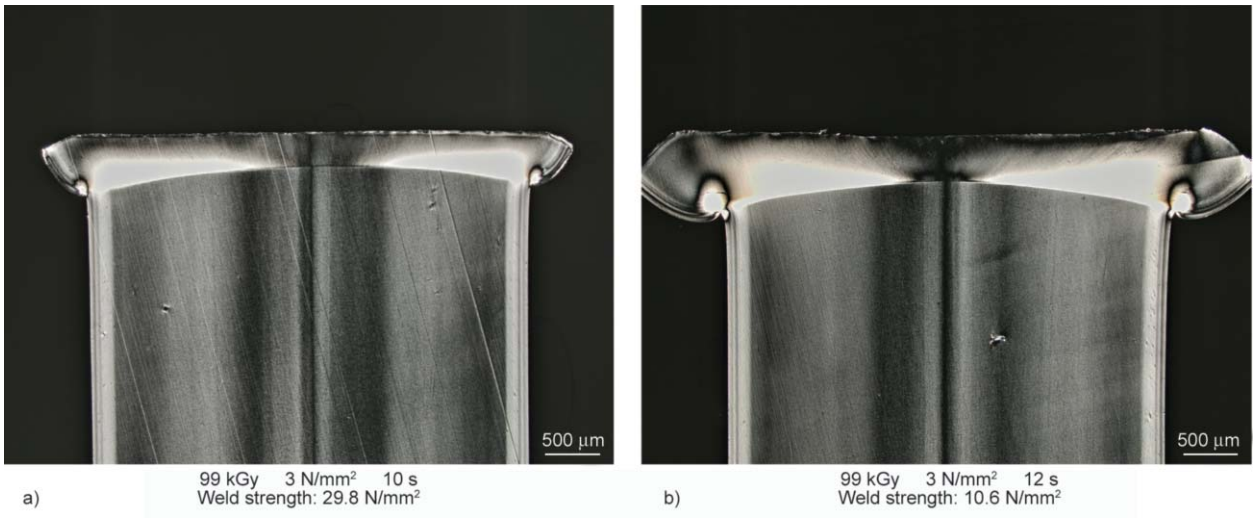

Figure 14. Transmitted light microscopy upon tensile tests of radiation cross-linkable polyamide 66 (photographs' conditions: linearly polarized light, polarization axes in the depicted image at 45°), a) 99 kGy, 3 N·mm^{-2}, 10 s, b) 99 kGy, 3 N·mm^{-2}, 12 s

4. Conclusions

The results obtained within the framework of the present research show that radiation cross-linking significantly affects the processing characteristics of infrared welding.

Electron beam irradiation led to no significant changes in the absorption bands in the wavelength range of a metal foil IR emitter but to alterations in the softening behavior above the crystallite melting temperature toward a rubber, elastic state. This state prevents squeeze flow during heating and, thus, led to the IR emitter exerting an altered energy input into the weld line. The energy outflow was impeded by the lack of squeeze flow and the material remained at a constant distance from the IR emitter during infrared heating. This is in contrast to the non-cross-linked polyamide with an increasing distance from the IR emitter, based on the melt flow.

For the cross-linked polyamide, the weld temperature showed a steady increase throughout the joining process and reached temperatures above the crystallite melting temperature. The resulting contact temperature increases with the heating duration. The meltdown proved to depend on the cross-linking-induced residual stiffness above the crystallite melting temperature and the heating time and joining pressure of the welding process. At higher radiation doses, the degree of cross-linking, and thereby the residual stiffness, increased. This stiffness emerging within the heat-affected material led to a different meltdown. With lower rates of cross-linking-induced residual stiffness, longer heating times, and higher joining pressures, the meltdown during the joining process increased. With a higher joining pressure the length of the weld line increases slightly and thus the possible joining area. Of the investigated parameters, heating duration and the resulting contact temperature exhibited a significant effect on the weld strength.

If the heating time was too short and the contact temperature was low, the specimens reflected lower values. Conversely, if the heating time was too long, the weld strength would also decrease. Around a heating time of 10 seconds, the maximum weld strength for the chosen process parameters was reached. A possible explanation for this effect could be thermal aging. The specimens with a longer heating duration exhibited a temperature which could lead to oxidative degradation of the material and subsequently to lower mechanical properties of the cross-linked material. Further investigations should explore this claim.

Acknowledgements

The authors would like to thank the German Research Foundation (DFG) for funding this work within the project DR 421/13-1 'Bonding mechanism during welding of radiation cross-linked thermoplastic polymers'. The authors are also grateful to PTS Plastic Technology Service, Adelshofen, Germany, for providing radiation cross-linkable polyamide 66 and BGS Beta Gamma Service, Bruchsal, Germany, for the electron beam irradiation.

References

[1] Makuuchi K., Cheng S.: Radiation processing of polymer materials and its industrial applications. Wiley, New Jersey (2011).

[2] Heger A., Dorschner L., Dunsch L.: Technologie der Strahlenchemie von Polymeren. Hanser, München (1990).

[3] Seefried A.: Zum Thermoformen von vernetztem Polyamid. PhD Thesis, Friedrich-Alexander-Universität Erlangen-Nürnberg, Erlangen (2015).

[4] Chapiro A.: XIIth international meeting on radiation processing Avignon 25–30 March 2001 (Polymer irradiation: Past–present and future). Radiation Physics and Chemistry, **63**, 207–209 (2002).
DOI: 10.1016/S0969-806X(01)00621-1

[5] Heinze D.: Das Verhalten von Hochpolymeren gegenüber energiereicher Strahlung. Kolloid-Zeitschrift und Zeitschrift für Polymere, **210**, 45–54 (1966).
DOI: 10.1007/BF01500434

[6] Charlesby A.: Atomic radiation and polymers. Pergamon Press, Oxford (1960).

[7] Leisen C., Menacher M., Drummer D.: Influence of radiation cross-linking of polyamide 66 on the characteristics of the vibration welding process. Polymer Engineering and Science, **55**, 2493–2499 (2015).
DOI: 10.1002/pen.24139

[8] Seefried A., Drummer D.: Thermoforming radiation crosslinked polyamide – Effects of degree of cross linking and thermoforming processing conditions. in 'Proceedings of the 72nd Annual Technical Conference of the Society of Plastics Engineers, Las Vegas, USA' Vol 72, 2400–2407 (2014).

[9] Drummer D., Seefried A.: Thermoformability of radiation cross linked polyamide 12. in 'Proceedings of the 69th Annual Technical Conference of the Society of Plastics Engineers: The Plastics Conference, Boston, USA' Vol 69, 2520–2526 (2011).

[10] Lee D. W.: Permanent vernetzt – Elektronenstrahl-Vernetzung von PA und PBTP. Kunststoffe, 91, 78–80 (2001).

[11] Bernstein B. S., Odian G., Orban G., Tirelli S.: Radiation crosslinking of nylon 66 and poly(vinyl alcohol). Journal of Polymer Science Part A: Polymer Chemistry, **3**, 3405–3412 (1965).
DOI: 10.1002/pol.1965.100031004

[12] Brocka Z.: Werkstoff- und Einsatzpotential strahlenvernetzter Thermoplaste. PhD Thesis, Friedrich-Alexander-Universität Erlangen-Nürnberg, Erlangen (2008).

[13] Wiedmer S., Gellner D., Friedrich K.: Effect of electron-beam radiation on thermoplastic composites. Plastics, Rubber and Composites, **34**, 76–84 (2005).
DOI: 10.1179/174328905X48568

[14] Leisen C., Seefried A., Drummer D.: Post-cross-linking behavior of radiation cross-linked polyamide 66 during vibration welding. Polymer Engineering and Science, in press (2016).
DOI: 10.1002/pen.24300

[15] Ehrenstein G. W.: Handbuch Kunststoff-Verbindungstechnik. Hanser, München (2004).

[16] Lambiase F., Paoletti A., Di Ilio A.: Mechanical behaviour of friction stir spot welds of polycarbonate sheets. The International Journal of Advanced Manufacturing Technology, **80**, 301–314 (2015).
DOI: 10.1007/s00170-015-7007-4

[17] Paoletti A., Lambiase F., Di Ilio A.: Analysis of forces and temperatures in friction spot stir welding of thermoplastic polymers. International Journal of Advanced Manufacturing Technology, **83**, 1395–1407 (2016).
DOI: 10.1007/s00170-015-7669-y

[18] Fuhrich R.: Infrarotschweißen von Kunststoffen mit thermischen Strahlungsemittern. Verlag Dr. Hut, München (2013).

[19] DIN 5030-2: Spectral measurement of radiation; radiation sources; Selection criteria (1982).

[20] DIN EN 62798: Industrial electroheating equipment – Test methods for infrared emitters (2015).

[21] DIN EN 60519-12: Safety in electroheating installations – Part 12: Particular requirements for infrared electroheating installations (2014).

[22] Gehde M., Friedrich S., Motchev S.: Strahlungserwärmung beim Kunststoffschweißen mit Infrarotstrahlung. Joining Plastic – Fügen von Kunststoffen, **1**, 58–63 (2008).

[23] Heil M.: Heizstrahlerschweißen thermoplastischer Kunststoffe. PhD Thesis, Universität Gesamthochschule Paderborn, Paderborn (1994).

[24] Lin-Vien D., Colthup N. B., Fateley W. G., Grasselli J. G.: The handbook of infrared and Raman characteristic frequencies of organic molecules. Academic Press, London (1991).

[25] DIN EN ISO 527-2: Plastics – Determination of tensile properties – Part 2: Test conditions for moulding and extrusion plastics (2012).

[26] Gottwald W., Wachter G.: IR-Spektroskopie für Anwender. Wiley-VCH, Weinheim (1997).

[27] Menacher M.: Vibrationsschweißen von strahlenvernetztem Polyamid 66. PhD Thesis, Friedrich-Alexander-Universität Erlangen-Nürnberg, Erlangen (2015).

[28] Bonten C.: Contribution to an explanation of the acting mechanism in welded seams out of semicrystalline thermoplastics. Shaker Verlag, Aachen (1999).

eXPRESS Polymer Letters Vol.10, No.10 (2016) 860–872
Available online at www.expresspolymlett.com
DOI: 10.3144/expresspolymlett.2016.80

Analytical prediction of void distribution and a minimum-void angle in anisotropic fabrics for radial injection resin transfer molding

R. Matsuzaki[1*], *M. Naito*[1], *D. Seto*[2], *A. Todoroki*[2], *Y. Mizutani*[2]

[1]Department of Mechanical Engineering, Tokyo University of Science, 2641 Yamazaki, Noda, 278-8510 Chiba, Japan
[2]Department of Mechanical Sciences and Engineering, Tokyo Institute of Technology, 2-12-1 O-okayama, Meguro, 152-8552 Tokyo, Japan

Received 20 March 2016; accepted in revised form 5 June 2016

Abstract. 2D radial injection vacuum-assisted resin transfer molding experiments were performed using anisotropic plain-woven fabrics to determine the void distribution and the relationship between the void fraction and the resin flow velocity at arbitrary resin impregnation angles. The obtained void fraction values vary with the impregnation angle and velocity, while void formation is very difficult at the minimum-void angle oriented in neither the warp nor the weft direction. Moreover, the impregnation in the fabric microscopic structure is characterized by two patterns separated at the minimum-void angle. Based on the experimental results, a mathematical model for predicting the void fraction value at arbitrary impregnation angles and velocities and for calculating the minimum-void angle was developed. A comparison of the model predictions with the experimental results revealed a good agreement between them.

Keywords: *polymer composites, processing technologies, modeling and simulation, resin transfer molding (RTM), defects*

1. Introduction

Vacuum-assisted resin transfer molding (VaRTM) has attracted attention because of its capability to replace the autoclave molding method with a low-cost composite material molding method [1–3]. However, resin impregnation of the VaRTM may be insufficient due to the inhomogeneity of the fabrics used for reinforcement [4, 5], resulting in the formation of cavities or voids, which decrease the strength of the final product [6–8]. The voids formed during the impregnation may be classified as macro-scale voids, meso-scale voids or micro-scale voids depending on their size. A macro-scale void is also called a dry spot and is formed in the domain where the fabric is not impregnated by the resin because of inappropriate molding conditions [9–11]. A meso-scale void is caused by inter-bundle air trapping resulting from the differences between the high value of the intra-bundle resin velocity and the low value of the inter-bundle resin velocity [12–14]. A micro-scale void is formed by the air trapped in the bundles due to the differences between the low value of the intra-bundle resin flow velocity and the high value of the inter-bundle resin flow velocity [13, 15, 16].

Various studies have been conducted on the prevention of void formation. To prevent the appearance of macro-scale voids, various simulations were performed to determine the optimal gate location [17–20]. Unlike the macro-scale voids, meso-scale and micro-scale voids are caused by the unevenness of the fabric microstructure, which depends on the capillary number, and numerical models for predicting the void fraction values have been developed in previous studies [13, 21, 22]. Park *et al*. [21] proposed a method

*Corresponding author, e-mail: rmatsuza@rs.tus.ac.jp

for predicting the meso-scale and micro-scale void fractions by calculating the intra-bundle and inter-bundle flow velocities. Matsuzaki *et al*. [23] presented a model for predicting the meso-scale void-fraction in the warp and weft directions of anisotropically woven fabrics. They constructed a model for predicting the amount of void formation based on the void-formation process observed in the experiment and compared the void-formation estimation and measurement results. However, these previous studies neither developed nor validated a prediction model that takes into account the effects produced by the angle and velocity of the resin impregnation on void formation in an anisotropic or any other type of fabric; only the relationship between the resin flow velocity and void formation during 1D resin impregnation was investigated. During resin impregnation in a real structure, the resin flows through the fabric at an arbitrary angle and velocity owing to the complexity of the fabric structure and the effects of the resin infusion point. Therefore, it is necessary to evaluate the amount of void formation in relation to the impregnation angle and resin velocity because void formation is thought to be predicted by estimating the amount of void formation in relation to the resin velocity for impregnation in an arbitrary direction, with the actual impregnation being not just in the warp and weft directions. In addition, the resin impregnation path through the microscopic structure of the fabric may change with the resin impregnation angle, and there may possibly be an optimal value of the angle that reduces the void fraction compared to when the resin is injected in the warp or the weft direction.

The purpose of this study is to evaluate the effect of the resin impregnation angle in an anisotropic fabric on the relationship between the amount of voids formed and the resin velocity. We performed experimental 2D radial-injection VaRTM and investigated the meso-scale void fraction distribution and the void formation mechanism for one-layered anisotropically woven fabrics. Henceforth in this paper, the word 'void' refers to a meso-scale void. Based on the experimental results, we also developed an analytical model for predicting the void fraction for an arbitrary resin impregnation angle and velocity, and for determining the optimal minimum-void angle. The developed model was validated by comparing its predictions with the experimental results. It should be noted that because the subject of the present study is plain-woven fabric, the model presented is for fabric that has sufficiently large inter-bundle cavities for which the void fraction can be estimated if the size of the voids formed in inter-bundle cavities exceeds the thickness of the fabric.

2. Void observations in the 2D radial-injection VaRTM

2.1. 2D radial-injection VaRTM

To study the relationship between the resin flow velocity and the void fraction during resin impregnation in a fabric at an arbitrary angle, an experimental 2D radial-injection VaRTM was performed from the fabric center. Figure 1 shows a schematic of the experimental device used in this work. A one-layer glass fabric was inserted between the upper and the bottom glass molds. The circumference of the mold was sealed with a sealant tape, while the glass mold was fixed with a vice. Spacers made from a 0.3 mm thick glass-fiber reinforced plastic were used to adjust the gap between the glass molds, while the thickness of the fabric was maintained constant. The pressure in the vacuum pump was controlled by a pilot-type vacuum regulator (Koganei, NVR200-01). Table 1 lists the material properties of the two fabrics used in the

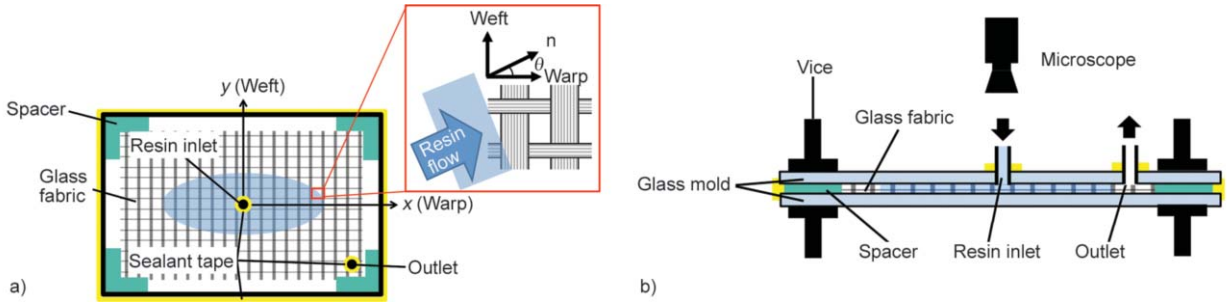

Figure 1. A schematic of the 2D VaRTM experiment. (a) Top view: the resin is impregnated radially from the center. (b) Side view: the fabric is laid between the transparent glass boards. The void fraction and void distribution are observed by a microscope and a camera.

Table 1. Material properties of the fabrics used in this work

Property	Value (SD)	
	M155	M200
Macroscopic porosity, Φ [%]	19.6 (±0.68)	15.2 (±0.62)
Height of a fiber bundle in the warp direction, h_{warp} [m]	$1.50 \cdot 10^{-4}$ ($\pm 0.04 \cdot 10^{-4}$)	$1.8 \cdot 10^{-4}$ ($\pm 0.04 \cdot 10^{-4}$)
Height of a fiber bundle in the weft direction, h_{weft} [m]	$1.10 \cdot 10^{-4}$ ($\pm 0.04 \cdot 10^{-4}$)	$1.2 \cdot 10^{-4}$ ($\pm 0.13 \cdot 10^{-4}$)
Distance between the bundles in the warp direction, l_{warp} [m]	$4.80 \cdot 10^{-4}$ ($\pm 0.27 \cdot 10^{-4}$)	$4.2 \cdot 10^{-4}$ ($\pm 0.26 \cdot 10^{-4}$)
Distance between the bundles in the weft direction, l_{weft} [m]	$6.50 \cdot 10^{-4}$ ($\pm 0.41 \cdot 10^{-4}$)	$6.8 \cdot 10^{-4}$ ($\pm 0.38 \cdot 10^{-4}$)
Macroscopic permeability in the warp direction, K_x [m^2]	$4.01 \cdot 10^{-10}$ ($\pm 3.94 \cdot 10^{-11}$)	$4.49 \cdot 10^{-10}$ ($\pm 1.62 \cdot 10^{-10}$)
Macroscopic permeability in the weft direction, K_y [m^2]	$5.39 \cdot 10^{-11}$ ($\pm 5.73 \cdot 10^{-12}$)	$5.61 \cdot 10^{-11}$ ($\pm 2.72 \cdot 10^{-11}$)
Width of a fiber bundle in the warp direction, w_{warp} [m]	$5.70 \cdot 10^{-4}$ ($\pm 0.16 \cdot 10^{-4}$)	$6.9 \cdot 10^{-4}$ ($\pm 0.32 \cdot 10^{-4}$)
Width of a fiber bundle in the weft direction, w_{weft} [m]	$1.00 \cdot 10^{-3}$ ($\pm 0.53 \cdot 10^{-4}$)	$1.1 \cdot 10^{-3}$ ($\pm 0.49 \cdot 10^{-4}$)
Porosity inside a bundle, φ_f [%]	48 (±8.1)	48 (±8.1)
Fiber radius r [μm]	4.5	4.5

experiments: M155K104 and M200K104 (Unitika Glass Fiber; henceforth referred to as M155 and M200, respectively; see also Figure 2). The fiber bundle of M200 was bigger than that of M155, while the macroscopic cavity ratio of the former material was smaller. The material properties of the unsaturated polyester resin (DH material, Sundhoma PC184-C) are listed in Table 2. In addition, the impregnation angle of the resin was set to 0° for the warp direction of the fabric and to 90° for the weft direction. In Figure 1a, the resin impregnation direction is denoted by **n**. The resin impregnation angle θ was defined as the angle between the warp direction and the resin impregnation direction n. The vacuum pressure P_{vac} was set to 50 kPa for M155 and 30 kPa for M200 during the experiments. In a preliminary experiment, micro-scale void formation was hardly observed. Vacuum pressures under which meso-scale void formation was likely to be observed were sought out in the respective fabrics, and the experiments were performed at the appropriate pressure.

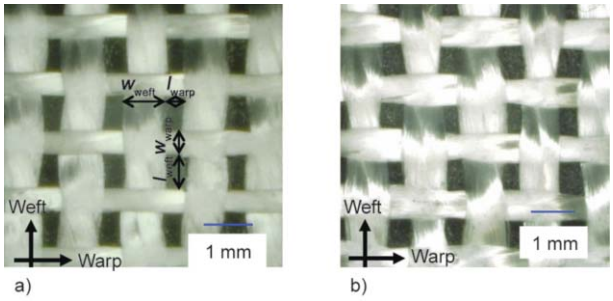

Figure 2. Fabrics used for the experiments in this work: (a) M155, (b) M200

Table 2. Material properties of the resin at 25 °C

Property	Value
Viscosity, μ [Pa·s]	0.169
Product of the surface energy γ and the cosine of the contact angle θ_c, ($\cos\theta_c$) [Nm]	0.025

To determine the void distribution for an arbitrarily set resin impregnation angle in the fabric, we used a camera to photograph the entire material after the completion of the resin impregnation process. The x axis and the y axis were defined as the warp and weft directions, respectively, with the origin at the resin inlet point. Because the resin impregnation was performed radially it was assumed to be symmetrical, and the measurements were only conducted in the domain of $x > 0$ and $y > 0$. To evaluate the effect of the impregnation direction on the relationship between the resin flow velocity and the void fraction, the void fraction value was determined at different impregnation angles. A microscope (Keyence VHX-900) was used to photograph the fabrics after the flow front had passed at an arbitrary angle. As shown in Figures 3, the photographic images were digitally processed to extract the outline of the voids and measure the void fraction. The voids are columnar in shape, thus it was assumed that the 2D void fraction value

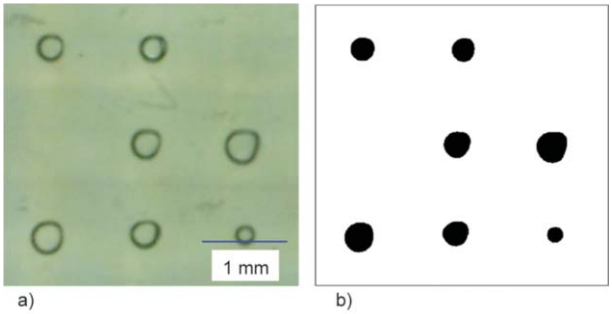

Figure 3. A method of measuring the void fraction: (a) voids observed with a microscope, (b) an image analysis of the obtained voids to determine the void fraction value

measured by means of the image analysis was equal to the volumetric void fraction [24].

2.2. Experimental results and discussion

Figures 4 show the resin impregnation and void formation in the microscopic structures of the M200 fabric at impregnation angles of 30 and 75°, respectively. The domains surrounded by the two warp bundles and two weft bundles are indicated by the red dotted lines. For both impregnation angles, the voids formed by the air trapping between the bundles were due to the fingering caused by the difference between the inter-bundle and intra-bundle resin flow velocities. In addition, the air trapping at the 30° impregnation angle was due to the completion of the resin impregnation in the weft bundle after that in the warp bundle. In contrast, the air trapping at the 75° impregnation angle was due to the completion of the resin impregnation in the warp bundle after that in the weft bundle. These observations confirm that the pattern of the intra-bundle resin impregnation vary with the impregnation angle. It should be noted that the formation of an undulating flow front is not considered problematic, because when observed microscopically, it can be regarded as impregnation at an oblique angle in the normal direction of the flow front. Moreover, the resin impregnation of crimps is extremely fast owing to the high fiber content and high capillary pressure. Furthermore, because crimps are present in both warp and weft fiber bundles, there is little impact on the resin impregnation when voids are shaped.

Figures 5a and 5b show the void distributions in the M155 and M200 fabrics, respectively. The black points represent the voids, and the white part corresponds to the domain of the impregnated resin. The figures show that it is very difficult for voids to appear at the minimum-void angle value θ_{min}. The 'minimum-void angle' was obtained by measuring, in the void distribution images, the direction where the void distribution was the smallest. Moreover, the change in the void formation pattern occurs at the minimum-void angle (as observed in Figure 4). From the void distributions, the minimum-void angle θ_{min} was determined to be approximately 49° for M155 and 53° for M200. Figures 5c and 5d show the relationships between the void fractions and the capillary number Ca^* for M155 and M200, respectively. The void fraction was measured at resin impregnation angles of 0, 30, 75, and 90°, and θ_{min} values of 49° for M155 and 53° for M200. The results shown in the figure indicate that the void fraction increases with decreasing the macroscopic resin flow velocity regardless of the impregnation angle; this happens because the difference between the intra-bundle and inter-bundle flow velocities increases with decreasing the macroscopic flow velocity resulting in an increase in the trapped air volume [24–26]. In addition, the resin flow velocity at the beginning of void formation (i.e. the flow velocity when air gets trapped between bundles and voids start to form) was highest at an impregnation angle of 0° and lowest at the minimum-void angle θmin for both fabrics. The reason for the difference in the velocity of

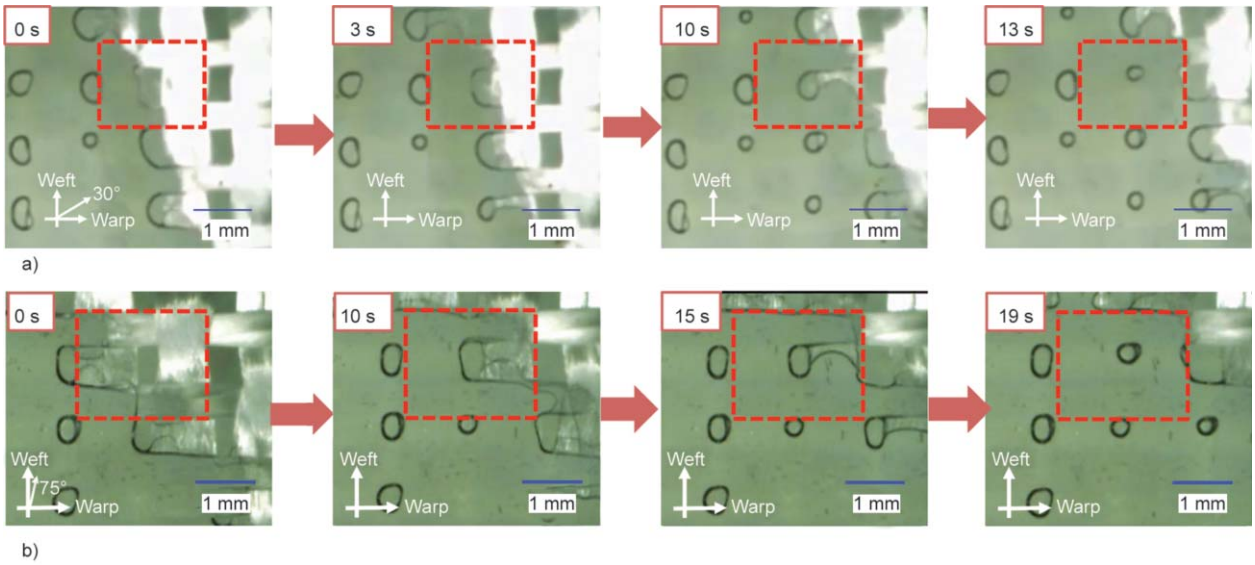

Figure 4. Resin impregnation and void formation in the microscopic structure of M200 as observed with a microscope at impregnation angles of (a) 30° and (b) 75°

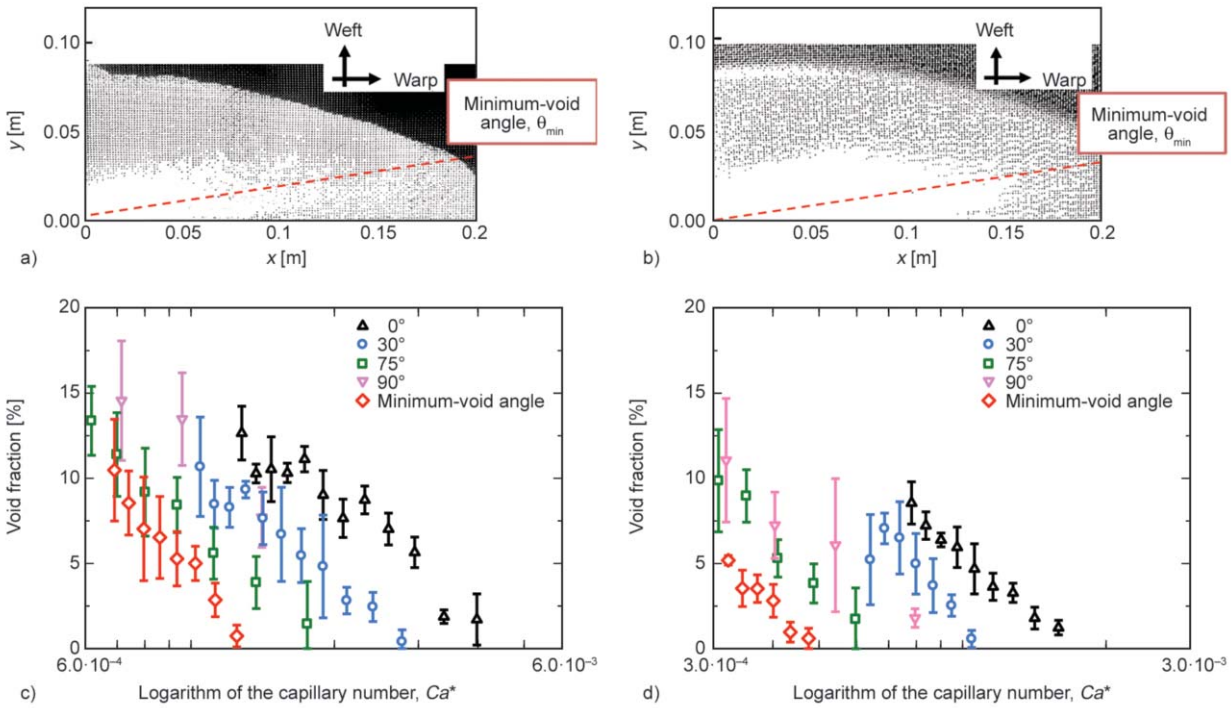

Figure 5. An observed void fraction distribution in the 2D radial injection VaRTM. The black points indicate voids, and the red line represents the impregnation angle corresponding to the minimum void fraction: (a) M155, (b) M200. An experimentally determined relationship between the capillary number and the void fraction at different flow directions: (c) M155, (d) M200.

void formation depending on the impregnation angle is attributed to the fact that the time required for intra-bundle and inter-bundle resin impregnation varies with the changes in the impregnation path length. The variation in the length of the intra-bundle impregnation path is larger than that of the length of the inter-bundle impregnation distance, as the impregnation angle inclines at an angle ranging from 0 to 90°. Moreover, because the physical properties and the macroscopic infiltration coefficient of the fiber bundles differ in the warp and weft directions, the timing of the void formation varies.

3. Analytical model for the void fraction prediction

3.1. Void formation

Figure 6 depicts a unit cell of the fabric used for the development of the void fraction prediction model. The unit cell is representative of the 2D composition of the fabric and contains two weft bundles and two warp bundles. In general, the unit cell was defined to consist of bundles, crimps, and an inter-bundle cavity.

The resin impregnation process of the unit cell used for developing the void fraction prediction model is

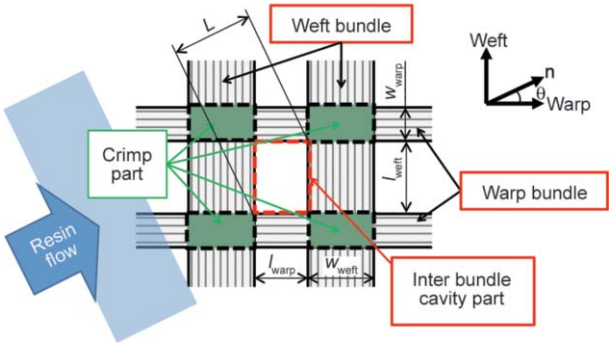

Figure 6. A unit cell of the woven fabric used for the void fraction prediction model

shown in Figure 7. The first stage shown in Figure 7a corresponds to the start of the impregnation process (0 s, Figure 4a), and the macroscopic flow front reaches one of the crimps in the unit cell. At this time, the macroscopic flow front makes contact with the lower fiber bundle at the red dotted line shown in Figure 7a. The resin impregnation thereafter progresses to the second stage shown in Figure 7b, which corresponds to the image at 10 s in Figure 4a. At this stage, resin impregnation in the transverse fiber bundle on the upstream side of the unit cell is completed, and the impregnation in the inter-bundle cavity begins as indicated by the red dotted line in Figure 7b. The resin im-

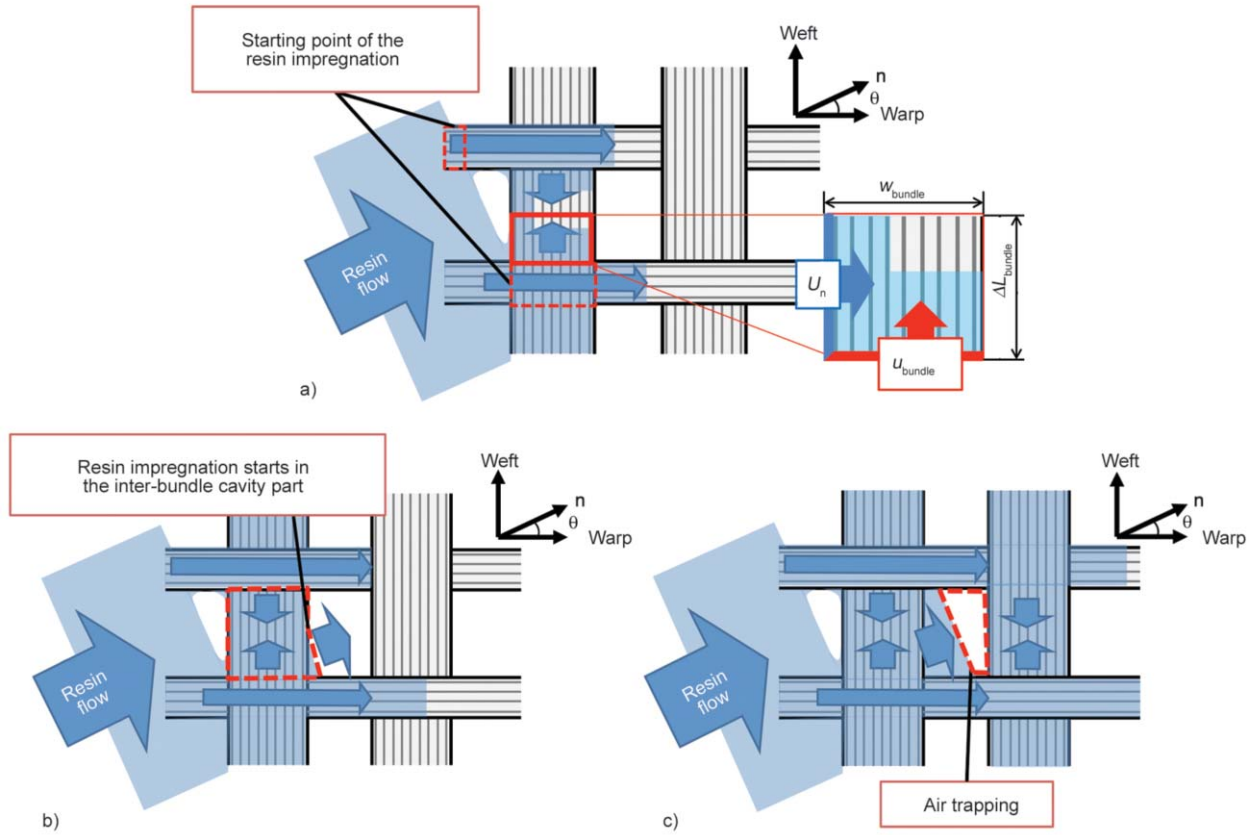

Figure 7. Stages of the resin impregnation in the unit cell: (a) Phase 1. Impregnation begins in the unit cell; the mechanism of the transverse bundle impregnation is shown. (b) Phase 2. After the completion of the transverse bundle impregnation, the resin impregnation of the inter-bundle cavity begins. (c) Phase 3. The intra-bundle resin impregnation is complete, and the air trapping process begins.

pregnation then progresses to the third stage shown in Figure 7c, which corresponds to the image at 19 s in Figure 4a. The intra-bundle resin impregnation in the unit cell is completed earlier than the inter-bundle impregnation due to the difference between the respective resin flow velocities. After the completion of the intra-bundle resin impregnation, the progress of the inter-bundle impregnation ceases, and the air trapped in the inter-bundle cavity forms a void. It should be noted that the inter-bundle impregnation

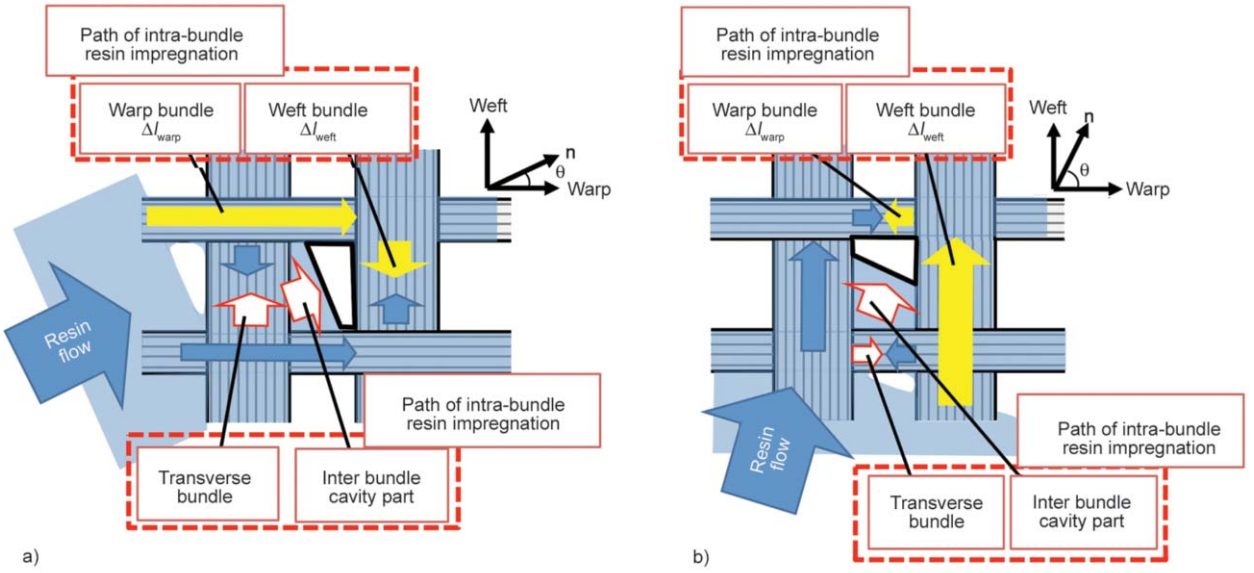

Figure 8. Descriptions of the impregnation paths in the unit cell: (a) Pattern 1, (b) Pattern 2

path was modeled as the impregnation of the upstream transverse bundle and the impregnation of the inter-bundle cavity surrounded by fiber bundles. Based on the void formation pattern for each impregnation angle in Figure 4, the impregnation paths were determined for Patterns 1 and 2 corresponding to the small and large impregnation angles, respectively, as shown in Figure 8. Detailed impregnation path modeling for each pattern will be performed in Sections 3.2 and 3.3.

3.2. Intra-bundle impregnation path

An intra-bundle resin flow velocity for each bundle (warp or weft) is defined by Equation (1), which is based on the Darcy's law with an additional term for the capillary pressure gradient [21, 25]:

$$u = -\frac{k}{\mu\varphi_{cr}}\left(\frac{\partial P}{\partial n_{axis}} - \frac{P_c}{\Delta l}\right) \tag{1}$$

where μ is the viscosity of the resin, P_c is the capillary pressure in the intra-fiber bundles, φ_{cr} is the crimp porosity, Δl is the intra-bundle impregnation distance. $\partial P/\partial n_{axis}$ denotes the macroscopic pressure gradients in the warp and weft bundle directions defined by Equations (2) and (3), respectively:

$$\frac{\partial P}{\partial n_{axis,\,warp}} = \frac{\partial P}{\partial n}\cos\theta \tag{2}$$

$$\frac{\partial P}{\partial n_{axis,\,weft}} = \frac{\partial P}{\partial n}\sin\theta \tag{3}$$

where $\partial P/\partial n$ is the macroscopic pressure gradient in the resin impregnation direction. k is the permeability of each warp and weft bundle depending on the crimp permeability [27]. The crimp permeability is determined by the ratio of the longitudinal fiber bundle thickness to the transverse bundle thickness as shown in Figure 9a as well as the by the permeabilities of the warp and weft bundles in both directions (Equation (4)):

$$k = \frac{h_{\parallel}k_{\parallel} + h_{\perp}k_{\perp}}{h_{\parallel} + h_{\perp}} \tag{4}$$

where $h_{\parallel}$ and $h_{\perp}$ are the heights of each bundle in the bundling and transverse directions, respectively, and $k_{\parallel}$ and $k_{\perp}$ are the permeabilities of the fiber bundles in the axial and transverse directions determined by the Gebart model as expressed by Equations (5) and (6) [28]:

$$k_{\parallel} = \frac{8r_f^2}{C_{\parallel}}\cdot\frac{\varphi_{cr}^3}{(1-\varphi_{cr})^2} \tag{5}$$

$$k_{\perp} = C_{\perp}r_f^2\left(\sqrt{\frac{V_{f\,max}}{1-\varphi_{cr}}} - 1\right)^{\frac{5}{2}} \tag{6}$$

where r_f is the radius of the fiber filament, and $C_{\parallel}$, $C_{\perp}$, and $V_{f\,max}$ are the shape functions. The fibers are assumed to be hexagonally arranged; hence, $C_{\parallel}$ = 53, $C_{\perp}$=16/(9π$\sqrt{6}$), and $V_{f\,max}$ = π/$\sqrt{6}$. In addition, the fabric section corresponding to the gap between the molds is homogenized to form the 2D model shown in Figure 9b. φ_{cr} is the average porosity of the gaps between the molds in the crimps defined by Equation (7):

$$\varphi_{cr} = 1 - \frac{h_{\parallel} + h_{\perp}}{H}\cdot(1-\varphi_f) \tag{7}$$

where H is the height of the gap between the molds, and φ_f is the porosity of the fiber bundles. It should be noted that the porosity of the fiber bundles is assumed to be the same in both directions [23, 24].

In addition, the capillary pressure in Equation (1) is determined using the Young-Laplace equation represented by Equation (8) [29]:

$$P_c = \frac{2\varphi C\cos\theta_c}{r_c} \tag{8}$$

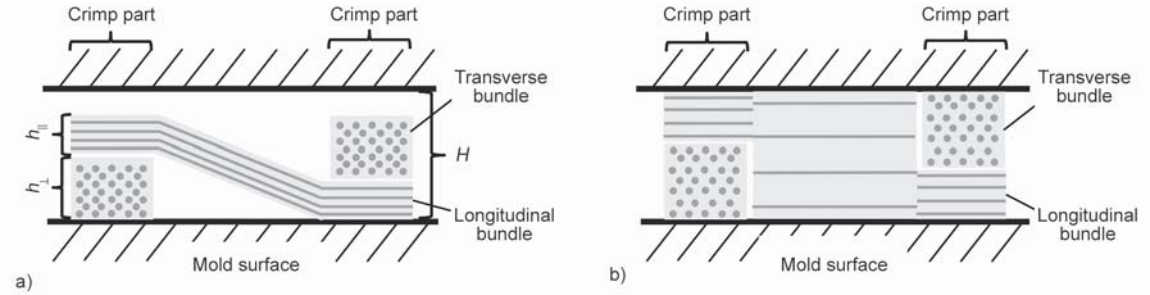

Figure 9. An effect of the thickness in the bundling direction on the superficial intra-bundle zone: (a) a realistic model, (b) an ideal model

where γ is the surface tension of the resin, C is the geometric correction factor, θ_c is the contact angle between the resin and the fibers, and r_c is the capillary radius of the fiber bundles specified by Equation (9). The geometric correction factor C is obtained by fitting the data from the measurement results in the void-fraction experiments with the results acquired using the estimated model. The average porosity in the gaps between the molds φ is defined by Equation (10):

$$r_c = \frac{\varphi}{1-\varphi} r_f \tag{9}$$

$$\varphi = 1 - \frac{h}{H}(1-\varphi_f) \tag{10}$$

where h is the height of the bundles in the warp or weft direction.

The intra-bundle impregnation distance Δl is different for Patterns 1 and 2 as indicated by the yellow arrows in Figure 8. Although both longer and shorter intra-bundle impregnation paths exist, the longer impregnation path was used to calculate the intra-bundle impregnation distance because it determines the intra-bundle impregnation time. Moreover, it was assumed for simplicity that the two intra-bundle impregnation fronts contact each other at the middle point of the downstream transverse bundle. The intra-bundle impregnation distances for the two patterns are determined by Equatios (11) and (12):

Pattern 1: $\theta < \theta_{min}$

$$\Delta l_{warp} = l_{warp} + l_{weft} \cdot \tan\theta, \quad \Delta l_{weft} = \frac{l_{weft}}{2} \tag{11}$$

Pattern 2: $\theta > \theta_{min}$

$$\Delta l_{warp} = \frac{l_{warp}}{2}, \quad \Delta l_{weft} = l_{weft} + l_{warp} \cdot \tan\left(\frac{\pi}{2} - \theta\right) \tag{12}$$

By integrating Equation (1), the intra-bundle impregnation time function Δt defined as the time required for the resin to cover a distance Δl in each warp and weft bundle was determined as shown by Equation (13):

$$\Delta t = -\frac{\mu\varphi_{cr}}{k \cdot \frac{\partial P}{\partial n_{axis}}}\left(\Delta l + \frac{P_c}{\frac{\partial P}{\partial n_{axis}}} \cdot \ln\left(1 - \frac{\frac{\partial P}{\partial n_{axis}}}{P_c} \cdot \Delta l\right)\right), \quad \frac{\partial P}{\partial n_{axis}} \neq 0 \tag{13}$$

Because the $\partial P/\partial n_{axis}$ is 0 at an impregnation angle of 90° for the impregnation of the warp bundles and at an impregnation angle of 0° for the impregnation of the weft bundles, the intra-bundle impregnation time at the respective angles is denoted by Equation (14):

$$\Delta t = -\frac{\mu\varphi_{cr}\Delta l^2}{2kP_c}, \quad \frac{\partial P}{\partial n_{axis}} = 0 \tag{14}$$

The warp impregnation time Δt_{warp} and the weft impregnation time Δt_{weft} are obtained by substituting the material properties of each bundle, namely the macroscopic pressure gradient in each bundle direction (Equations (2) and (3)), and the impregnation distances for each bundle (Equations (11) and (12)) into Equations (13) and (14), respectively. The total intra-bundle resin impregnation time Δt_{total} is specified by Equation (15):

$$\Delta t_{total} = \Delta t_{warp} + \Delta t_{weft} \tag{15}$$

The intra-bundle impregnation time increases with the impregnation angle for Pattern 1, whereas the reverse is true for Pattern 2. The minimum-void angle θ_{min} is an angle, at which the relationship between the lengths of the intra-bundle resin impregnation times in Patterns 1 and 2 is reversed. In other words, an angle that satisfies the following equation is the minimum-void angle θ_{min} (Equation (16)):

$$\Delta t_1 - \Delta t_2 = 0 \tag{16}$$

where Δt_1 and Δt_2 are the intra-bundle impregnation times for Patterns 1 and 2, respectively.

3.3. Inter-bundle impregnation path and void formation

Assuming that the resin flow velocity through the inter-bundle cavity is the same as the macroscopic flow velocity, the macroscopic resin flow velocity Un in the inter-bundle cavity in the impregnation direc tion can be expressed by Equation (17) based on the Darcy's law:

$$U_n = \frac{K_n}{\mu\Phi_n} \cdot \frac{\partial P}{\partial n} \tag{17}$$

where K_n is the permeability in the resin impregnation direction, and Φ_n is the sectional porosity of the fabric at the mold gap in the resin-impregnation direction. The subscript n denotes the resin impregna-

tion direction at the flow front. Considering the minuteness of the unit cell, if the resin flow velocity during the resin impregnation in the inter-bundle cavity is constant, the resin impregnation time in the inter-bundle cavity at an arbitrary angle ΔT_{inter} can be expressed as Equation (18):

$$\Delta T_{inter} = \frac{L}{U_n} = -\frac{\mu \Phi_n \left(l_{warp} \cos\theta + l_{weft} \sin\theta \right)}{K_n \frac{\partial P}{\partial n}} \quad (18)$$

where L is the length of the inter-bundle cavity in the flow direction, and l_{warp} and l_{weft} are the distances between the fiber bundles in the warp and weft directions, respectively (see Figure 6).

In addition, the resin impregnation of the inter-bundle cavity begins after the completion of that in the upstream transverse bundle shown in Figure 7b, and the impregnation time for the upstream transverse fiber bundle is added to the impregnation time for the inter-bundle path. As shown in Figure 7a, the resin impregnation of the transverse bundle begins at the two crimps (with an intra-bundle velocity u_{bundle}) and proceeds at the boundary between the upstream inter-bundle cavity and the transverse bundle (with a macroscopic velocity U_n). Knowing the flow volume and the transverse bundle width, the impregnation time ΔT_{bundle} of the transverse bundle can be determined by Equations (19) and (20):

$$\Delta T_{bundle} = \frac{w_{bundle} \Delta L_{bundle}}{u_{bundle} w_{bundle} + U_n \Delta L_{bundle}} \quad (19)$$

where

$$L_{bundle} = \begin{cases} \frac{l_{weft}}{2} & \text{for Pattern 1} \\ \frac{l_{warp}}{2} & \text{for Pattern 2} \end{cases} \quad (20)$$

Here w_{bundle} is the width of the transverse bundle, and ubundle can be calculated using Equation (1). From Equations (18) and (19), the total inter-bundle impregnation time ΔT_{total} can be obtained (Equation (21)):

$$\Delta T_{total} = \Delta T_{inter} + \Delta T_{bundle} \quad (21)$$

Assuming the regularity and continuity of the unit cell, the mean value of the void fraction V_v of the unit structure can be determined by Equation (22) [22]:

$$V_v = \left(1 - \frac{\Delta t_{total}}{\Delta T_{total}} \right) \cdot \Phi \quad (22)$$

where Φ is the macroscopic porosity of the fabric obtained from the ratio of the inter-bundle domain to the whole fabric area. The macroscopic porosity is obtained by measuring the ratio occupied by inter-bundle cavities by analyzing images of the fabric taken from above.

4. Validation of the analytical prediction model

4.1. Void distribution

The prediction model was applied to determine the void fraction. The material properties of the fabrics and resin used in this model are given in Tables 1 and 2. From fitting the experimental data, the geometric correction factor C for the capillary pressure was calculated to be 2.4 for M155 and 1.4 for M200. In addition, a resin infusion point radius r_0 of 0.003 m and a gap between the molds H of 0.0003 m were used for the model calculations. The macroscopic resin flow velocity and the pressure gradient values were calculated analytically (see Appendix A).

Using Equation (16), the minimum-void angle θ_{min} in the prediction model was determined to be 53° for M155 and 56° for M200. Little deviations exist between the minimum-void angle values obtained by the prediction model and those determined by the experiment (49° for M155 and 53° for M200) for both fabrics. The difference between the impregnation angles is very small for the elliptical shape indicating that the minimum-void angle θ_{min} predicted by the model is in good agreement with the experimentally determined value. Figures 10 show the predicted void distributions for M155 and M200 demonstrating that void formation in the direction of the minimum-void angle is very difficult, and that the void distribution changes at the boundary of the minimum-void angle for both fabrics. This is in agreement with the experimental observations presented in Figure 5a and 5b.

4.2. Relationship between the void fraction and the macroscopic resin flow velocity

The analytically obtained curves of the void fraction as a function of the logarithm of the resin flow velocity for both fabrics are shown in Figures 11a and 11b, where the experimental results are also presented for comparison. The obtained theoretical and experimental results are in good agreement, thus validating the void fraction prediction model described in this work.

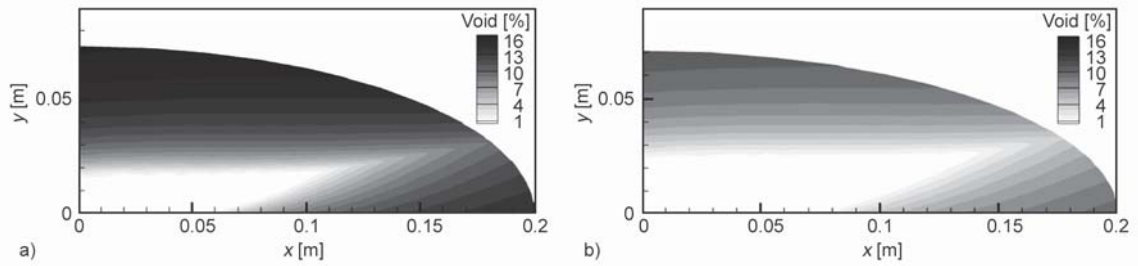

Figure 10. Void distributions produced by the single-point resin injection into the woven fabric determined by the void fraction prediction model: (a) M155, (b) M200

The curves of the void fraction as a function of the resin impregnation angle for both fabrics at a constant resin flow velocity are shown in Figures 11c and 11d. Capillary number $Ca^* = 0.00142$ and 0.000406 were used for M155 and M200, respectively. Due to a very low value of the resin flow velocity, the experimental results for M200 were not measurable at impregnation angles of 0 and 30°. At constant resin flow velocities, the void fraction was the largest at an impregnation angle of 0° for both Patterns 1 and 2 and smallest at the minimum-void angle value. The deviation between the results predicted by the model and experimental results was due to experimental variation and the model being constructed with simplified fabric. However, as the void-formation trends could be reproduced, we think that it is useful for the constructed void-formation prediction model. The reason why the deviation between the experimental and theoretical values is large in places is thought to be that the impregnation differed from the ideal situation because of disordered impregnation caused by the creases and wrinkles of the fabric. Moreover, because the measured area was small, the difference between the void formation and non-formation increased. Further-

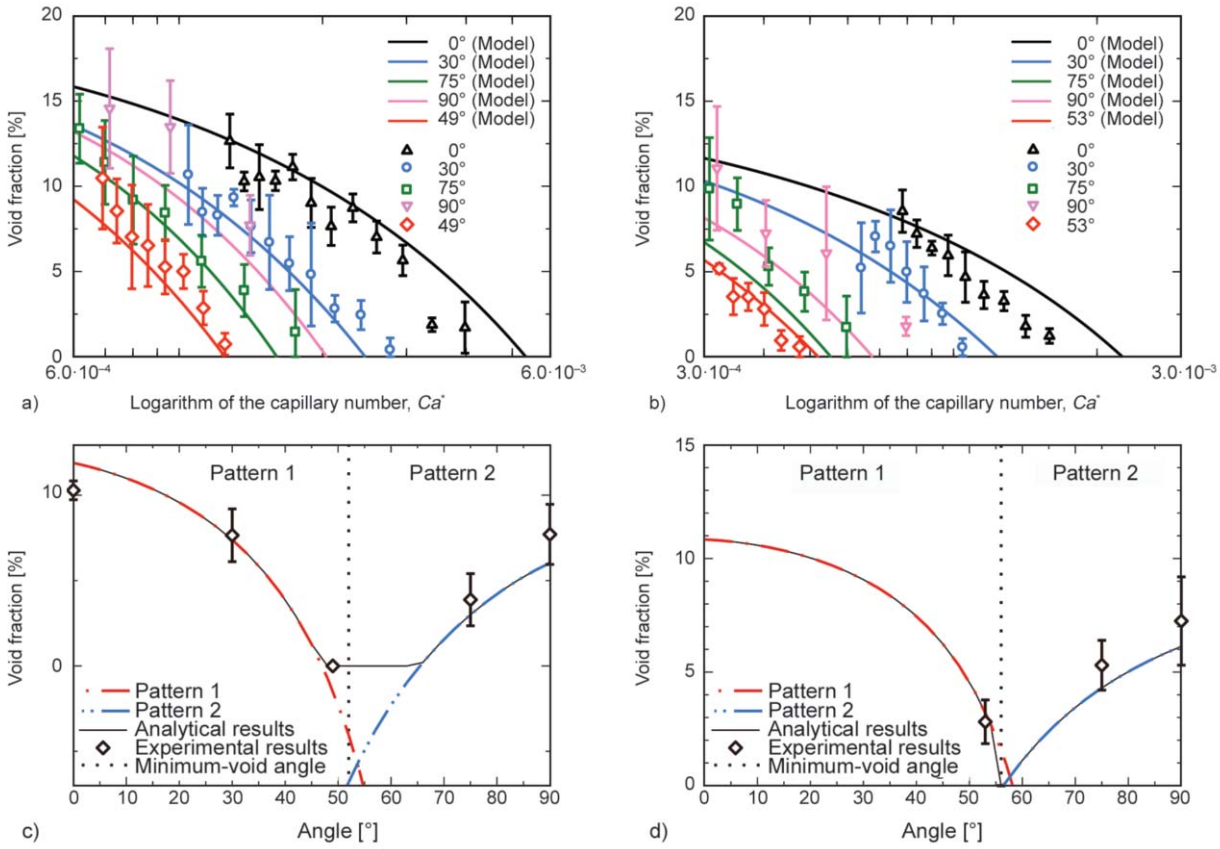

Figure 11. A comparison of the theoretical and experimental results. A relationship between the capillary number and the void fraction for different flow directions in (a) M155 and (b) M200. Void fraction as a function of the angle between the flow direction and the fiber orientation at a constant flow velocity in (c) M155 and (d) M200.

more, deviations also occurred because the model for the present study was simplified and omitted the effect of the impregnation time for the crimps and perpendicular tilts and twists of the fiber bundles. Nonetheless, because as a trend the relationship between the impregnation angle and capillary number were virtually consistent between the experimental and predicted results, we consider the proposed model to be useful for predicting void formation.

5. Conclusions

Experimental 2D radial-injection VaRTM was performed using two types of an anisotropic plain-woven fabric. The void distributions during resin impregnation were obtained. We determined the relationship between the void fraction and the resin flow velocity for an impregnation direction inclined at an arbitrary angle to the fiber-bundling direction. Void formation was also demonstrated to be a function of the resin impregnation angle in the microscopic structure of the fabric. Our observations reveal that void formation varies with the resin impregnation angle and is minimized at the minimum-void angle, which corresponds to the border between the two void formation patterns. Based on the variations in the void formation pattern with the resin impregnation angle in the microscopic structure of the fabric, a theoretical model was developed for predicting the void fraction value at arbitrary values of the resin impregnation angle and velocity in the anisotropic fabric. This model can also be used to predict the minimum-void angle values, for which void formation is minimized. The model predictions were compared with the experimental results indicating a good agreement between them.

For simplicity, the present study was devoted to void formation in a single fabric layer. However, a realistic composite structure contains multiple layers, which may induce air trappings between the layers in addition to those existing within the layers. Therefore, further studies are required to develop an analytical model for predicting void formation in multiple layers. The proposed model would necessarily consider spatial uncertainties in mesoscale structures caused by overlapping layers.

Appendix A. Derivations of the macroscopic resin flow velocity and pressure gradient parameters for elliptical resin impregnation

The experiments in this study were related to the 2D radial-injection VaRTM, in which the resin was infused from the center of the fabric and impregnated in the radial direction, as shown in Figure 1a. Therefore, the macroscopic resin flow velocity and the pressure gradient for elliptical resin impregnation parameters were derived for a comparison with the experimental results.

The 2D pressure governing equation for the resin impregnation by one-point injection can be obtained from Equation (A.1) [30, 31]:

$$\frac{\partial^2 P}{\partial x^2} + \frac{K_y}{K_x} \cdot \frac{\partial^2 P}{\partial y^2} = 0 \tag{A.1}$$

where K_x and K_y are the macroscopic permeabilities in the x and y directions, respectively (taking into consideration the sectional porosity).

By using the quasi-isotropic distances $\overline{x}$ and $\overline{y}$ determined by Equation (A.2), the domain in Equation (A.1) was modified into the quasi-isotropic one expressed by Equation (A.3) for a pressure field:

$$\overline{x} = \left(\frac{K_y}{K_x}\right)^{\frac{1}{4}} x, \quad \overline{y} = \left(\frac{K_x}{K_y}\right)^{\frac{1}{4}} y \tag{A.2}$$

$$\frac{\partial^2 P}{\partial \overline{x}^2} + \frac{\partial^2 P}{\partial \overline{y}^2} = 0 \tag{A.3}$$

By converting Equation (A.3) into polar coordinates, an ordinary differential equation containing a quasi-isotropic radius $\overline{r}$ is obtained (Equation (A.4)):

$$\frac{\mathrm{d}^2 P}{\mathrm{d}\overline{r}^2} + \frac{1}{\overline{r}} \cdot \frac{\mathrm{d}P}{\mathrm{d}\overline{r}} = 0 \tag{A.4}$$

where the quasi-isotropic radius $\overline{r}$ is defined by (Equation (A.5)):

$$\overline{r} = \sqrt{\overline{x}^2 + \overline{y}^2} \tag{A.5}$$

From Equation (A.4), the quasi-isotropic macroscopic pressure gradient is obtained for the boundary condition $P = 0$ at a flow front $\overline{r} = \overline{r}_f$ and $P = P_{vac}$ at an injection point $\overline{r} = \overline{r}_0$ as Equation (A.6):

$$\frac{\mathrm{d}P}{\mathrm{d}\overline{r}} = \frac{P_{vac}}{\ln \overline{r}_f - \ln \overline{r}_0} \cdot \frac{1}{\overline{r}} \tag{A.6}$$

where $\bar{r}_0$ is the quasi-isotropic injection point determined by Equation (A.7) for an injection point radius r_0 and an angle φ formed by the center point:

$$\bar{r}_0 = r_0\sqrt{\left(\frac{K_y}{K_x}\right)^{\frac{1}{2}}\cos^2\varphi + \left(\frac{K_x}{K_y}\right)^{\frac{1}{2}}\sin^2\varphi} \tag{A.7}$$

The quasi-isotropic permeability $\bar{K}$ in the resin impregnation direction can be calculated by using Equation (A.8), whereas the quasi-isotropic resin flow velocity $\bar{U}$ is defined by Equation (A.9):

$$\bar{K} = \sqrt{K_x K_y} \tag{A.8}$$

$$\bar{U} = -\frac{\bar{K}}{\mu}\cdot\frac{dP}{d\bar{r}} \tag{A.9}$$

Using the quasi-isotropic resin flow velocity calculated earlier, the real resin flow velocity value can be obtained. The coefficients used to convert the quasi-isotropic resin flow velocities in the x and y directions into the real flow velocities are $(K_x/K_y)^{1/4}$ and $(K_y/K_x)^{1/4}$, respectively, whereas the tensor $\mathbf{c}_K$ used to convert the quasi-isotropic resin flow velocity into the real flow velocity at an arbitrary impregnation angle is defined by Equation (A.10):

$$\mathbf{c}_K = \begin{bmatrix} \left(\frac{K_x}{K_y}\right)^{\frac{1}{4}} & 0 \\ 0 & \left(\frac{K_y}{K_x}\right)^{\frac{1}{4}} \end{bmatrix} \tag{A.10}$$

The real resin flow velocity for an arbitrary angle in terms of the tensor $\mathbf{c}_K$ can be determined using Equation (A.11):

$$\mathbf{U} = \mathbf{c}^T\mathbf{c}_K\mathbf{c}\bar{\mathbf{U}} \tag{A.11}$$

where $\mathbf{c}$ is the transformation matrix. From Equation (A.11), the real resin flow velocity U_n in the resin impregnation direction can be expressed as Equation (A.12):

$$U_n = \left(\left(\frac{K_x}{K_y}\right)^{\frac{1}{4}}\cos^2\theta + \left(\frac{K_y}{K_x}\right)^{\frac{1}{4}}\sin^2\theta\right)\bar{U} \tag{A.12}$$

Here the permeability K_{aniso} and flow velocity U_{aniso} values at an arbitrary angle in anisotropic fabrics are expressed using the macroscopic pressure gradient of the resin impregnation direction $\partial P/\partial n$ [32] (Equations (A.13) and (A.14)):

$$K_{aniso} = K_x\cos^2\theta + K_y\sin^2\theta \tag{A.13}$$

$$U_{aniso} = -\frac{K_x\cos^2\theta + K_y\sin^2\theta}{\mu}\cdot\frac{\partial P}{\partial n} \tag{A.14}$$

Assuming that the real resin flow velocity U_n is the same as the flow velocity U_{aniso} in the flow direction, $\partial P/\partial n$ can be expressed as Equations (A.15):

$$\frac{\partial P}{\partial n} = \bar{K}\frac{\left(\left(\frac{K_x}{K_y}\right)^{\frac{1}{4}}\cos^2\theta + \left(\frac{K_y}{K_x}\right)^{\frac{1}{4}}\sin^2\theta\right)}{K_x\cos^2\theta + K_y\sin^2\theta} \tag{A.15}$$

References

[1] Mallick P. K.: Fiber-reinforced composites. CRC Press, Boca Raton (1993).

[2] Gibson R. F.: Principles of composite material mechanics. CRC Press, Boca Raton (2011).

[3] Advani S. G., Sozer E. M.: Process modeling in composites manufacturing. CRC Press, Boca Raton (2002).

[4] Matsuzaki R., Kobayashi S., Todoroki A., Mizutani Y.: Flow control by progressive forecasting using numerical simulation during vacuum-assisted resin transfer molding. Composites Part A: Applied Science and Manufacturing, **45**, 79–87 (2013).
DOI: 10.1016/j.compositesa.2012.09.014

[5] Matsuzaki R., Kobayashi S., Todoroki A., Mizutani Y.: Control of resin flow/temperature using multifunctional interdigital electrode array film during a VaRTM process. Composites Part A: Applied Science and Manufacturing, **42**, 782–793 (2011).
DOI: 10.1016/j.compositesa.2011.03.004

[6] Huang H., Talreja R.: Effects of void geometry on elastic properties of unidirectional fiber reinforced composites. Composites Science and Technology, **65**, 1964–1981 (2005).
DOI: 10.1016/j.compscitech.2005.02.019

[7] Varna J., Joffe R., Berglund L. A., Lundström T. S.: Effect of voids on failure mechanisms in RTM laminates. Composites Science and Technology, **53**, 241–249 (1995).
DOI: 10.1016/0266-3538(95)00024-0

[8] Ghiorse S. R.: Effect of void content on the mechanical properties of carbon/epoxy laminates. SAMPE Quarterly, **24**, 54–59 (1993).

[9] Lee D. H., Lee W. I., Kang M. K.: Analysis and minimization of void formation during resin transfer molding process. Composites Science and Technology, **66**, 3281–3289 (2006).
DOI: 10.1016/j.compscitech.2005.07.008

[10] Johnson R. J., Pitchumani R.: Flow control using localized induction heating in a VaRTM process. Composites Science and Technology, **67**, 669–684 (2007).
DOI: 10.1016/j.compscitech.2006.04.012

[11] Matsuzaki R., Kobayashi S., Todoroki A., Mizutani Y.: Full-field monitoring of resin flow using an area-sensor array in a VaRTM process. Composites Part A: Applied Science and Manufacturing, **42**, 550–559 (2011). DOI: 10.1016/j.compositesa.2011.01.014

[12] Patel N., Rohatgi V., Lee L. J.: Micro scale flow behavior and void formation mechanism during impregnation through a unidirectional stitched fiberglass mat. Polymer Engineering and Science, **35**, 837–851 (1995). DOI: 10.1002/pen.760351006

[13] Schell J. S. U., Deleglise M., Binetruy C., Krawczak P., Ermanni P.: Numerical prediction and experimental characterisation of meso-scale-voids in liquid composite moulding. Composites Part A: Applied Science and Manufacturing, **38**, 2460–2470 (2007). DOI: 10.1016/j.compositesa.2007.08.005

[14] Lundström T. S., Gebart B. R.: Influence from process parameters on void formation in resin transfer molding. Polymer Composites, **15**, 25–33 (1994). DOI: 10.1002/pc.750150105

[15] Chen Y-T., Davis H. T., Macosko C. W.: Wetting of fiber mats for composites manufacturing: I. Visualization experiments. AIChE Journal, **41**, 2261–2273 (1995). DOI: 10.1002/aic.690411009

[16] Yamaleev N., Mohan R.: Effect of the phase transition on intra-tow flow behavior and void formation in liquid composite molding. International Journal of Multiphase Flow, **32**, 1219–1233 (2006). DOI: 10.1016/j.ijmultiphaseflow.2006.05.011

[17] Liu B., Bickerton S., Advani S. G.: Modelling and simulation of resin transfer moulding (RTM)–gate control, venting and dry spot prediction. Composites Part A: Applied Science and Manufacturing, **27**, 135–141 (1996). DOI: 10.1016/1359-835X(95)00012-Q

[18] Restrepo O., Hsiao K-T., Rodriguez A., Minaie B.: Development of adaptive injection flow rate and pressure control algorithms for resin transfer molding. Composites Part A: Applied Science and Manufacturing, **38**, 1547–1568 (2007). DOI: 10.1016/j.compositesa.2007.01.005

[19] Phelan F. R.: Simulation of the injection process in resin transfer molding. Polymer Composites, **18**, 460–476 (1997). DOI: 10.1002/pc.10298

[20] Gokce A., Hsiao K-T., Advani S. G.: Branch and bound search to optimize injection gate locations in liquid composite molding processes. Composites Part A: Applied Science and Manufacturing, **33**, 1263–1272 (2002). DOI: 10.1016/S1359-835X(02)00047-7

[21] Park C. H., Lebel A., Saouab A., Bréard J., Lee W. I.: Modeling and simulation of voids and saturation in liquid composite molding processes. Composites Part A: Applied Science and Manufacturing, **42**, 658–668 (2011). DOI: 10.1016/j.compositesa.2011.02.005

[22] Matsuzaki R., Seto D., Todoroki A., Mizutani Y.: Void formation in geometry–anisotropic woven fabrics in resin transfer molding. Advanced Composite Materials, **23**, 99–114 (2013). DOI: 10.1080/09243046.2013.832829

[23] Matuzaki R., Seto D., Naito M., Todoroki A., Mizutani Y.: Analytical prediction of void formation in geometrically anisotropic woven fabrics during resin transfer molding. Composites Science and Technology, **107**, 154–161 (2015). DOI: 10.1016/j.compscitech.2014.12.013

[24] Matsuzaki R., Seto D., Todoroki A., Mizutani Y.: *In situ* void content measurements during resin transfer molding. Advanced Composite Materials, **22**, 239–254 (2013). DOI: 10.1080/09243046.2013.801822

[25] Kang M. K., Lee W. I., Hahn H. T.: Formation of microvoids during resin-transfer molding process. Composites Science and Technology, **60**, 2427–2434 (2000). DOI: 10.1016/S0266-3538(00)00036-1

[26] Rohatgi V., Patel N., Lee L. J.: Experimental investigation of flow-induced microvoids during impregnation of unidirectional stitched fiberglass mat. Polymer Composites, **17**, 161–170 (1996). DOI: 10.1002/pc.10601

[27] Erickson D., Li D., Park C. B.: Numerical simulations of capillary-driven flows in nonuniform cross-sectional capillaries. Journal of Colloid and Interface Science, **250**, 422–430 (2002). DOI: 10.1006/jcis.2002.8361

[28] Gebart B. R.: Permeability of unidirectional reinforcements for RTM. Journal of Composite Materials, **26**, 1100–1133 (1992). DOI: 10.1177/002199839202600802

[29] Ahn K. J., Seferis J. C., Berg J. C.: Simultaneous measurements of permeability and capillary pressure of thermosetting matrices in woven fabric reinforcements. Polymer Composites, **12**, 146–152 (1991). DOI: 10.1002/pc.750120303

[30] Adams K. L., Russel W. B., Rebenfeld L.: Radial penetration of a viscous liquid into a planar anisotropic porous medium. International Journal of Multiphase Flow, **14**, 203–215 (1988). DOI: 10.1016/0301-9322(88)90006-7

[31] Vanegas J. D., Patiño I. D., Vargas C. A.: Boundary element approaches for filling simulations of anisotropic reinforced preforms used in the resin transfer molding process. Journal of Composite Materials, **48**, 2603–2629 (2014). DOI: 10.1177/0021998313501917

[32] Wang T. J., Wu C. H., Lee L. J.: In-plane permeability measurement and analysis in liquid composite molding. Polymer Composites, **15**, 278–288 (1994). DOI: 10.1002/pc.750150406